

# Characterization of Seawater Intrusion and Submarine Groundwater Discharge: Field and laboratory approach

PhD Thesis  
Laura Martínez Pérez



Laura Martínez Pérez



UNIVERSITAT POLITÈCNICA  
DE CATALUNYA  
BARCELONATECH

PhD program in Geotechnical Engineering

# Characterization of seawater intrusion and submarine groundwater discharge in alluvial coastal aquifers: field and laboratory approach

**Doctoral thesis by:**

Laura Martínez Pérez

**Thesis advisor:**

Linda Luquot

Jesús Carrera

Civil and Environmental Engineering

Barcelona, Febrero 2020



### **Aknowlegments**

This work was funded by the projects CGL2013-48869-C2-1-R/2-R and CGL2016-77122-C2-1- R/2-R of the Spanish Government. We would like to thank SIMMAR (Serveis Integrals de Manteniment del Maresme) and the Consell Comarcal del Maresme in the construction of the research site. Authors wants to thank the support of the Generalitat de Catalunya to MERS (2018 SGR-1588). This work is contributing to the ICTA 'Unit of Excellence' (MinECo, MDM2015-0552).

# Abstract

Seawater intrusion (SWI) causes not only salinization of coastal aquifers, but also a reduction submarine groundwater discharge (SGD) and nutrient fluxes to marine ecosystems.

We have developed a small scale experimental field site to gain insights into both SWI and SGD. The site is located in a coastal alluvial aquifer at the mouth of an ephemeral stream in the Maresme coastline (Barcelona, Spain).

Here, we describe our attempts for a detailed site characterization, which was based on the four pillars of hydrogeology: geology (Lithological description and geochemical analysis of core), geophysics (borehole logs, Electrical Resistivity Tomography and thermal monitoring), hydraulics (pumping and tidal response tests) and hydrochemistry (major and minor elements, stable isotopes and Radium isotopes for SGD assessment).

As it turned out, all four pillars yielded some surprise. The aquifer consists of alluvial sediments, rather than coastal plain deposits. Tidal loading, rather than hydraulic connection to the sea, appears to drive tidal response, in spite of the aquifer being unconfined. Hydrochemistry suggests an unusually reactive layer, with all cations reflecting some mineral dissolution process, beyond the expected cation exchange. Radium increased with salinity, but the correlation was poor, partly blurred by pH, which was low in the deep portions of the aquifer.

These observations were largely explained with the help of geophysics. Both borehole logs and cross-hole ERT helped in identifying silt layers that are frequent in alluvial deposits but proved to play a critical role here.

The integration of the different techniques allowed to characterize the different distribution of salt- and fresh- groundwater, that in fact yielded an inverse disposition to what is expected in coastal hydrogeology.

To improve SGD quantification, we also characterized radium behavior within the aquifer. The recovered sediment during borehole drilling was used to perform both batch and column laboratory experiments. We performed constant salted fluid injections but we also vary the salinity (SWI and SGD simulation) to infer adsorbed Ra from its mobilization.

Column experiments were later simulated using a 0D model to interpret the results. We have observed that heterogeneous flux through preferential flow paths occurs in the columns. Variations in these flow paths may explain the observed fluctuations. Such variations may also occur during the freshening and salinization experiments, but the changes in sorption are so dominant that overcome the impact of changes in porosity structure.

# Resumen

La intrusión de agua de mar (SWI) causa no solo la salinización de los acuíferos costeros, sino también una reducción de la descarga submarina de aguas subterráneas (SGD) y los flujos de nutrientes a los ecosistemas marinos.

Con el fin de poder caracterizar de una manera acoplada ambos procesos, hemos desarrollado un "laboratorio" de campo. La zona de campo experimental está ubicada en un acuífero aluvial costero, en la margen derecha de la desembocadura de una riera efímera, en la costa del Maresme (Barcelona, España).

Aquí, describimos nuestros intentos de caracterización detallada del sitio, basándonos en los cuatro pilares de la hidrogeología: geología (descripción litológica y análisis geoquímico de sedimentos), geofísica (registros de pozos, tomografía de resistividad eléctrica y monitoreo térmico), hidráulica (bombeo y ensayos de respuesta a marea) e hidroquímica (elementos mayores y menores, isótopos estables e isótopos de radio para la evaluación de la SGD).

Al final resultó que, los cuatro pilares arrojaron algo de sorpresa. El acuífero consiste en sedimentos aluviales, en lugar de depósitos llanura costera.

A pesar de que el acuífero es libre, parece que la respuesta del acuífero a las mareas está causada por la carga mecánica impuesta por el mar, en lugar de evidenciar la conexión hidráulica con el mismo. La hidroquímica sugiere una zona altamente reactiva, con todos los cationes reflejando algún proceso de disolución mineral, más allá del intercambio de catiónico esperado. El radio aumenta con la

salinidad, pero no de una manera evidente, debido a que el pH es especialmente ácido en la zona más profunda del acuífero considerado.

Todas estas observaciones pudieron realizarse gracias en gran medida a la ayuda de los diferentes métodos geofísicos aplicados. Tanto los registros de pozo como la tomografía eléctrica de resistividad realizada entre los pozos, ayudaron a identificar capas de limo, frecuentes en los depósitos aluviales, pero que demostraron desempeñar un papel fundamental aquí.

La integración de las diferentes técnicas permitió caracterizar la distribución de diferentes masas de agua subterránea salada y dulce, que de hecho presentaban una disposición inversa a lo que se espera en zonas costeras.

Para mejorar la cuantificación de los flujos de SGD, también se caracterizó el comportamiento del radio dentro del acuífero. El sedimento recuperado durante la perforación de los pozos se utilizó para realizar experimentos batch y en columna en el laboratorio. Para ello, realizamos lavados consecutivos a salinidad constante, pero también variando la salinidad (simulando eventos de SWI y SGD), para inferir el Ra adsorbido a partir de su movilización.

Posteriormente se modelaron los experimentos de columna utilizando un modelo 0D para interpretar los resultados. En las columnas hemos observado flujo heterogéneo a través de caminos preferentes. Las variaciones en estos caminos podrían explicar las fluctuaciones observadas en los experimentos realizados a salinidad constante. Dichas variaciones también pueden ocurrir durante los experimentos de descarga de agua dulce y salinización, pero los cambios en la sorción del radio con la salinidad son tan dominantes que superan el impacto de los cambios en la estructura de la porosidad.

## TABLE OF CONTENTS

<b>CHAPTER 1. INTRODUCTION .....</b>	<b>5</b>
<b>CHAPTER 2. CHARACTERIZATION OF THE MEDITERRANEAN COASTAL AQUIFER OF ARGENTONA .....</b>	<b>9</b>
2.1 INTRODUCTION .....	11
2.2 SITE DESCRIPTION .....	13
2.2.1 Geological situation .....	13
2.2.2 Equipment .....	13
2.3 METHODS.....	16
2.3.1 Geological characterization .....	16
2.3.2 Geophysical characterization.....	17
2.3.3 Hydrodynamic characterization.....	18
2.3.4 Hydrochemical and isotopic characterization .....	19
2.4 RESULTS AND DISCUSSION .....	20
2.4.1 Sedimentary structure .....	20
2.4.2 Geophysical response of the aquifer .....	27
2.4.3 Hydraulics .....	30
2.4.4 Hydrochemical behavior.....	32
2.5 SUMMARY .....	40
<b>CHAPTER 3. QUESTIONING THE TRADITIONAL PARADIGM FOR SEAWATER INTRUSION: EVIDENCE FROM SALINITY PROFILES .....</b>	<b>43</b>
3.1 INTRODUCTION .....	45
3.2 CHARACTERIZATION METHODS.....	47
3.3 RESULTS: SALINITY PROFILES .....	49
3.4 DISCUSSION: SWI PATTERNS AND IMPLICATIONS FOR BOREHOLE SALINITY PROFILES .....	51
3.5 SUMMARY .....	56
<b>CHAPTER 4. LABORATORY EXPERIMENTS TO CHARACTERIZE RADIUM DESORPTION... 57</b>	<b>57</b>
4.1 INTRODUCTION .....	59
4.2 EXPERIMENTAL MATERIALS AND METHODS .....	61
4.2.1 Batch experiment .....	62
4.2.2 Column experiments .....	62
4.3 INTERPRETATION METHOD.....	64
4.3.1 Radium sorption .....	64
4.3.2 Radium mass balance .....	65
4.4 RESULTS .....	66
4.4.1 Time impact on radium desorption .....	67
4.4.2 Desorption at different salinities .....	68
4.4.3 Desorption at consecutive fixed inlet salinities .....	68
4.4.4 Desorption at variable salinities.....	70
4.5 DISCUSSION.....	71
4.5.1 Displacement tests at fixed salinity .....	72
4.5.2 Displacement tests to simulate SWI and SGD .....	73
4.6 MODELING.....	75
4.7 SUMMARY .....	79
<b>CHAPTER 5. CONCLUSIONS AND FUTURE STEPS.....</b>	<b>81</b>
<b>REFERENCES.....</b>	<b>85</b>
<b>APPENDIX A .....</b>	<b>91</b>

## Figure Index

Figure 2-1- Localization of the experimental site and nests distribution.....	14
Figure 2-2- Lithostratigraphic correlation. Geological cross-section (AA', see Figure 2-1. Sea is to the right). Also shown are the gamma ray logs and the textural and mineralogical description from logs. It must be mentioned that the potential continuity of the bottom silt layers emerged from the interpretation of other data.....	21
Figure 2-3 - Integration and correlation of logging techniques (MSUS: Magnetic susceptibility; SGR: Spectral Gamma Ray; EC <sub>b</sub> : Bulk electrical conductivity of the formation) and stratigraphic column of the deepest boreholes (25 m).....	22
Figure 2-4 - Geochemical analyses made on core samples extracted from borehole N1-25.....	23
Figure 2-5 - Evolution with depth of the different oxides. Elemental composition expressed in weight percent of oxides obtained after acid digestion of the samples extracted from borehole N1-25. ....	24
Figure 2-6- Magnetic susceptibility measured on core vs MnO % obtained after acid digestion of sediments.....	27
Figure 2-7- A) SGR Logs of all the boreholes. Total CPS from spectral gamma ray logs and B) Th/K ratios for each surveyed borehole.....	28
Figure 2-8 - Zoom in the freshwater zone of EC <sub>b</sub> logs.....	29
Figure 2-9- Relationship of induction logs and EC <sub>w</sub> .....	30
Figure 2-10 - Comparison of transmissivities obtained from grain size distribution (Hazen and Shepherd) and from hydraulic tests. ....	31
Figure 2-11 -. Results obtained from the tidal method: A) Spectra of the sea and N3 nest signals (Lunar semidiurnal, M2, and lunar diurnal, K1 and O1, components are apparent both in the sea and boreholes); B) scaled time lag and C) scaled dampening in each borehole versus distance to the coast calculated using the components with highest amplitude (hollow symbols for K1 and filled for M2). Under ideal conditions, all points should coincide on a straight line, identical for B) and C). ....	32
Figure 2-12 – Cross-section of the aquifer with stiff diagrams of each sampling point. ....	34
Figure 2-13 - Evolution of the measured parameters with depth. ....	35
Figure 2-14 - Hydrochemical characterization: Ionic relationships of the different elements (in mg L <sup>-1</sup> ) (A). δ <sup>18</sup> O vs δD values for 16 sampled piezometers, freshwater and seawater. The seawater mixing line has been represented in degradation from blue (fresh) to red (saline). Isotopic composition of precipitation in Barcelona has also been represented (B). Radium activity measured in the wells. No freshwater samples or seawater samples were analyzed (C).....	37
Figure 2-15 - Relationship of <sup>224</sup> Ra and pH. ....	39
Figure 2-16 – Evolution with depth of the CEC and exchangeable Na <sup>+</sup> measurements performed on core. ....	40
Figure 3-1 Traditional SWI paradigm that can be found in textbooks (e.g., (Bear et al., 1999; Custodio and Llamas, 2001); (Domenico and Schwartz, 1998), for a homogeneous steady state aquifer with a fixed sea boundary and correspondent salinity profiles (A) or a multi-layer aquifer (B) and for a significant tidal range (C). (This figure has been inspired by Jiao and Post (2019)). ....	45
Figure 3-2. Examples of salinity profiles performed in Y. Liu, Jiao, Liang, and Kuang (2017) (A), Buckley et al. (2001) (B), Shalev et al. (2009) (C) and Yechieli et al. (2010) (D). The average EC <sub>w</sub> of western Mediterranean Sea is marked with a blue line. Red and green lines represent salinity profiles obtained at different times. ....	46
Figure 3-3 Localization of the Argenton Experimental site, annual precipitation regime (Average for the period 2001-2017: 584.1 mm), disposition of the wells and cross-section A-A' with the geology and localization of piezometers slotted intervals. ....	48
Figure 3-4 Monthly precipitation in mm of the monitored years. The date of salinity profiles acquisition is marked in vertical dotted lines. Salinity profiles performed in PP20 representative of the different seasons (A), B), C) and D)). Salinity profiles after rain events compared with seawater EC <sub>w</sub> (E).....	50
Figure 3-5 Combination of geophysical measurements: Induction logging (electromagnetic method) (mS/m) and CHERT profiles (geo-electric method) and point measurements EC <sub>w</sub> (mS/cm) performed in the different piezometers belonging to each nest. The localization of slotted intervals of each piezometer is marked with blue squares. In PP20 fluid sampling was performed at two different depths. CHERT profile has resolution constraints below 20 m at the edges and is not taken into account for the analysis.....	53

Figure 3-6 Comparison of (A) salinity and (B) CHERT profiles with (C) SGR logs in PP20.....54

Figure 3-7 Combination of CHERT and surficial ERT (from (Palacios et al., 2019)).....55

Figure 4-1 Experimental setup. ....62

Figure 4-2- Batch experiments performed at halite saturation. Activity of  $^{224}\text{Ra}$  measured after consecutive batch experiments. ....67

Figure 4-3 - Activity of  $^{224}\text{Ra}$  measured in the four columns after being in contact for different periods of time (C1: 72h, C2: 3h, C3: 1h and C4: 0h since the first injection). ....68

Figure 4-4.-  $^{224}\text{Ra}$  measured activity in the four columns at different salinities in secular equilibrium. ....68

Figure 4-5.- Consecutive percolations performed on C3. A: at 30 g/L and B at 80 g/L. In bottom B part, the outlet water salinity is presented all along the different percolations. ....69

Figure 4-6.- Consecutive percolations performed on C2. ....70

Figure 4-7.- Simulation of a SWI event in column C4. Evolution of inlet and outlet salinity (A) and radium desorption (B).....71

Figure 4-8.- Simulation of an SGD event in column C2. Evolution of inlet and outlet salinity (A) and temporal evolution of  $^{224}\text{Ra}$  activity (B).....71

Figure 4-9.- Measured  $^{224}\text{Ra}$  activity during salinization and freshening events. Inlet salinity of the percolating volumes is marked in blue. ....73

Figure 4-10.- Results of the simulations for fixed inlet salinity simulations. ....76

Figure 4-11- Results of the simulations performed for the SWI and SGD events. ....77

Figure 4-12- Measured and computed  $^{224}\text{Ra}$  activity and salinity for the whole set of percolations. ....78

## Table index

Table 2-1.- Characteristics of the different types of boreholes and relation of logs performed. Being ECL: electrical conductivity logging, MSUS: Magnetic susceptibility, SGR: Spectral Gamma Ray, GR: total gamma ray, ERT: electrodes along the borehole. Among this instrumentation, all boreholes are equipped with FO. ....	15
Table 2-2.- DRX of the extracted samples. Mineral composition in % of the different samples extracted from borehole N1-25. ....	24
Table 2-3.- Multielemental composition of the samples obtained from N1-25 in $\mu\text{g}\cdot\text{g}^{-1}$ , including U, Th and trace elements from acid digestion.....	25
Table 2-4.- Hydraulic conductivity obtained from grain size analysis. ....	30
Table 2-5.- Results of the short pumping tests performed in each borehole. ....	31
Table 2-6.- Groundwater major element concentrations in $\text{mg}\cdot\text{L}^{-1}$ .....	36
Table 2-7.- Measured parameters and characteristics of the "anomalous" piezometers in terms of radium concentration. Note that radium measurements (in $\text{Bq}\cdot\text{kg}^{-1}$ ) were performed on core extracted from borehole N1-25. ....	38
Table 3-1 Geophysical acquisitions .....	51
Table 4-1 - Different experimental conditions to obtain $K_d$ (units in $\text{mL/g}$ if not explicit). ....	60
Table 4-2 - Geochemical parameters of sample n1-13.....	61
Table 4-3 - Experimental conditions.....	63
Table 4-4 - Simulation events (SWI and SGD), and the correspondent salinity of each displacing pore volume (PV).....	63
Table 4-5 – Input parameters for the model. ....	75
Table 4-6 –Calibrated parameters.....	77

# Chapter 1.

## Introduction



The landward incursion of seawater can be caused by prolonged changes in coastal groundwater levels due to pumping, triggered by land-use change, climate variations or sea-level fluctuations. It has a direct impact on the reduction of available freshwater and contamination of production wells. The term seawater intrusion (**SWI**) refers to the subsurface movement of seawater and its associated factors, such as dispersive mixing, tidal effects, density effects including unstable convection, surface hydrology (e.g. recharge and interactions between surface and subsurface), paleo-hydrogeological conditions, anthropogenic influences and geological characteristics (Custodio and Bruggeman, 1987).

SWI is a global issue due to the increasing demands for freshwater in coastal zones, and the influences of rising sea levels and changing climates. It has been a topic of considerable research effort, but the characterization and prediction of the freshwater-salt water interface over regional scales and in highly heterogeneous and dynamic settings is still challenging.

The study of submarine groundwater discharge (**SGD**) to the sea is a topic of growing interest to both the scientific community and national administrations. Its importance is derived from freshwater resources management in coastal aquifers and from the transport of pollutants and nutrients into the sea, as it can lead to an alteration of coastal biogeochemical cycles. Numerous studies highlight the importance of correctly assessing the SGD to determine the input of nutrients and dissolved pollutants in different coastal ecosystems (Garcia-Solsona et al., 2010). One of the most widespread methods to calculate SGD fluxes, among other techniques described in the compilation made by Burnett et al. (2006a), rely on the quantification of natural radioactive tracers (Charette et al., 2001; Moore, 1996; Rodellas i Vila et al., 2015).

Ideally, SGD can be derived as the ratio of radium flux into the sea divided by Ra concentration in groundwater. The latter is in question because Ra adsorbs onto the solids and adsorbed/dissolved distribution of Ra is affected by exchange with sodium during aquifer salinization. As a result, fluctuations of the fresh and saline groundwater interface can mobilize, concentrate and dilute Ra isotopes. Interpreting Ra isotope measurements can be problematic in complex coastal systems.

The complexity of both SWI and SGD requires detailed hydrogeological characterization for proper understanding (Michael et al., 2011) (Werner et al., 2013). There is a **lack of well-characterized examples of SWI sites**, which makes it difficult to understand field-scale processes, such as those controlling mixing zones, salt water upconing, heterogeneity effects and Ra mobilization.

Intensive measurement campaigns to characterize accurately interfaces and their movement in a real coastal aquifer together with geological, geophysical and hydrogeological research seems to be the only way to overcome those weaknesses. In order to advance along this path and specifically to gain insights in the coupling of SWI and SGD, we built a field laboratory in the Maresme coast, in the frame of project MEDISTRAES (Mixing and dispersion in the transport of energy and solutes).

The original goal of this thesis was to characterize the experimental site in order to better constrain the factors that determine the impact of the coalescence of both fluxes. This included both field work at the site and laboratory work to understand sorption properties of the aquifer material.

Accordingly, this thesis has been structured in three main chapters. Each one corresponds to a future publication:

**Chapter 2** contains a description of the experimental site and the results obtained during its characterization: sedimentary structure, nature of sediments, and hydrochemistry, including the distribution of Th chain radioisotopes, both in the solid phase and in dissolution.

As it turned out, the resulting characterization was surprising in that fresh water discharges not only above seawater was also below. We argue in **Chapter 3** that this feature may not be an exceptional feature of Argentona, but a frequent situation because it helps to explain the anomalous salinity profiles that are often measured in fully slotted coastal wells.

**Chapter 4** contains the description of laboratory experiments aimed characterizing Ra sorption. In particular, we propose a new type experiment to calculate concentrations adsorbed and in solution.

The conclusions and future works suggested by this thesis are summarized in **Chapter 5**.

## **Chapter 2.**

Conceptual and methodological surprises in the  
characterization of the Mediterranean coastal  
aquifer of Argenton



## 2.1 INTRODUCTION

Seawater Intrusion (SWI) is a global problem (Michael et al., 2017; Werner et al., 2013) because coastal zones are increasingly demanded for human settlements, often linked to the fertile lands of deltas distributed worldwide (Tessler et al., 2015). The hydrology community (Michael et al., 2017) has devoted a significant research effort to address the problem. Lowering of heads, which drives SWI, also causes a reduction of submarine groundwater discharge (SGD) and, thus, of the nutrient flux to submarine ecosystems (Church, 1996) (Moore and others, 1996; Younger, 1996). Only recently has the hydrology community started to think actively of the coupled SWI-SGD problem. Yet, no clear methodology exists to address the management of either SWI or SGD, which probably reflects the complexity of the problem. The interaction between discharging fresh water and seawater is sensitive to numerous factors: temporal fluctuations (ranging from tidal, different everywhere, to seasonal); typically, high but often uncertain pumping; complex hydrochemistry.

Proper understanding requires a thorough characterization. The sedimentological and petrophysical complexity of coastal aquifers causes their hydraulics and geochemistry to be equally complex. As a consequence, SWI research has comprised mostly a theoretical and numerical framework or has concentrated on specific aspects of the problem: geology (Abarca, 2006; Bampalouka, 2016; Díaz and Maldonado, 1990; Heinz et al., 2003; Maier et al., 2005), hydrodynamics (Chidichimo et al., 2015; Guo et al., 2010b; Sherif et al., 2018; Vallejos et al., 2015) and hydrochemistry (Ozler, 2003; Tamez-Meléndez et al., 2016). These approaches are sometimes combined such as hydraulics and geophysics, and hydrochemistry and hydrodynamics (Falgàs et al., 2011b; Goldman and Kafri, 2006; Li et al., 2009; Xue et al., 2000). We feel that proper understanding requires addressing the four pillars of hydrogeology (geology, geophysics, hydraulics, and hydrochemistry and isotopes).

Coastal aquifers geology is specifically complex because conventional sedimentary variability often mixes with sea level fluctuations associated to glaciations and eustatic movements. These may lead to progradation-retrogradation events (Gámez et al., 2009); (Rovere et al., 2016). To taper off this complexity, high-resolution data are needed. These data can be provided by core data analyses, essential for sedimentology understanding, for identifying the minerals that may control geochemistry, for quantifying local permeability and, in general, small scale heterogeneities (Stumm and Como, 2017b) (Maliva et al., 2009) (Dausman and Langevin, 2005).

Geophysics, both borehole logging and the non-invasive surface geophysics, help in reducing the costs of core analysis by either complementing core information and helping to extend it to the hole borehole (log), or by providing thorough coverage (electrical, electromagnetic, seismic, gravimetric). Among the former, natural and spectral gamma ray (NGR and SGR) logging, are widely used in hydrogeological practice (Serra, 2008). Geoelectrical methods are also widely used. They help define the geological structure and aquifer geometry, but they sound especially attractive for SWI because salinity contrasts should help in defining the extent of the seawater wedge. Unfortunately, loss of resolution causes a poor definition of the seawater wedge (Nguyen et al., 2009).

Hydraulic characterization is the approach of choice for quantitative evaluations because direct application of Darcy's law provides water fluxes. Unfortunately, its application is hindered by difficulties in estimating hydraulic conductivity and in measuring heads (e.g., Carrera et al. (2009)). Coastal aquifers provide a unique opportunity in tidal response tests, which consist of observing the aquifer head response to tidal and other (e.g., driven by wind or barometric pressure) sea level fluctuations (Carr and Van Der Kamp, 1969; Ferris, 1952). Tidal response tests sound ideal in that they are easy to perform and may provide information along the whole coast. Tidal response has motivated a lot of work to address the impact of heterogeneity, aquitard leakage or hydromechanical effects (e.g., (Alcolea et al., 2007; Guo et al., 2010a; Slooten et al., 2010)). In spite of that, tidal response tests are not widely used in hydrogeological practice.

Hydrochemistry and isotopes help in defining the origin of water, the chemical processes it undergoes, and how different waters mix in an aquifer. It is especially relevant in coastal aquifers because mixing of fresh and salt water drives numerous reactions, ranging from mineral dissolution or precipitation (Plummer, 1975) (Sanford and Konikow, 1989) to ionic exchange, sulfate reduction and methanogenesis (Andersen et al., 2005). The study of hydrochemistry is especially relevant for quantifying SGD, because one of the most widespread methods to calculate SGD fluxes rely on the quantification of natural radioactive tracers (Burnett, 2006; Beck et al., 2007; Charette et al., 2001; Rodellas, 2014). Radium ( $^{226}\text{Ra}$ ,  $^{228}\text{Ra}$ ,  $^{224}\text{Ra}$ ), and radon isotopes ( $^{222}\text{Rn}$ ) are the most popular due to its ease of detection and their capacity to trace processes occurring at different time scales because of the different semi-disintegration rates of the different isotopes (Kiro et al., 2015; Krest and Harvey, 2003; Lamontagne et al., 2015; Moore and others, 1996; Rodellas et al., 2017; Smith et al., 2012). While the method sounds attractive,

the variability of Ra concentrations measured in aquifers poses a question on its validity (Michael et al., 2011).

The summary of this long discussion is that the study of coastal aquifers is challenging and suggests that the coupling between different processes requires the integration of all of them. Small scale features must also be taken into account to be able to explain observed behaviors at bigger scales. In order to account for the mentioned scale effect and heterogeneity impacts, the implementation of hierarchical methodologies focused on the characterization of real-world aquifers is required (Werner et al., 2013).

This work proposes the characterization of a coastal aquifer using the four pillars jointly. To do so, we have developed a heavily instrumented site in the coast close to Barcelona, close to the mouth of the Argentona Stream, where SWI and SGD take place and the occurrence of radium and radon as natural tracers are relevant (Cerdà-Domènech et al., 2017). In this chapter, we report the characterization of this site.

## **2.2 SITE DESCRIPTION**

### **2.2.1 Geological situation**

The Argentona Stream is ephemeral and crosses the Catalan Coastal Range (CCR) towards the Mediterranean Sea. The CCR represents a tectonically elevated granitic horst that separates the Vallès depression from the coastal plain. The latter is part of an external depression developed mostly under the sea (IGME, 1976). Both structures are bound by two normal faults. One of these faults controlled the development of the Argentona Stream valley, which consists of Variscan granite and related plutonic rocks (granodiorites, tonalities, monzogranites, pegmatites, and dykes). The stream outlines a small Mediterranean catchment delimited by a relief reaching up to 632 m in the NE and by softened shapes, ranging between 300 and 400 m of altitude, due to the weathering and erosion of the granitic outcrops. In its lower part, the dynamics of the stream of Argentona and its tributaries have developed heterogeneous Holocene alluvial deposits composed of granitic sands, gravels, and silt coming from the granitic saprolite. Groundwater occurs in these recent alluvial deposits bounded by the sea at the coastline and where salt water mix with freshwater.

### **2.2.2 Equipment**

The Argentona Experimental site is located at the "seaside mouth" of the Argentona Stream (Figure 2-1). The site was designed so as to characterize SWI and SGD, with special emphasis in identifying mixing zone processes, especially Ra mobilization. Eighteen boreholes were drilled lay down in a cross-shaped distribution, following both

parallel and perpendicular orientations towards the sea, over a respective length of 30 m and 62 m, defining a total area of 1860 m<sup>2</sup>. The northeastern edge of the site starts at a distance of 42 m from the streambed, and its southeastern limit, 40 m inland from the coast. We arranged the distribution of the boreholes after a first electrical tomography survey, before the construction of the site. Preferential drilling in the direction transverse to the shoreline included 13 boreholes, having 9 of them grouped in 3 nests (N1, N2, N3) and other three additional piezometers (PP15, PP18, PP20). An additional branch to study transverse variability is formed by two piezometers (PS25 and MH) placed at the southwestern limit of the flood plain of the Argentona Stream and a complementary nest drilled close to the streambed (N4), at the same distance to the sea as N3.

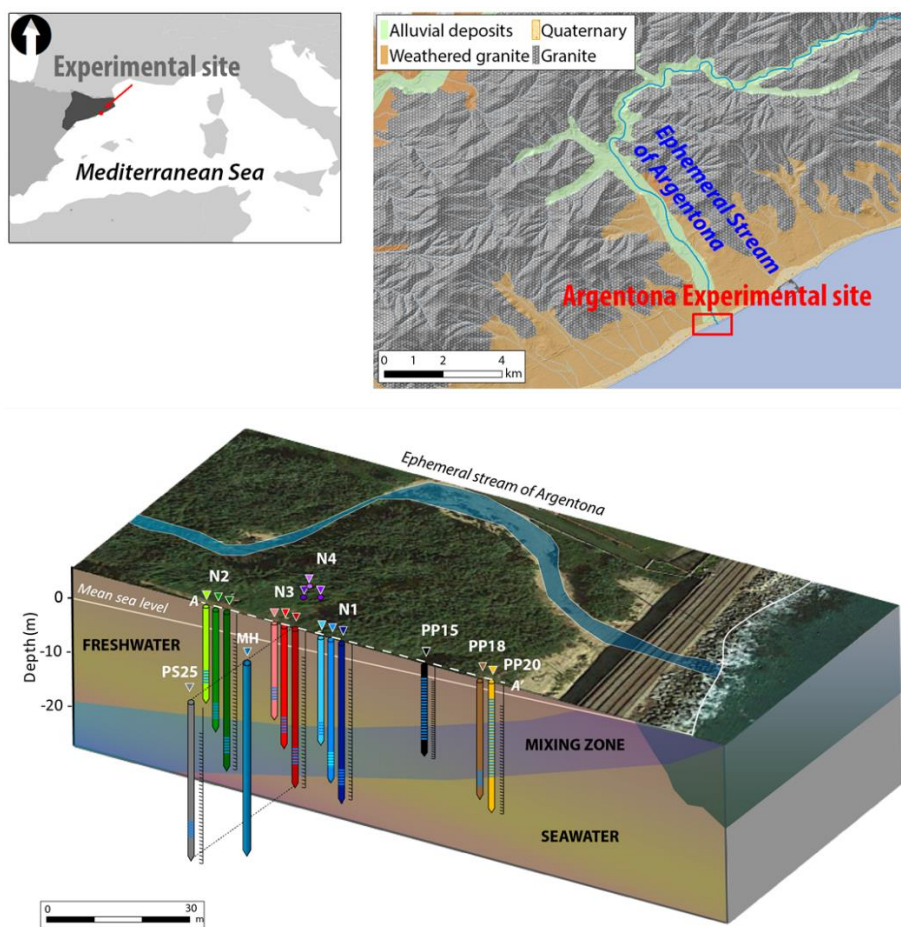


Figure 2-1- Localization of the experimental site and nests distribution.

Taking into account the theoretical 20-30 m thickness of the aquifer (Galofre, 1969), each nest is composed of 3 piezometers that cover different depths (around 25, 20, and 15 m, see Figure 2-1). This configuration lets us monitor the ongoing processes in the shallower, intermediate and deeper zones of the aquifer. All the boreholes were cased with a PVC tube of 3.5 inches of internal diameter, with a 2 m screened interval and a blind closed-end, excepting two fully slotted piezometers (PP15, PP20). The position of the screened

intervals coincided with the localization of the coarsest lens during drilling (see Table 2-1) at each predetermined depth, except for MH, which is a blind borehole fully filled with bentonite.

*Table 2-1.- Characteristics of the different types of boreholes and relation of logs performed. Being ECL: electrical conductivity logging, MSUS: Magnetic susceptibility, SGR: Spectral Gamma Ray, GR: total gamma ray, ERT: electrodes along the borehole. Among this instrumentation, all boreholes are equipped with FO.*

Type of well	Well name	Distance from the sea [m]	Depth [m]	Slotted interval [m]	Core recovery	Geophysics
Nest 1 (N1)	N1-15	62.9	16.5	12.5-14.5	No	ECL, MSUS, SGR
	N1-20	60.2	22.4	18.4-20.4	No	ECL, MSUS, SGR
	N1-25	62.3	24.8	20.9-22.8	Yes	GR, SGR ERT
Nest 2 (N2)	N2-15	97.9	14	10.0-12.0	No	ECL, MSUS, SGR
	N2-20	99.8	19	15.0-17.0	No	ECL, MSUS, SGR
	N2-25	98.3	25.6	20.0-22.0	Yes	GR, SGR ERT
Nest 3 (N3)	N3-15	80.1	14	10.0-12.0	No	ECL, MSUS
	N3-20	79.7	20	16.0-18.0	No	ECL, MSUS, SGR
	N3-25	78.1	25.3	18.0-20.0	Yes	GR, SGR ERT
Nest 4 (N4)	N4-15	82.0	17.19	10.4-12.4	No	ECL, MSUS, SGR
	N4-20	81.1	19	14.0-16.0	No	ECL, MSUS, SGR
	N4-25	82.6	25.2	18.2-20.2	Yes	GR, SGR ERT
Single	PP15	52.4	15	2.0-13.0	No	SGR, ERT
	PP20	39.5	20	3.0-18.0	No	SGR, ERT
	PP18	39.6	18	13.0-15.0	No	ECL, SGR
	PS25	83.3	25.1	18.0-20.0	No	ERT, MSUS, GR, SGR
	MH	83.3	28	-	Yes	ECL, SGR

All the boreholes in the experimental site are equipped with a permanent distributed temperature sensing (DTS) installation that consists of two lines of steel armored fiber optic cables placed around the piezometers (BRUsens cable Temperature, Brugg Kabel AG, SwitzECLand). Fiber optic installation enables measuring differences in temperature between fresh and saline groundwater bodies and thus registered spatial and temporal dynamics of the freshwater-salt water interface with high-definition (Folch et al., 2020). Also, in the deepest boreholes of each nest (N1-25, N2-25, N3-25, N4-25), and in PS25, PP15 and PP20, permanent geophysical downhole instrumentation was installed to characterize spatial variations in subsurface resistivity using cross-hole electrical resistivity tomography (CHERT). The equipment consisted of 36 permanent electrodes attached to the PVC casing with different spacing depending on borehole length (Folch et al., 2020). This installation also provided time lapse CHERT images (Palacios et al., 2019). In addition, in a specific borehole drilled up to 28 m depth and filled with bentonite (borehole MH) a downhole imaGeau observatory (Subsurface Monitoring Device, SMD)

was installed to study changes of electrical conductivity in pores with high resolution in space and time.

## **2.3 METHODS**

As mentioned in the introduction, the characterization included several techniques focused on the different aspects that influence SWI and SGD: geological heterogeneity, salinity and flow distribution and chemical reactions in the mixing zone.

We have tried them all, with different outcomes. We first assessed the subsurface structure of the aquifer at different scales, then the hydrodynamic response of the aquifer to the micro-tidal regime of the Mediterranean aquifer together with some hydraulic parameters and finally, the main hydrochemical processes including radium distribution.

### **2.3.1 Geological characterization**

We drilled some of the boreholes with core recovery to be able to characterize the bulk lithology of the aquifer. The material obtained from the deepest boreholes from each nest (N1-25, N2-25, N3-25, and N4-25) and MH, was described at centimetric scale and classified into different depositional sequences, based on the identification of fining upwards trends. Therefore, the main variations in lithology were observed with depth, while lateral continuity of the identified layers enabled to observe the same depositional sequences in the nearby boreholes.

Given this, we took 18 samples from borehole N1-25 to perform sediment characterization at small-scale. Sampling frequency was 1.2 m, discarding the upper 3 m of soil. To characterize the general geochemistry, petrophysics, and mineralogy of the aquifer, analyses on core included non-destructive and destructive techniques made on aliquots:

1. Sieve analysis was selected to determine the grain size distribution of 11 samples using a series of 7 progressively smaller mesh diameters, ranging from 5 to 0.1 mm.
2. Multi-point BET (Brunauer-Emmet-Teller) gas adsorption method (Brunauer et al., 1938) was selected to measure the surface area of the sediment.
3. The Cu-Trien method (Stanjek and Künkel, 2018) served to characterize total cation exchange capacity (CEC) and the amount of exchangeable cations (Na, K, Ca, Mg) to constrain ion-exchange reactions in the freshwater-salt water interface.

4. X-Ray diffraction was performed in subsamples using a Bruker D8 Advance diffractometer to assess mineral content.
5. Gamma spectrometry equipped with a high-purity germanium detector (HPGe) was used to measure radium isotopes ( $^{226}\text{Ra}$ ,  $^{224}\text{Ra}$ , and  $^{228}\text{Ra}$ ) to determine the bulk amount of radioactive tracers in the aquifer matrix and its variation with depth.
6. A Bartington MS2B sensor was used to evaluate the presence of ultrafine (<0.03  $\mu\text{m}$ ) magnetic minerals measuring magnetic susceptibility at two distinct frequencies.
7. Acid digestion ( $\text{HNO}_3$ ,  $\text{HF}/\text{HClO}_4$ ) was used to solubilize aliquotes of the sediments. Major elements (Al, Ca, Fe, K, Mg, Mn, Si, Na, Ti, P) were determined by Inductively Coupled Plasma-Atomic Emission Spectrometry (ICP-AES) using a Thermo Jarrel-Ash instrument, whereas trace metals (Ba, P, Sr and Ti) were determined by Inductively Coupled Plasma-Mass Spectroscopy (ICP-MS) using an X-series II Thermo instrument. The same analytical methods were later used for hydrochemical analyses (see Section 2.3.4).

### **2.3.2 Geophysical characterization**

Different logging techniques were used to characterize the petrophysical properties at borehole scale (Table 2-1).

1. We performed Natural Gamma Ray (NGR) in 8 boreholes to first characterize the sediments and establish the stratigraphic correlation between boreholes ( Figure 2-2). Later, Spectral Gamma Ray (SGR) was performed in 16 wells with the Antares Spectral Natural Gamma Probe Datensysteme GmbH, equipped with a BGO scintillation crystal (bismuth germanate). This tool enables geochemical logging by the registration of the K, U and Th curves for each logged borehole with a spatial resolution of 5 cm. The discrimination within the three elements allows obtaining their contribution to the SGR signal (Hesselbo, 1996) and hence localize zones in the aquifer with higher Th and U content that provide a potential source for natural tracers (radium) and K rich layers with high clay content (Schlumberger, 2009).
2. Magnetic susceptibility and electrical conductivity logs were obtained using the Geovista EM51 electromagnetic induction probe in the shallower piezometers with no permanent geophysical instrumentation (N1-20, N1-15, N3-20, N4-20, N4-15, N2-20, N2-15)(Table 2-1).
3. Magnetic susceptibility profiles provided the localization of fine-grained horizons, possibly rich in magnetic minerals and/or oxide alteration profiles (Dearing, 1994)

while the shape of electrical conductivity logs is mainly controlled by porosity and pore water salinity, which together with the conductivity of the rock determine the electrical conductivity of the formation ( $EC_b$ ) (Archie and others, 1942).

### 2.3.3 Hydrodynamic characterization

Hydraulic characterization usually entails measuring heads and hydraulic parameters, so as to assess water flow. We recorded head data every 15 min in every borehole using CTDs. An additional preexisting borehole belonging to the monitoring network of the Catalan Water Agency, placed some 500 m upstream, was monitored to serve as a boundary condition for hydrodynamic analyses. Given the difficulty of measuring hydraulic conductivity ( $K$ ) in the field, it is more frequent to derive transmissivity ( $T$ ) from pumping tests. Here, we used different methods to obtain parameters at different scales:

1. Hydraulic conductivity ( $K$ ) was determined at cm scale based on the grain size distributions of Section 2.4.1 using two different empirical relationships:  $K_{Hazen} = C_H(d_{10})^2$  (Hazen, 1911) and  $K_{Shepherd} = C_S d_{50}^j$  (Shepherd, 1989). The first relationship is frequently applied for sand as it relies on the effective grain size ( $d_{10}$ ). Coefficient  $C_H$  depends on sorting and ranges from 350 ( $K$  in m/d and  $d$  in mm) for poorly sorted to 1300 for well sorted sands (Fetter, 2018). The second one is meant for a broader range of sediment types (as reflected in coefficient  $C_S$  and dimensionless exponent  $j$ ) and relies median grain size ( $d_{50}$ ). And we have used  $C_S = 140$  and  $j = 1.65$  (Fetter, 2018).
2. Hydraulic parameters at borehole scale were obtained from short pumping tests using both drawdown and recovery data. Pumping tests were performed using an electrical suction pump and pressure transducers (Schlumberger, USA; Solinst, Canada) to monitor drawdown evolution. During the cleanup of the boreholes, after drilling and installation of the PVC piezometers, 17 single borehole tests of one-hour duration were carried out. These hydraulic tests enabled obtaining values of local transmissivity ( $T_{field}$ ) of the sedimentary unit of each slotted interval in the vicinity of the piezometers.
3. Hydraulic diffusivity at the experimental site scale can be derived from tidal response analysis (Slooten et al., 2010). We used the signal measured in boreholes, in terms of head variation, and compared them to sea level oscillations of the sea. First, we performed a filtering step to remove the effect of factors such as wind, atmospheric pressure, and waves. After all non-tidal noise was removed, a spectral analysis was applied to find the harmonics of sea tidal signal in the sea and in the boreholes, together with its main components. Tidal response is typically interpreted using the

method of (Ferris, 1952). The method is based on assuming an ideal homogeneous infinite aquifer, and that sea level fluctuates harmonically as  $h_s(t) = A_s \sin(\omega t)$ , where  $A_s$  is the amplitude of sea level fluctuations with frequency  $\omega$ .

$$h(x, t) = A_s e^{-ax} \sin(\omega t - ax) = A_s e^{-x/L_c} \sin\left(\frac{2\pi}{P}\left(t - \frac{P}{2\pi} \frac{x}{L_c}\right)\right) \quad (2.1)$$

where  $a = \sqrt{\omega S/2T} = \sqrt{\pi S/PT}$ ,  $P$  is the period ( $P = 2\pi/\omega$ ),  $L_c$  is the characteristic dampening depth  $L_c = 1/a = \sqrt{PT/\pi S} = \sqrt{PD_H/\pi}$ . Therefore, hydraulic diffusivity can be obtained either from the amplitude dampening ( $A/A_s = e^{-x/L_c}$ , where  $A$  is the amplitude observed in each borehole) or from the lag ( $t_{lag} = Px/2\pi L_c$ , where  $t_{lag}$  is the elapsed time between the sea fluctuation and the observation in the borehole). Since sea level fluctuations contain several harmonics, and dampening and lag depend on the period, we propose to scale them as  $\ln(A_s/A) \sqrt{P/\pi}$  and  $t_{lag} \sqrt{4\pi/P}$ . The resulting scaled dampening and lag should both equal  $x/\sqrt{D_H}$ . When plotted versus  $x$  (distance to the coast) they should align along a straight line. The slope of this line yields  $D_H$ , which should allow deriving a site scale estimate of transmissivity, assuming storativity known.  $D_H$  is a good indicator of connectivity (Knudby and Carrera, 2006): boreholes with low amplitude dampening and lag are well connected to the sea.

### 2.3.4 Hydrochemical and isotopic characterization

We collected 18 water samples, after a relatively dry period (the 22nd of January 2016) in different sampling points: all the boreholes excepting MH and PP18, seawater, and upstream fresh groundwater. Groundwater samples were obtained from different depths of the aquifer (see Table 2-1).

Hydrochemistry characterization proceed by first sampling the monitoring wells. Initially, we purged three times the volume of groundwater (between 110 and 40 L) contained inside the PVC tube of each piezometer to ensure the collection of formation water before sampling. A centrifugal pump was used to extract groundwater at a flow rate of  $0.5 \text{ L}\cdot\text{min}^{-1}$  to minimize colloids mobilization. We placed it in the middle of the slotted interval to minimize the impact of mixing with water within the borehole. We passed the pumped water through a multi-parameter probe to measure *in-situ* temperature, dissolved oxygen (DO), pH, Eh, alkalinity and water electrical conductivity ( $EC_w$ ).

Samples were filtered in the field using  $0.2 \mu\text{m}$  syringe filters before refrigeration and storage. Samples for cation analysis were mixed with 0.15 mL of ultrapure  $\text{HNO}_3$  to avoid mineral precipitation. Major ion and trace elements were analyzed by the ICP-AES and

ICP-MS equipment mentioned in Section 2.3.1. Phosphates (PO<sub>4</sub>, and total P) were determined by spectrophotometry while the rest of the nutrients (NH<sub>4</sub>, NO<sub>2</sub>, and NO<sub>3</sub>) and anions (Cl<sup>-</sup>, SO<sub>4</sub><sup>2-</sup>, Br<sup>-</sup>, F<sup>-</sup>) were analyzed by ionic chromatography.

On samples aliquots, we analyzed stable isotopes (<sup>18</sup>O and D). <sup>18</sup>O isotopic content was determined by equilibrium with a mixture of 0.3% CO<sub>2</sub> gas with He using a mass spectrometer of isotopic relations (MAT-253 Thermofisher) and D was analyzed by pyrolysis of the samples and analysis of the H<sub>2</sub> produced by separation and chromatographic column using a pyrolyzer coupled in continuous flow to a mass spectrometer of isotopic relations (TC/EA-IRMS Delta Plus XP Thermofisher).

Radioactive tracers activity was measured on specific groundwater samples taken in 11 different points of the aquifer perpendicular to the sea. 60 L of water were extracted from the piezometers to later filter them through MnO<sub>2</sub> fibers (Moore, 1976). Six different isotopes belonging to the disintegration chains of <sup>238</sup>U (<sup>226</sup>Ra, <sup>222</sup>Rn, and <sup>223</sup>Ra) and <sup>232</sup>Th (<sup>228</sup>Ra, <sup>224</sup>Ra, and <sup>228</sup>Th) have been measured. A Radium Delayed Coincidence Counter (RaDeCC) was used to quantify short-lived isotopes (<sup>223</sup>Ra and <sup>224</sup>Ra), while gamma spectrometry was used for long-lived isotopes (<sup>226</sup>Ra and <sup>228</sup>Ra). Other specific procedures detailed in Rodellas et al. (2015) were used to measure concentrations of <sup>222</sup>Rn.

## **2.4 RESULTS AND DISCUSSION**

### **2.4.1 Sedimentary structure**

The cores extracted from the deepest wells (N1-25, N2-25, N3-25, and N4-25) consist of granitic and siliciclastic sediments of variable grain size that often contain a sandy to silty matrix and are organized in packs of variable thickness, depending on the considered part of the experimental site. The correlation within the descriptions performed while drilling and the data obtained from NGR logs lead to the lithological cross section of Figure 2-2.

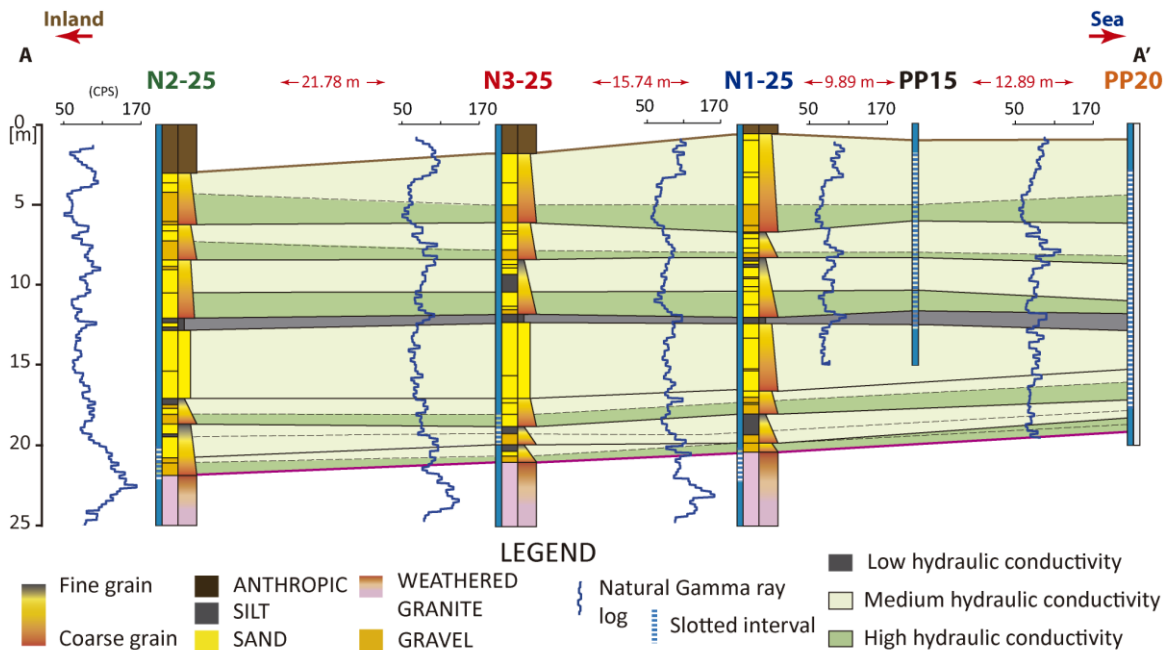


Figure 2-2- Lithostratigraphic correlation. Geological cross-section (AA', see Figure 2-1. Sea is to the right). Also shown are the gamma ray logs and the textural and mineralogical description from logs. It must be mentioned that the potential continuity of the bottom silt layers emerged from the interpretation of other data.

The most important feature of this figure is the arrangement of the layers in fining-upwards depositional sequences composed by coarse and fine sandy silica levels with variable proportion of silt. A total of 7 alluvial sequences have been differentiated. We found an intermediate continuous layer of silt located around 12 m depth, that separates an upper zone composed by 3 sequences of fining-upwards beds (coarse dominated, proximal facies) and a lower zone with other 4 sequences of equal type, but with finer grain size.

Other minor layers of silt have been found at the top of another two fining upward sequences at 7 and 17 m. The shallower coincides with the beginning of the second alluvial sequence. Which is also marked by the sharp augmentation in magnetic susceptibility logs (Figure 2-3), and resembles the end of the coarsest materials found in the aquifer.

Textural description highlighted four main sediment types: gravelly sand, sandy gravel, gravelly muddy sand and slightly gravelly sand (Folk and Ward, 1957). The sediments found are a combination of variable proportions of these textural groups, which composition varied from metamorphic and quartzitic to granitic. In the deepest part of the boreholes, the granitic component becomes dominant, as we reach the upper part of the basement weathering front. The composition of these sediments revealed an origin linked to the erosion and surface runoff of the weathered granitic outcrops present in the upper parts of the basin of the Argentona Stream.

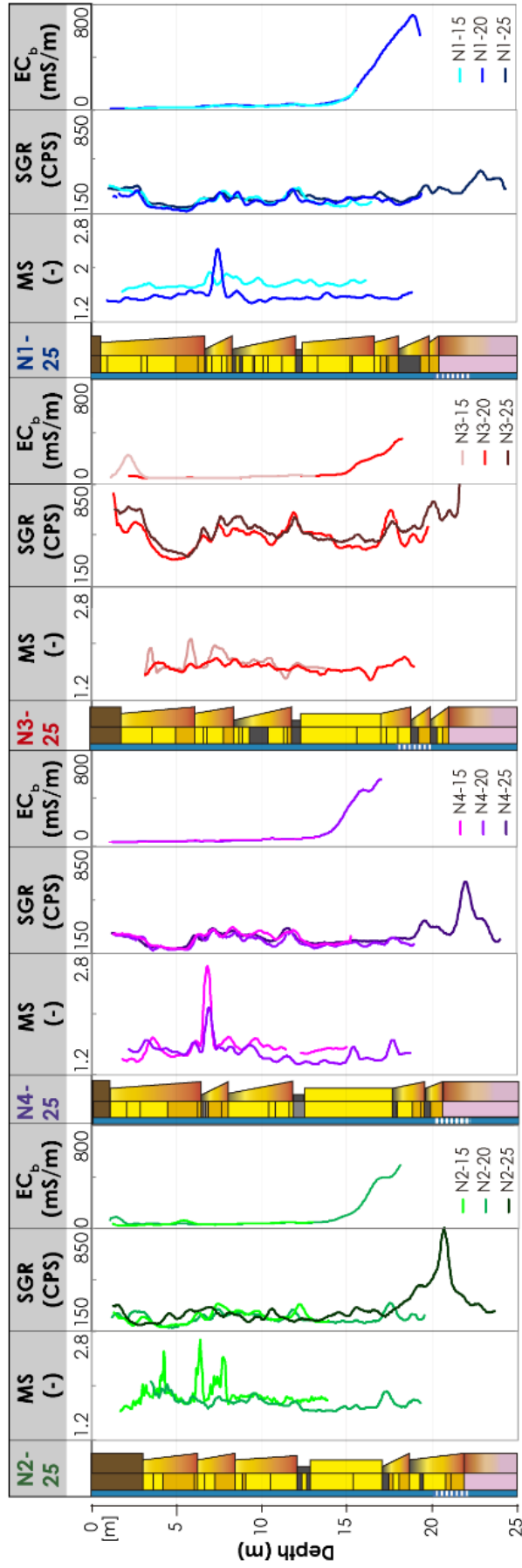


Figure 2-3 - Integration and correlation of logging techniques (MSUS: Magnetic susceptibility; SGR: Spectral Gamma Ray; EC<sub>b</sub>: Bulk electrical conductivity of the formation) and stratigraphic boreholes (25 m).

Alluvial deposits are usually considered isotropic and homogeneous in terms of geological formations. However, we cannot neglect the sedimentary dynamics that formed them, which usually develop abrupt lateral changes of facies. These variations in facies distribution can give rise to local confinement of the aquifer, transforming the medium into a highly heterogeneous and anisotropic ensemble (Huber and Huggenberger, 2016).

To characterize the geochemistry of the sediments, we analyzed in detail 18 core samples. Grain size distribution analysis performed in 11 samples (avoiding the continuous layer of silt) pointed out the presence of fine-grained sample at 7.5 m depth (sample n1-4) (Figure 2-4).

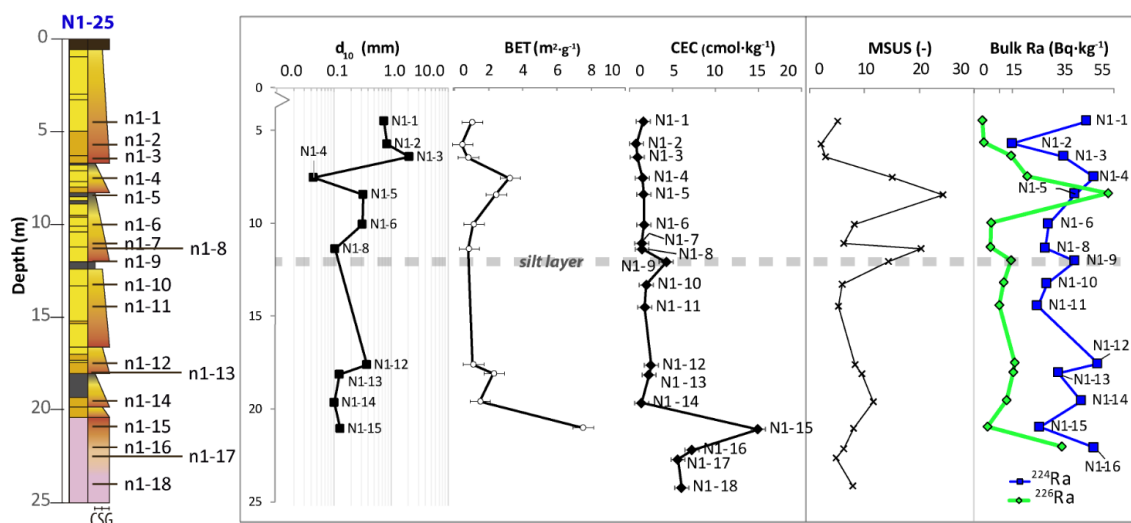


Figure 2-4 - Geochemical analyses made on core samples extracted from borehole N1-25.

The average grain size of the analyzed sediments is medium to very coarse siliceous sand (0.4 mm to 2 mm). General mineralogy consists of 56% of both sodium and potassium feldspar, 20.6 % quartz, 18.4% mica and 5% amphibole. Detailed mineral composition can be found in Table 2-2.

Elementary composition of the sediments and the distribution of major (Figure 2-5), and up to 44 trace elements, including Th and U, was obtained from acid digestions (see Table 2-2). Samples with higher Th and U were n1-3 (6.4 m depth) and n1-12 (17.5 m depth). The average composition of the samples of each slotted interval of N1 depicted higher Th in the intermediate borehole (N1-20) followed by the shallowest (N1-15) and the deepest (N1-25). U presented a different trend: the most enriched sediments (in decreasing order) are those coinciding with the slotted interval of N1-15, then N1-20 and finally N1-25. The results were also expressed in weight percentage, and confirmed the granitic source of the sediments, as  $\text{SiO}_2$  and  $\text{Al}_2\text{O}_3$  present the highest content (see

Figure 2-5). Prominent peaks of MnO, Fe<sub>2</sub>O<sub>3</sub>, TiO<sub>2</sub> and MgO, can be distinguished at 8.4 m depth (sample n1-5), 17.5 m, and at 19.5 m depth (samples n1-12 and n1-14). The general increase in oxides continues until 20.9 m depth (samples n1-15 and n1-16).

Table 2-2.- DRX of the extracted samples. Mineral composition in % of the different samples extracted from borehole N1-25.

Sample	Depth [m]	Quartz	Microcline	Albite	Illite	Lizardite	Clinocllore	Mg-hornblende Fe rich
n1-1	4.50	27.30	20.62	42.29	9.80	-	-	-
n1-2	5.70	19.49	26.74	31.08	22.70	-	-	-
n1-3	6.40	30.76	15.83	37.78	15.63	-	-	-
n1-4	7.50	14.46	33.70	31.33	16.77	-	-	3.74
n1-5	8.40	28.46	14.25	36.58	16.74	-	-	3.98
n1-6	10.00	17.66	24.14	30.72	20.78	-	-	6.71
n1-7	11.00	26.00	27.00	44.00	3.00	-	-	0.00
n1-8	11.30	13.71	18.55	37.34	23.57	-	-	6.83
n1-9	12.00	30.00	24.00	38.00	8.00	-	-	-
n1-10	13.20	28.00	24.00	21.00	26.00	1.00	-	-
n1-11	14.40	27.00	22.00	46.00	5.00	-	-	-
n1-12	17.50	18.51	26.87	38.03	13.17	-	0.33	3.09
n1-13	18.00	19.51	28.92	29.72	16.14	-	-	5.70
n1-14	19.50	18.48	31.79	35.27	14.46	-	-	-
n1-15	20.90	18.40	22.60	26.33	32.67	-	-	-
n1-16	22.50	15.00	10.00	35.50	38.00	1.50	-	-
n1-17	24.00	37.00	24.00	33.00	6.00	-	-	-

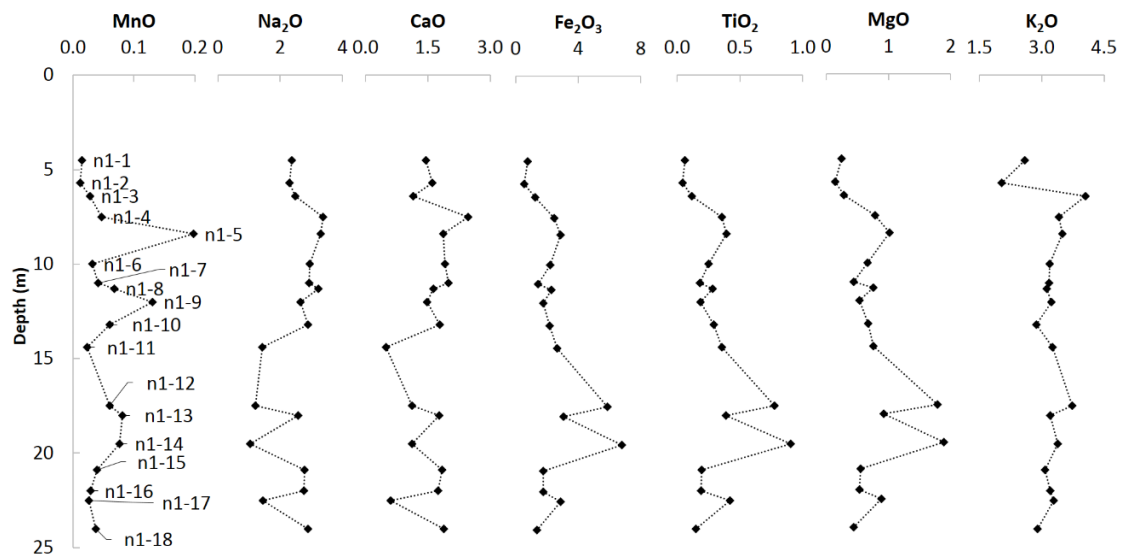


Figure 2-5 - Evolution with depth of the different oxides. Elemental composition expressed in weight percent of oxides obtained after acid digestion of the samples extracted from borehole N1-25.

Table 2-3.- Multielemental composition of the samples obtained from N1-25 in  $\mu\text{g g}^{-1}$ , including U, Th and trace elements from acid digestion.

Sample	Depth (m)	As	Ba	Be	Bi	Cd	Co	Cr	Cs	Cu	Ga	Ge	Hf	In	Mo	Nb	Ni	Pb	Rb	Sb	Sc	Sn	Sr	Ta
n1-1	4.5	1.39	422.85	1.30	0.08	0.04	1.28	81.38	1.13	5.16	10.48	1.08	1.52	<D.L.	0.79	1.93	4.39	11.46	76.14	<D.L.	2.34	0.93	137.51	0.21
n1-2	5.7	1.03	333.55	1.20	0.08	0.02	0.96	111.11	0.82	3.81	9.64	1.00	1.06	<D.L.	0.94	1.94	3.23	9.25	63.86	0.06	1.39	0.64	129.67	0.21
n1-3	6.4	1.98	273.37	1.82	2.84	0.07	1.90	87.50	1.95	18.62	12.53	1.98	2.28	0.03	0.95	4.73	3.23	61.66	115.76	0.10	4.20	5.35	101.99	1.02
n1-4	7.5	2.52	524.43	1.93	0.25	0.12	3.95	38.27	2.04	10.68	15.73	1.64	11.60	0.04	<D.L.	6.59	2.47	19.52	101.04	0.06	10.42	2.46	186.18	0.76
n1-5	8.4	2.85	545.11	1.73	0.31	0.10	8.15	24.49	3.05	11.90	15.52	1.63	7.50	0.04	1.25	6.81	6.80	20.64	110.19	0.08	9.04	2.55	155.63	0.74
n1-6	10	3.50	466.78	1.63	0.17	0.05	3.34	50.23	1.93	13.27	14.92	1.36	3.16	<D.L.	0.57	5.04	4.88	15.90	102.31	0.09	6.38	1.72	167.95	0.54
n1-7	11	1.17	497.81	1.55	0.65	0.04	2.49	64.83	1.52	10.10	13.61	1.28	2.13	<D.L.	0.75	3.61	4.18	14.91	93.78	0.06	4.41	1.62	177.77	0.47
n1-8	11.3	1.23	484.97	1.66	0.44	0.04	8.42	88.58	1.77	6.52	14.95	1.62	2.92	<D.L.	1.14	5.65	5.29	16.75	95.20	0.11	6.12	1.84	170.54	0.70
n1-9	12	2.04	562.47	1.46	0.22	0.05	6.77	64.24	1.57	26.51	12.86	1.28	2.36	<D.L.	1.63	3.66	8.20	15.40	95.88	0.12	5.11	1.55	151.17	0.37
n1-10	13.2	2.33	437.40	1.59	0.20	0.06	4.21	59.13	1.77	9.78	14.98	1.36	6.26	<D.L.	1.03	5.86	5.16	13.75	92.68	0.12	7.30	2.06	156.61	0.68
n1-11	14.4	3.54	498.75	1.48	0.25	0.04	3.70	34.60	2.50	10.52	15.10	1.33	4.22	0.04	1.02	6.44	4.01	15.35	112.62	0.15	8.93	2.33	76.70	0.68
n1-12	17.5	9.05	429.18	1.95	0.22	0.07	10.73	38.02	1.69	19.53	22.02	1.57	5.65	0.06	1.05	10.66	8.17	20.93	99.40	0.21	18.88	2.77	105.23	0.90
n1-13	18	1.83	483.98	1.57	0.32	0.05	6.02	35.54	2.76	11.00	16.58	1.31	2.33	<D.L.	<D.L.	6.73	5.03	16.72	108.85	<D.L.	8.27	2.04	169.16	0.73
n1-14	19.5	10.54	533.07	1.92	0.08	0.08	11.85	42.21	2.03	25.58	22.50	1.58	4.61	0.07	0.89	12.64	8.43	17.18	106.29	0.27	18.93	3.32	106.07	1.33
n1-15	20.9	2.22	485.92	1.46	0.13	0.05	3.14	46.86	1.55	6.95	13.43	1.35	2.70	<D.L.	0.60	3.72	3.18	14.68	91.59	<D.L.	5.58	1.54	163.64	0.43
n1-16	22.5	1.72	510.57	1.72	0.25	0.05	5.56	31.58	2.66	19.67	16.58	1.41	4.45	0.04	0.84	7.21	5.52	16.25	115.10	0.12	10.47	2.57	84.95	0.74
n1-17	24	<D.L.	442.27	1.52	0.17	0.04	2.69	57.51	1.48	6.63	13.74	1.19	2.05	<D.L.	0.78	3.17	3.50	12.60	92.02	<D.L.	4.41	1.24	171.32	0.32
n1-1	4.5	4.01	2.20	10.93	1.23	6.16	15.43	51.21	11.13	20.25	2.34	8.49	1.61	0.64	1.30	0.19	1.16	0.23	0.63	0.09	0.65	0.10		
n1-2	5.7	3.81	0.57	7.12	1.06	6.11	9.72	33.48	9.07	17.93	1.94	7.25	1.42	0.61	1.14	0.17	1.03	0.21	0.60	0.09	0.63	0.10		
n1-3	6.4	18.77	3.61	18.60	34.38	20.12	19.00	58.99	11.84	21.42	2.60	9.44	2.10	0.49	2.20	0.43	3.05	0.69	2.05	0.33	2.46	0.38		
n1-4	7.5	11.00	1.96	37.86	5.60	23.77	39.09	423.38	24.37	46.80	5.49	21.12	4.75	1.00	4.04	0.66	4.16	0.87	2.47	0.38	2.73	0.44		
n1-5	8.4	10.62	2.03	46.00	6.88	21.84	47.47	263.88	21.26	41.77	5.04	19.44	4.22	0.90	3.69	0.59	3.78	0.80	2.24	0.34	2.35	0.38		
n1-6	10	6.52	1.22	31.07	2.04	14.58	39.39	106.82	18.42	36.10	4.17	16.06	3.43	0.88	2.85	0.44	2.59	0.53	1.45	0.21	1.47	0.23		
n1-7	11	6.46	0.99	22.25	2.43	13.16	27.20	71.47	15.93	29.93	3.47	12.93	2.55	0.85	2.15	0.35	2.17	0.45	1.28	0.20	1.44	0.23		
n1-8	11.3	12.29	1.68	33.99	44.76	17.79	34.48	92.80	26.25	51.73	5.98	22.41	4.47	0.95	3.54	0.53	3.15	0.64	1.77	0.26	1.85	0.29		
n1-9	12	6.57	0.99	27.10	5.64	10.39	44.56	78.22	14.37	27.95	3.21	12.09	2.48	0.77	2.06	0.32	1.90	0.39	1.06	0.15	1.10	0.17		
n1-10	13.2	9.87	1.81	34.87	4.32	21.04	34.22	21.67	21.02	42.59	4.86	18.80	4.04	0.91	3.56	0.59	3.66	0.78	2.17	0.33	2.31	0.36		
n1-11	14.4	9.21	1.97	42.35	3.78	14.47	48.30	143.42	22.66	36.79	4.82	17.97	3.52	0.83	2.87	0.44	2.62	0.53	1.42	0.21	1.47	0.23		
n1-12	17.5	14.19	8.86	97.06	3.98	19.60	99.25	204.88	27.13	61.80	6.74	25.39	5.06	1.11	4.01	0.60	3.63	0.75	2.07	0.31	2.24	0.36		
n1-13	18	8.78	1.33	46.45	2.04	15.43	46.19	79.00	22.05	44.81	5.23	19.36	3.91	1.00	3.13	0.47	2.79	0.56	1.51	0.22	1.45	0.23		
n1-14	19.5	14.15	5.33	107.49	5.62	23.06	110.86	162.52	33.99	78.61	7.93	29.28	5.64	1.19	4.53	0.68	4.17	0.87	2.43	0.36	2.60	0.41		
n1-15	20.9	12.07	1.02	26.48	1.91	14.48	27.77	88.70	34.22	62.27	6.49	22.03	3.50	0.91	2.74	0.42	2.59	0.54	1.52	0.22	1.59	0.24		
n1-16	22.5	10.79	2.46	49.38	3.83	16.58	61.20	157.19	24.03	49.33	5.23	19.32	3.81	0.92	3.11	0.48	2.93	0.60	1.69	0.25	1.77	0.28		
n1-17	24	4.92	0.82	20.35	3.36	9.69	22.95	48.28	13.61	24.80	2.94	11.09	2.24	0.82	1.83	0.28	1.72	0.36	0.98	0.14	1.00	0.16		

The characterization of the internal structure of the sediments was completed using the BET surface analysis. Surface area is relatively constant at shallow depth ranging between 0.5 and 1.15 m<sup>2</sup>·g<sup>-1</sup>, excepting between 7.5 and 8.4 m, where it increases up to 3.2 m<sup>2</sup>·g<sup>-1</sup> (sample n1-4) (Figure 2-4). In the lower part of the aquifer, in sample n1-15, surface area presents its maximum value (7.53 m<sup>2</sup>·g<sup>-1</sup>), coinciding with the same depth of SGR maxima (20.9 m). This larger surface influences the measured CEC, which increases its value up to 14.8 cmol·kg<sup>-1</sup> at the same depth, while at the shallower part, the average CEC value is also low (1.58 cmol·kg<sup>-1</sup>). At 12 m depth (sample n1-9) there is another slight increase in CEC, that we attribute to the silt layer previously identified in the analysis performed at larger scale. The amount of exchangeable cations (Na<sup>+</sup>, Mg<sup>2+</sup>, K<sup>+</sup>, Ca<sup>2+</sup>) is also the highest at 20.9 m depth (sample n1-15). Below this depth, both total CEC and exchangeable Na<sup>+</sup> decrease again (samples n1-16, n1-17, n1-18) until an average value of 6.13 cmol·kg<sup>-1</sup>.

The analysis of long lived radium isotopes using gamma spectrometry depicted two different positive anomalies and trends depending on the isotopic decay chain considered (<sup>238</sup>U or <sup>232</sup>Th) (Figure 2-4). The maximum <sup>226</sup>Ra (U decay chain) activity was measured at 8.4 m depth (4.2 ppm, sample n1-5), coinciding with the higher values of the magnetic susceptibility logs. Th derived isotopes (<sup>228</sup>Ra) present its maximum (48.70 ppm) at 17.5 m depth (sample n1-12). Both isotopes present different trends: <sup>226</sup>Ra tends to decrease towards depth, while <sup>228</sup>Ra increases at the bottom of the borehole. This goes in the opposite direction of acid digestion results, and could be related to the ongoing geochemical processes that will be later discussed in Section 2.4.4.

Finally, the presence of finer (<0.03 μm) magnetic minerals was evaluated measuring the magnetic susceptibility at two distinct frequencies. Measurements on core showed two prominent peaks at 8.4 and 11.3 m of 24.4 and 20.35, respectively (samples n1-5 and n1-8, Figure 2-6), corresponded to the highest content of MnO, <sup>226</sup>Ra and magnetic susceptibility (in logs, Figure 2-4). The positive correlation between manganese oxides and radium (Gonneea et al., 2008) provided another tool to characterize of the most suitable zones of the aquifer to host exchange reactions that will affect Ra distribution. In those areas where the magnetic susceptibility is greater, the measured Ra activity is also the highest recorded in the entire profile (see logs and measurements on core in Figure 2-3 and Figure 2-4), which enables to use magnetic susceptibility logs as a proxy for radium in the aquifer. This lead to the localization of a source layer of radionuclides at 7 m depth, highlighted by a continuous anomaly in all the MSUS logs (Figure 2-3).

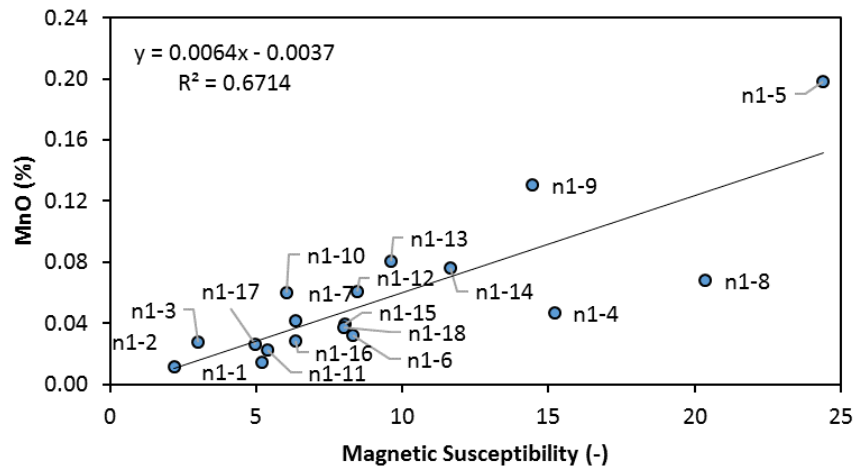


Figure 2-6- Magnetic susceptibility measured on core vs MnO % obtained after acid digestion of sediments.

## 2.4.2 Geophysical response of the aquifer

We describe here the results of logging surveys performed in the site. All types of logs are plotted together to facilitate comparison both among boreholes and among technologies (Figure 2-3) for N1, N2, N3 and N4 and Figure 2-7 for the other boreholes).

An increase in CPS can be observed in the deep portion of the gamma ray logs of all boreholes. We attribute this increase to the presence of weathered granite with fine materials and minerals containing a significant source of Th, U and K, as highlighted in Section 2.4.1. A broad minimum in CPS can be observed in the radioactive logs (NGR and SGR) top portion of all boreholes. This drop is typical of coarse grained materials. CPS decrease towards the bottom of the logs, which is most evident in borehole MH, that could be associated with the presence of non-matrix supported granitic sands. A small peak of 300 CPS in total SGR can be distinguished in all logs at a depth of 12 m, which supports the existence of a laterally continuous layer of fine-grained material (silt). Another continuous high response in SGR, with variations in intensity (270-340 CPS), can also be identified 7 m deep in all the boreholes. This led us to consider the presence of similar lithologies but with slightly different proportions of the same minerals. Another SGR peak can also be distinguished at 17 m depth in most deep boreholes, but it is less continuous than the other peaks and more marked in the inland extreme of the experimental site (boreholes PS25, N2-25 and N3-25). This peak resembles the occurrence of a less continuous level of silt affecting only the western-inland part of the experimental site.

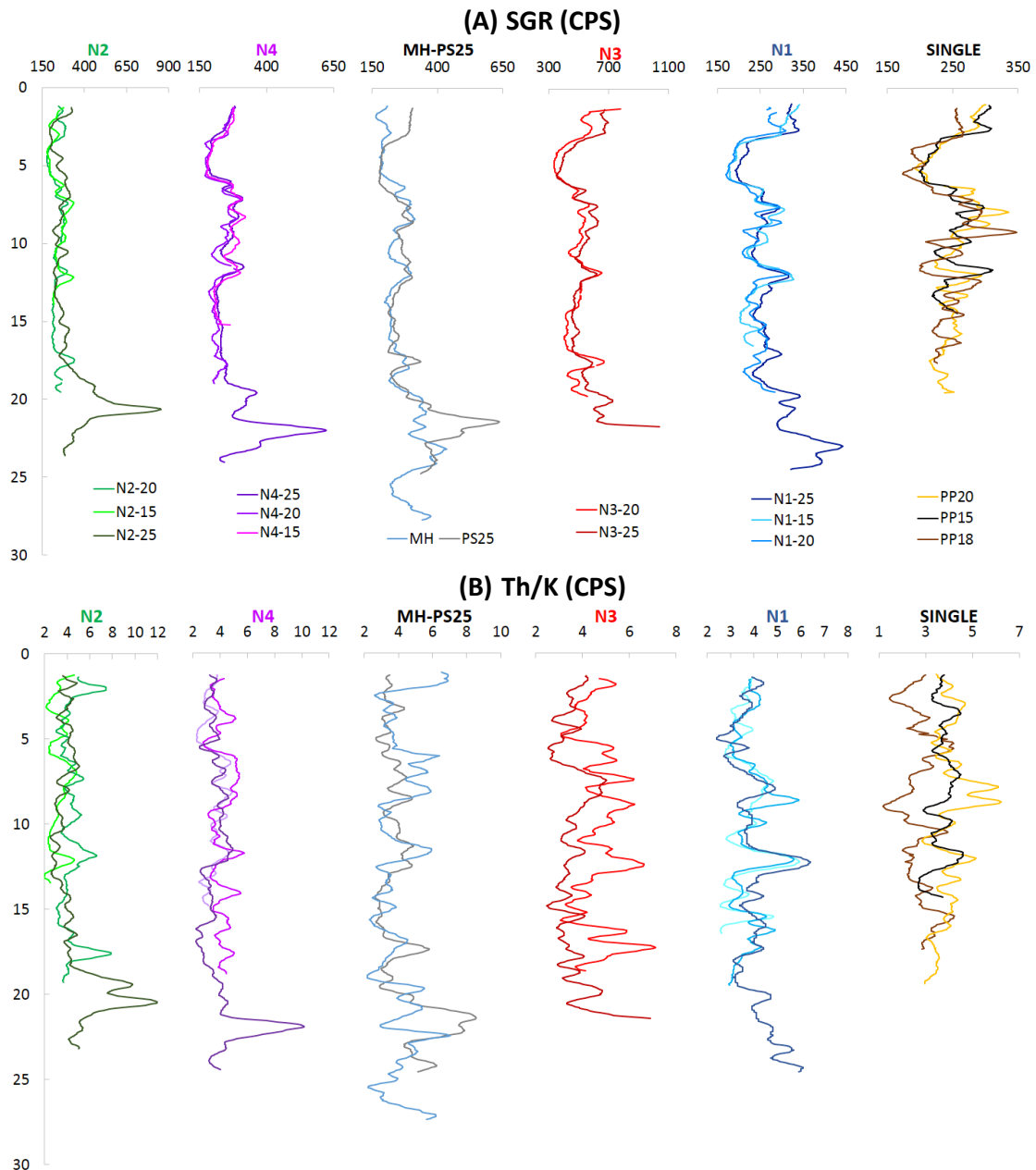


Figure 2-7- A) SGR Logs of all the boreholes. Total CPS from spectral gamma ray logs and B) Th/K ratios for each surveyed borehole.

This presumed lack of continuity in sedimentary bodies can also be seen by comparing SGR logs within a nest (boreholes separated a maximum distance of 1.5 m), where the opposite trend can be observed (in boreholes belonging to nests N2 and N3 and between MH and PS25). The occurrence of high and low CPS at the same depth may be a consequence of variations in lithology, which is a consequence of the heterogeneous sedimentological regime that generated an alternation of small coarser and finer sand lenses in this part of the site. Discrepancies in the vertical correspondence of logs may also explain this variability, as highlighted by (Rider, 1990).

Records of Th/K ratio can be obtained from SGR. They are included in Figure 2-7. Overall, they reproduce the patterns of SGR discussed above, but a bit noisy. This ratio displays

low values in the upper zone and peaks at 7, 12 y 17 m depth. The Th/K ratio reaches high values around 21 m in all deep (25 m deep) boreholes. This is consistent with the weathered granite core descriptions, but the ratio drops at further depths. Moreover, the magnitude of the maximums drop seawards (from 13.4 in N2-25 to 6.7 at PP20).

Bulk electrical conductivity generally increases with depth (see Figure 2-3). The sharp increase at 15 m depth in all logs can be attributed to the high  $EC_w$  of seawater entering through the permeable layer described before. Isolated peaks of higher  $EC_b$  than surroundings bulk conductivity can be identified at the same depth of those identified at 7 and 12 m in the SGR logs (Figure 2-3), which may reflect surface conduction at silt layers (Figure 2-8). Still the variability pattern is somewhat surprising. One would expect a more or less constant  $EC_b$  in the upper part, controlled by freshwater conductivity, and a more or less constant value at depth, controlled by seawater conductivity. In reality  $EC_b$  increased downwards also in the freshwater zone (see Figure 2-8).

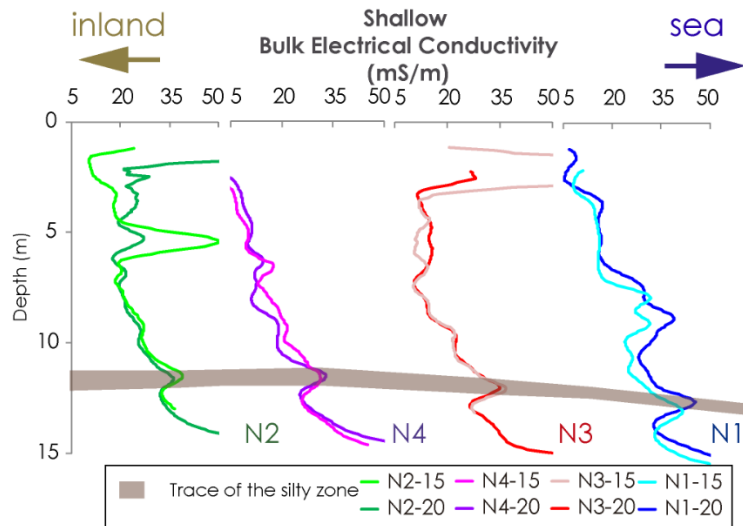


Figure 2-8 - Zoom in the freshwater zone of  $EC_b$  logs.

We attribute this increase to relict salinity from past intrusion events. A large increase can be observed at depth ranging from 15 m in nests N1, N3 and N4 to 20 m in the most inland nest, N2. This can be attributed to salt water, but it is non-monotonous. Bulk conductivity decreases further down in some boreholes (Figure 2-9), which suggests freshwater at depth. Magnetic susceptibility logs range from 1.2 to 2.8 SI. All the surveyed wells present an isolated sharp increase at around 7 m depth, more pronounced in N2-15, N4-15, N4-20 and N1-20. In N2-20 and N4-20, another slight increase can be found at 17 m depth.

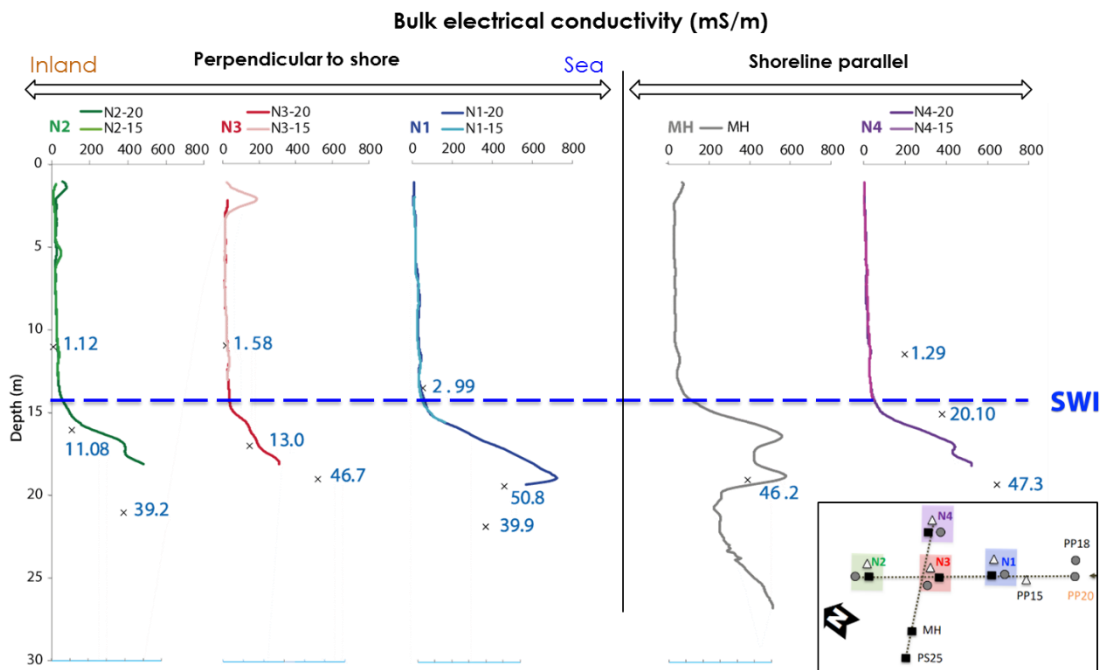


Figure 2-9- Relationship of induction logs and ECw.

### 2.4.3 Hydraulics

Hydraulic parameters were obtained at different scales and using different complementary methods that enabled obtaining transmissivity and hydraulic conductivity of the materials and the degree of connectivity of the different boreholes with the sea.

Table 2-4 displays hydraulic conductivity values obtained from grain distributions along N1-25, which may represent small scale conductivities. Values obtained with the Shepherd equation tend to be an order of magnitude larger than those of Hazen, but the two methods correlate quite well (correlation coefficient of 0.9 in log scale). What can be concluded is that hydraulic conductivity tends to decrease with depth and it is quite variable, as expected in this type of sediment, where fine grain layers alternate with coarse grained layers.

Table 2-4.- Hydraulic conductivity obtained from grain size analysis.

Sample name	Depth (m)	$K_{Shepherd}$ (m/day)	$K_{Hazen}$ (m/day)
n1-1	4.5	949.10	451.15
n1-2	5.7	437.84	505.17
n1-3	6.4	7973.68	3036.78
n1-4	7.5	10.93	0.84
n1-5	8.4	2098.17	85.27
n1-6	10	474.05	71.67
n1-8	11.3	53.66	3.89
n1-12	17.5	2167.91	110.96
n1-13	18	97.70	14.99
n1-14	19.5	9.81	4.37
n1-15	20.9	60.58	16.70

Table 2-5 displays borehole scale transmissivities, estimated from short pumping tests ( $T_{field}$ ), which may be representative of some 10 m ( $\sqrt{Kt/S_s}$ ) around the well for each sedimentary unit. Short pumping tests localized zones of low transmissivity in boreholes N1-25 and N2-25, which slotted intervals are placed in a deeper position with respect to the others. Intermediate boreholes present higher transmissivities than the rest, as also pointed out in the tidal analysis.

Table 2-5.- Results of the short pumping tests performed in each borehole.

Depth (m)	$T_{field}$ ( $m^2 \cdot day^{-1}$ ) PER NEST AND PIEZOMETERS						
	N2	N4	PS25	N3	N1	PP15	PP20
15	112	226	-	206	216	250	
20	218	249	-	578	125	-	568
25	9	107	324	223	3	-	-

These values are compared to those derived from grain sizes in Figure 2-10. It is clear that they do not compare well. However, this is consistent with our experience, transmissivities obtained from grain size distributions tend to underestimate those obtained from pumping tests. This could be probably because flow at borehole scale may be controlled by a few coarse layers that may have been missed during sampling, which may be biased because core extraction is more difficult for coarse layers than for fine layers.

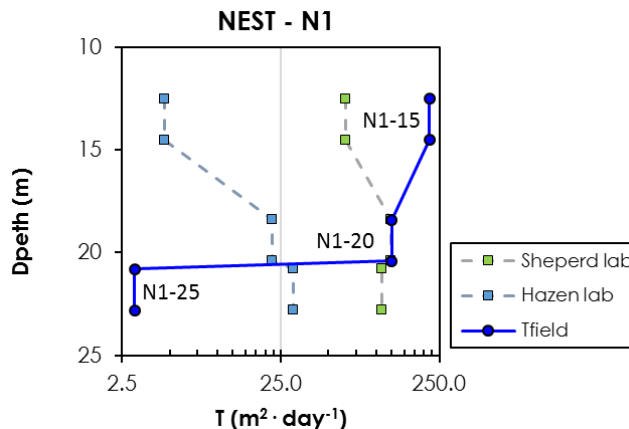


Figure 2-10 - Comparison of transmissivities obtained from grain size distribution (Hazen and Shepherd) and from hydraulic tests.

Results for the tidal response analysis are shown in Figure 2-11. The spectral analysis (Goyetche et al., 2020) identified the same set of harmonics in the boreholes and in the sea (Figure 2-11A displays semidiurnal, M2, and diurnal, K1 and O1, lunar components). The aquifer responds to sea level fluctuations, which suggests hydraulic connection to the sea. Plots of scaled lag and amplitude (Figure 2-11B and C, respectively) should fall on a straight line, passing through  $x=0$ . They do not. In fact, scaled lag data are scattered and do not appear to correlate with distance. This is hardly surprising because lag is

known to be affected by numerous factors (leakage among others, (Jiao and Tang, 1999; Li and Jiao, 2001); (Li and Jiao, 2002). What is surprising is that scaled lags are very short, in fact the shortest for 20 m deep observation intervals (circles in Figure 2-11B). We can only attribute this short lag to mechanical response, which is driven by the time derivative of sea level and thus tends to be half a period shorter than hydraulic response (Guarracino et al., 2012).

The conjecture of mechanical response is supported by amplitude dampening results, which are aligned when plotted versus  $x$  in Figure 2-11C, but the lines do not pass through the origin. We attribute this behavior again to mechanical response, which causes the amplitude at the coast to be half of the sea level amplitude.

In short, it is clear that the observed tidal response is not hydraulically driven, but mechanically driven. We conjecture that this observation reflects that the silt layers act as confining at the site scale. If we view the aquifer as a conventional unconfined aquifer, we would not expect this kind of response.

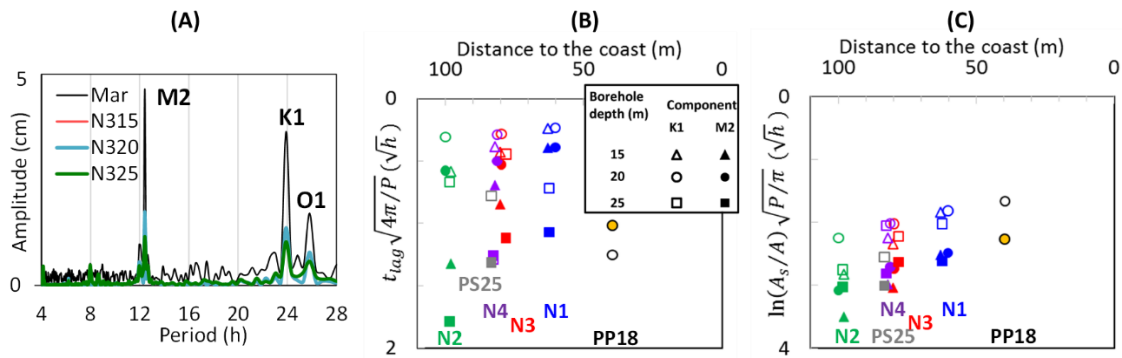


Figure 2-11 -. Results obtained from the tidal method: A) Spectra of the sea and N3 nest signals (Lunar semidiurnal, M2, and lunar diurnal, K1 and O1, components are apparent both in the sea and boreholes); B) scaled time lag and C) scaled dampening in each borehole versus distance to the coast calculated using the components with highest amplitude (hollow symbols for K1 and filled for M2). Under ideal conditions, all points should coincide on a straight line, identical for B) and C).

Regardless the method used, up to three layers of high hydraulic conductivity can be located at 6.4, 8.4 and 17.5 m depth (corresponding to samples n1-3, n1-5 and n1-12).

#### 2.4.4 Hydrochemical behavior

The spatial distribution of major ions, represented as Stiff diagrams, is displayed in Figure 2-12. All water samples are Na-Cl, except the freshest ones (shallow inland piezometers), which are Ca-HCO<sub>3</sub> and the intermediate wells of N3, N4, and N2 which are Ca-Cl. This picture is consistent with the conventional SWI Figure 2-1 (saline water at depth and freshwater above, with Ca enrichment in the saline portion as a result of cation

exchange). It is also consistent with depth variations of other parameters, shown in Figure 2-13.  $EC_w$  measured from water samples tends to increase with depth as expected. However, the increase is non-monotonic at the nests closest to the coast, with higher  $EC_w$  between 15 and 19 m depth (N1-20 and PP20) than the deepest piezometers (N1-25 and N2-25). We attribute this non-monotonic increase of  $EC_w$  to the presence of discharging freshwater flows through permeable layers, making the mixing zone of the aquifer, a complex and irregular transition zone, far from the paradigm of Figure 2-1. Note that these fluctuations appear to be caused by the silt layer at 17 m depth, so minor that it went unnoticed during core description and was only identified from the SGR logs, so that it must be considered a relatively minor heterogeneity feature of an otherwise homogeneous alluvial aquifer. DO was low in all samples, but lowest in the deep boreholes ( $0.10 \text{ mg}\cdot\text{L}^{-1}$  in PS25). This, together with the increasing concentrations of Fe ( $1.42 \text{ mg}\cdot\text{L}^{-1}$  in N1-25) and Mn ( $0.34 \text{ mg}\cdot\text{L}^{-1}$  in N3-25) evidence the strong reducing character of deep saline water (Figure 2-13). pH was also low, much lower than the end-members freshwater (7.8) and seawater (8.09) and tends to decrease with depth, showing an increasing acidification in the lower part of the aquifer.

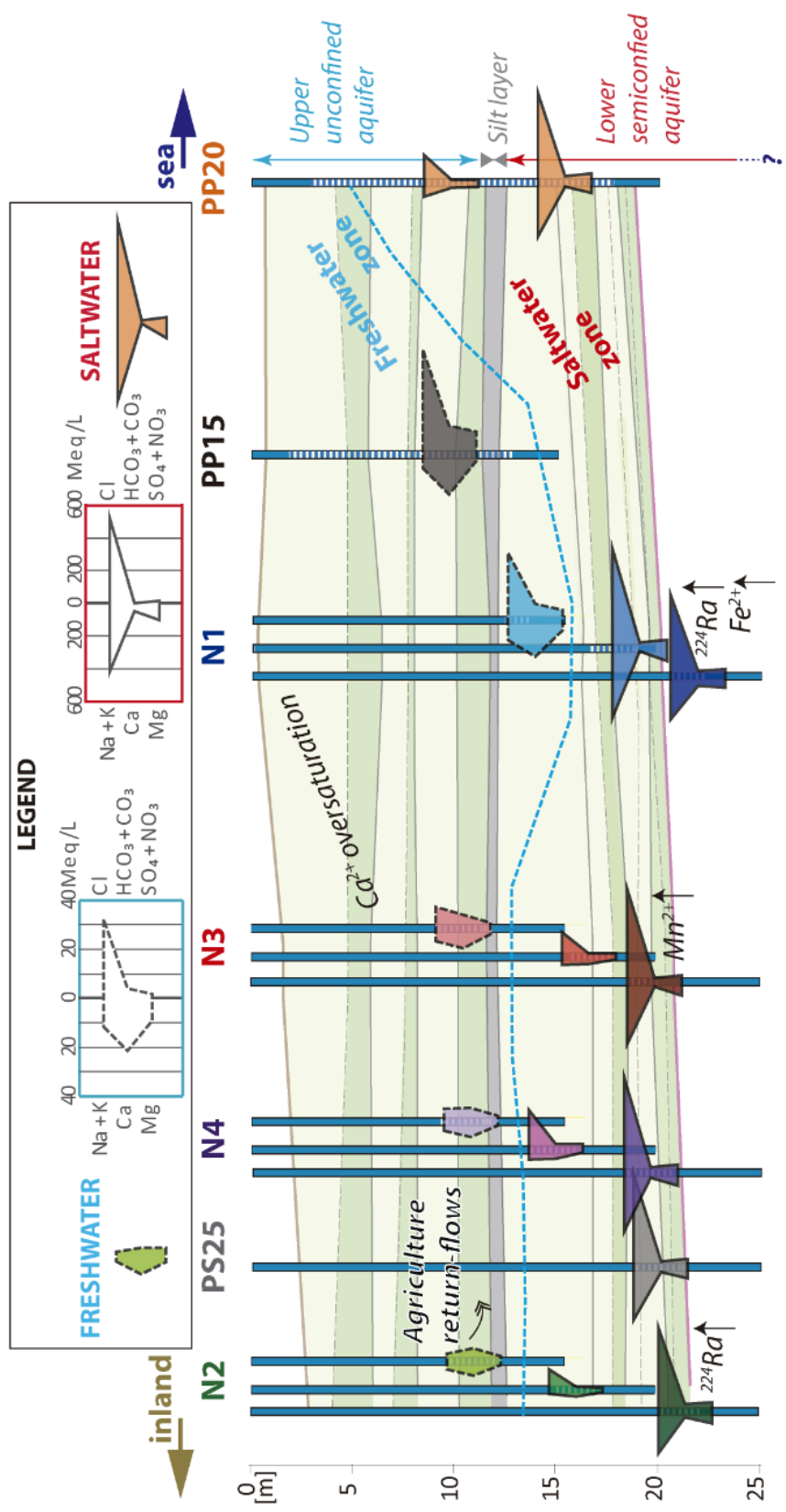


Figure 2-12 – Cross-section of the aquifer with stiff diagrams of each sampling point.

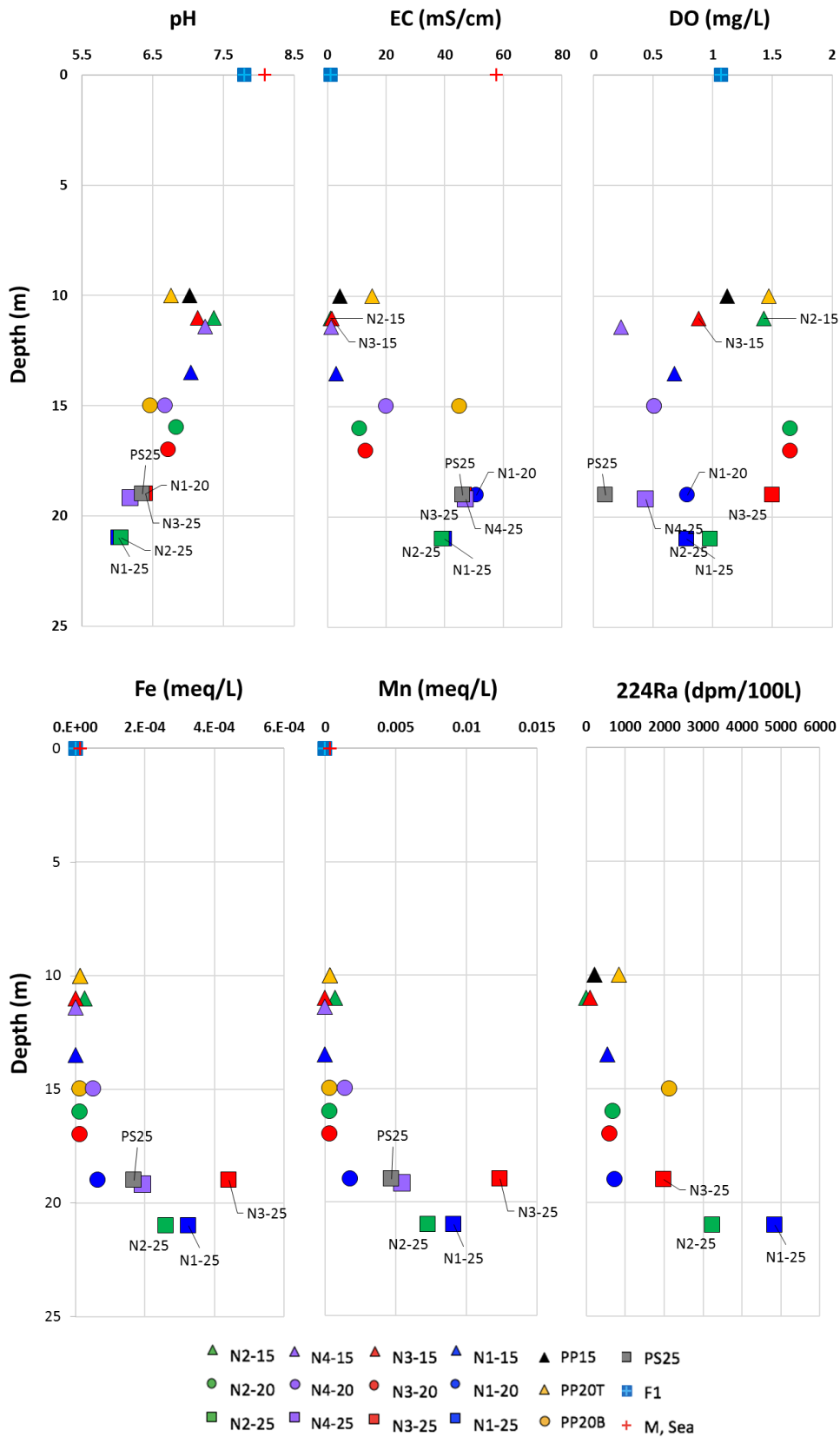


Figure 2-13 - Evolution of the measured parameters with depth.

Major, and some minor, ions are plotted versus Cl<sup>-</sup> in Figure 2-14 and presented in Table 2-6. Chloride, total cations and stable isotopes suggest that our samples are mixtures of FW and SW. All species differ from the conservative mixing line in all samples. Departure is maximum in the deepest boreholes, slotted between 19 and 22 m depth. The enrichment in Ca<sup>2+</sup> is accompanied by the depletion in Na<sup>+</sup> and K<sup>+</sup>, which suggests cation exchange processes (Russak and Sivan, 2010). This observation is further supported by the fact that total cations do act as conservative when expressed in meq/L (Figure 2-14). The drop of Na<sup>+</sup> with respect to the mixing line is especially dramatic in wells of N2-25 and N1-25, which we attribute to the adsorption of Na<sup>+</sup> on the surface of the sediments and release of Ca<sup>2+</sup> that occupies high proportions of exchangeable sites. A possible source of Ca<sup>2+</sup> can be provided by the occurrence of granitic saprolites characteristic of this region (Bech, 1977). Increases of Ca<sup>2+</sup> have been traditionally attributed also to the dissolution of interstitial carbonate and gypsum cement contained in the sandy matrix of the aquifer, or the hydrolysis of plagioclase and hornblende (Santucci et al., 2017a). Carbonate dissolution is indeed possible, but gypsum dissolution is unlikely. Sulphate values fall below the mixing line, which suggests precipitation, which may well occur in response to the dramatic increase of Ca<sup>2+</sup>.

Table 2-6.- Groundwater major element concentrations in mg · L<sup>-1</sup>.

Well name	Sampling Depth (m)	Ca <sup>2+</sup>	Mg <sup>2+</sup>	Na <sup>+</sup>	K <sup>+</sup>	Cl <sup>-</sup>	SO <sub>4</sub> <sup>2-</sup>	NO <sub>3</sub> <sup>-</sup>	Sr <sup>2+</sup>	F <sup>-</sup>	Fe <sup>2+</sup>
F1		147	27	42	2.5	66.7	103	94	0.41	0.19	0.11
M. Sea		410	1310	11200	271	21700	971	0.57	7.72	1.09	0.01
PP15	10	436	112	270	5.69	1150	58.9	15.4	2.14	0.17	0.04
PP20	10	764	396	2000	28.2	5100	222	16.4	4.74	0.27	0.05
N1-15	13.5	323	75.8	224	5.23	799	55	16.2	1.59	0.32	0.02
N3-15	11	165	37.3	124	5.68	256	46.9	18.3	0.65	0.24	0
N4-15	11.4	133	27.2	94.8	2.47	143	50.1	21.3	0.5	0.23	0.01
N2-15	11	117	23.8	84.2	4.23	88.6	47.5	21	0.37	0.22	0.59
PP20	15	1250	1170	7790	115	16500	672	3.06	10.6	0.16	0.01
N1-20	19.4	973	1260	9670	134	18600	795	0.38	9.96	0.15	0
N3-20	17	1090	370	1320	16.9	4360	153	9.28	5.46	0.17	0.06
N4-20	15	1580	560	1920	24.8	6940	233	7.54	7.73	0.17	0.03
N2-20	16	1050	313	821	13.1	3670	115	9.97	4.87	0.2	0.01
N1-25	21.87	1700	1170	6110	153	15100	515	0.52	14.2	0.07	1.42
N3-25	19	995	1240	8430	153	17500	666	2.16	11.2	0.16	0.41
N4-25	19.2	1180	1270	8200	142	17800	686	0.15	11.5	0.14	0.04
N2-25	21	1550	1310	6210	128	15200	471	0.14	13.6	0.11	0.48
PS25	19	1200	1170	7370	103	17200	675	0.65	11.2	0.14	0.06

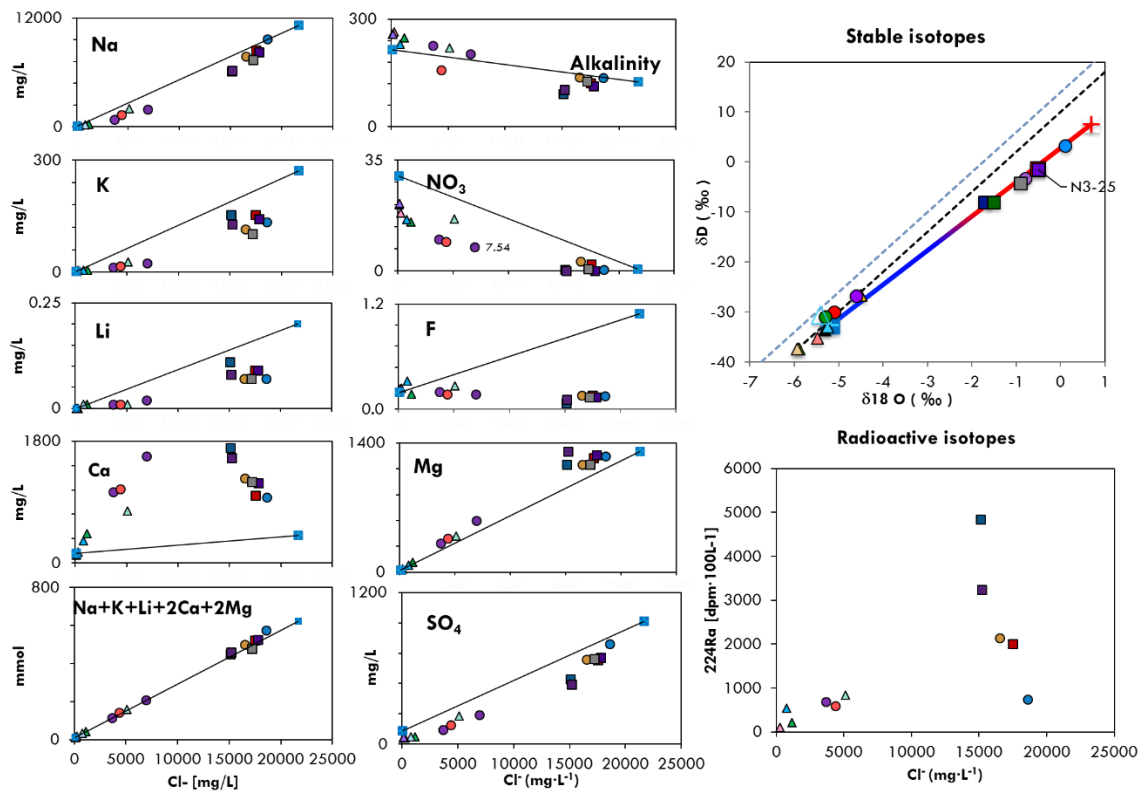


Figure 2-14 - Hydrochemical characterization: Ionic relationships of the different elements (in  $\text{mg}\cdot\text{L}^{-1}$ ) (A).  $\delta^{18}\text{O}$  vs  $\delta\text{D}$  values for 16 sampled piezometers, freshwater and seawater. The seawater mixing line has been represented in degradation from blue (fresh) to red (saline). Isotopic composition of precipitation in Barcelona has also been represented (B). Radium activity measured in the wells. No freshwater samples or seawater samples were analyzed (C).

We have analyzed both stable isotopes and Ra isotopes (Figure 2-14). The former are typically used to identify the different sources of groundwater (Gat and Gonfiantini, 1981); (Clark and Fritz, 2013).

Stable isotopes in the different indicate a pure mixing of two extreme waters (freshwater and seawater samples). In the experimental site,  $\delta^{18}\text{O}$  ranges from  $-5.93\text{‰}$  (N4-15) to  $0.70\text{‰}$  (sea) and  $\delta\text{D}$  concentrations present values from  $-37.99$  (N215) to  $7.50\text{‰}$  (sea). Upstream freshwater has a concentration of  $-5.18$  for  $\delta^{18}\text{O}$  and  $-32.6\text{‰}$  for  $\delta\text{D}$ . All the samples fall below the local meteoric water line (LMWL) defined by Neal et al. (1992), and fall along the freshwater – seawater mixing line. Isotopic values obtained from the shallower boreholes (between 10 and 19 m) plot along the global meteoric water line (GMWL), whereas boreholes from 19 to 22 m below the surface, fall below. Isotopic values of precipitation are similar to samples taken from shallower sampling points, pointing out that rainfall is the main recharging mechanism in the shallower piezometers (between 10 and 19 m depth), with some mixing processes between depleted  $\delta^{18}\text{O}$  and  $\delta\text{D}$  water and seawater. Values of the deepest piezometers (from 19 and 22 m depth) and two intermediate piezometers (PP20B and N1-20) tend to be more enriched in  $\delta^{18}\text{O}$  and  $\delta\text{D}$  relative to shallower boreholes (boreholes from 10 and 19 m).

The composition of the recharging waters can also be modified as a consequence of the agricultural activities that take place few kilometers upstream. The slightly high nitrate concentrations (see Figure 2-14) and the low ratio Cl<sup>-</sup>/Br<sup>-</sup> of 95.27 observed in the shallower inland borehole (N2-15) are characteristic of agriculture-return flows (Bear et al., 1999).

Special attention was paid to the characterization of radium distribution within the aquifer, which is typically considered homogeneous in the inland component of the SGD (Michael et al., 2011). We observed different activities of <sup>224</sup>Ra, <sup>228</sup>Ra, <sup>228</sup>Th, <sup>226</sup>Ra, <sup>222</sup>Rn and <sup>223</sup>Ra depending on the sampled zone of the aquifer. Here, we will focus on the distribution of <sup>224</sup>Ra (Figure 2-14). <sup>224</sup>Ra activities display a linear correlation with Cl<sup>-</sup>, as expected (Webster et al., 1995) in low to moderate salinity samples. But outliers can be found in the high salinity samples. In the following we will analyze this in detail:

1. The maximum activities measured in N1-25 and N2-25 (4845.27 and 3244.14 dpm·100L<sup>-1</sup>) do not coincide with the highest EC<sub>w</sub> (Table 2-7). Instead, <sup>224</sup>Ra maxima correspond to the zones of the experimental site where pH is lowest (6.02 and 6.03, Figure 2-15). In these zones bulk Ra activities measured on core are higher as a consequence of the proximity of the granitic weathering front. Moreover, grain size and transmissivity are small. We conjecture that these less transmissive zones at N1-25 and N2-25 may provide a suitable environment for <sup>224</sup>Ra accumulation in water via alpha recoil.

Table 2-7.- Measured parameters and characteristics of the “anomalous” piezometers in terms of radium concentration. Note that radium measurements (in Bq·kg<sup>-1</sup>) were performed on core extracted from borehole N1-25.

Well	Depth (m)	Distance to the sea (m)	Water measurements				Sediment measurements		
			pH	Na <sup>+</sup> (mg·L <sup>-1</sup> )	EC (mS·cm <sup>-1</sup> )	<sup>224</sup> Ra (dpm·100L <sup>-1</sup> )	<sup>224</sup> Ra (Bq·kg <sup>-1</sup> )	<sup>226</sup> Ra (Bq·kg <sup>-1</sup> )	<sup>228</sup> Ra (Bq·kg <sup>-1</sup> )
N1-25	21	78.11	6.02	6110	39.9	4845.27	25.80	14.6	36.6
N2-25	21	98.37	6.06	6210	39.20	3244.14	-	-	-
N3-25	19	83.31	6.4	8430	46.70	1999.96	-	-	-
N1-20	19	39.58	6.4	9670	50.80	741.60	37.8	19.4	35.4

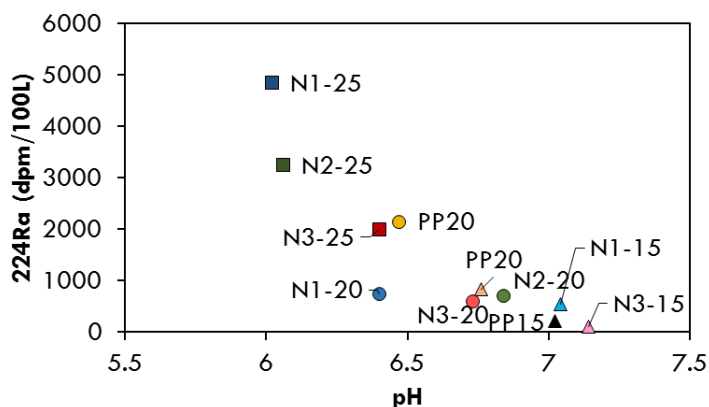


Figure 2-15 - Relationship of  $^{224}\text{Ra}$  and pH.

2. The lowest concentrations of  $^{224}\text{Ra}$  observed in saline waters ( $\text{EC}_w$  between 46.7 and 50.8  $\text{mS}\cdot\text{cm}^{-1}$  in boreholes N3-25 and N1-20 respectively) are located in zones with higher pH (6.4) (Figure 2-13).
3. Additional constraints on radium activities are exerted by groundwater composition, as can be observed in two sampling points (N3-25 and N1-20) where pH is the same (see Table 2-7, Figure 2-15). Despite its higher salinity, N1-20 is depleted in  $^{224}\text{Ra}$ . The slight differences in groundwater composition may be the main cause, as some elements, such as Fe and  $\text{NO}_3$  present strong affinity for radium (Gonneea et al., 2008). This is coherent with groundwater composition measured in N3-25, which presents considerable amounts of Fe ( $0.41\text{ mg}\cdot\text{L}^{-1}$ ) and  $\text{NO}_3$  ( $2.16\text{ mg}\cdot\text{L}^{-1}$ ), whereas in N1-20 the values measured were lower or absent.

Another factor that contributes to having depleted radium zones is a direct consequence of the higher hydraulic conductivity of the sediments: more permeable sediments are formed by sands and gravels with larger grain diameter, which avoids exchange reactions to occur, limiting radium desorption. However, in the lower part of the aquifer we can find sediments with higher BET surface area and CEC (Figure 2-4) that enhance exchange reactions. In this zone, we also encounter high  $\text{Na}^+$  concentrations in water ( $8430$  and  $9760\text{ mg}\cdot\text{L}^{-1}$ ) that might be scavenging Ra from the surface of the sediment as a consequence of the strong affinity of both ions to be exchanged (Webster et al., 1995).

In the intermediate zone of the aquifer, and coinciding with the continuous silt layer identified at 12 m, we noticed a different cation exchanger highlighted by the analysis performed on core (Figure 2-16). In this zone of the aquifer, where we still have freshwater, the exchangeable  $\text{Na}^+$  remains constant with depth, although the total CEC increases (sample n1-9). This makes radium activity higher in the solids (as highlighted in bulk isotopic measurements, Figure 2-4) because the exchange cation is other different from  $\text{Na}^+$  and salinity remains low, keeping radium attached to the surface sediment, and

activities in groundwater, low. In depth, the different behaviour is observed, both exchangeable  $\text{Na}^+$  and CEC increase and bulk radium decreases (see Figure 2-4).

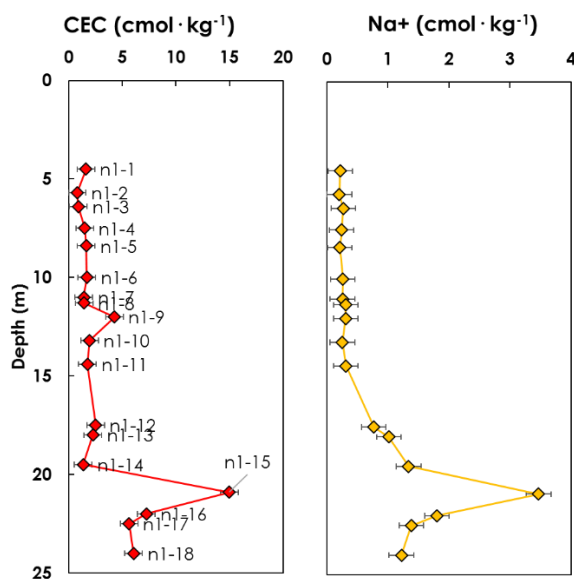


Figure 2-16 – Evolution with depth of the CEC and exchangeable  $\text{Na}^+$  measurements performed on core.

## 2.5 SUMMARY

The original goal of this work was to establish a conceptual model of the Argentona coastal aquifer integrating geological, petrophysical, hydraulic and hydrochemical information. This combined effort resulted in a series of conceptual reconsiderations.

Geophysics yielded the most important surprise: identification of four levels of freshwater discharge below salinity lenses, presumably representative of SWI wedges. Deep freshwater discharges are frequently found in multi-aquifer systems, but the Argentona aquifer is by all accounts, a typical fluvial aquifer. This finding contradicts the traditional SWI, a topic that is further analyzed in Chapter 3.

Geology was also surprising. We expected coastal deposits, but found that the aquifer consists of alluvial sediments. It has been discussed since long whether the aquifer in this region lies over Holocene deposits (controlled by sea level fluctuations during the last 15000 years) or a granitic basement (Villarroya, 1986). Both alternatives have implications towards flow. Holocene coastal deposits are often underlain by highly permeable packs of gravel, thus facilitating deep freshwater discharge. A granitic basement can be affected by different degrees of weathering (saprolite), and depending on the considered portion of the saprolite, it may contain layers that can act as flow barriers or conduits. We assumed the former (Holocene deposits), but found the latter (granitic basement), although we have not identified yet the possible high permeability layer

predicted by Dewandel et al. (2006) beneath the weathered zone, which will be the subject of future campaigns.

Hydraulics was surprising in that tidal analysis led us to conclude that aquifer head fluctuations in response to sea level fluctuations were largely mechanical, rather than driven by hydraulic connection to the sea. This cannot occur if the aquifer is unconfined, as originally expected. We attribute mechanical response to the semi-confining effect of the silt layers, which is consistent with the importance of these layers for freshwater discharge discussed above. This finding has forced us to revise traditional methods for analyzing tidal response data (Goyetche et al., 2020).

Hydrochemistry yielded a huge chemical activity in the mixing zone. All samples appear to be a mixture of freshwater and seawater, as reflected by stable isotopes, Cl, and total cation equivalents. But mixing is affected by other processes. The most marked impact was cation exchange driven by the penetration of seawater, which is frequent in the SWI literature ((Liu et al., 2017); (Zhang et al., 2017); (Santucci et al., 2017b; Xue et al., 2000)). Cation exchange leads to the enrichment in Ca, but our Ca concentrations are very high second only to those of (Boluda-Botella et al., 2008 and Santucci et al., 2017b). All anions appear to suffer from some dissolution/precipitation process. The presence of dissolved Fe and Mn implies that redox processes are important and may explain the unusually low pH. It is not clear if this activity reflects some special feature of our site or if it is a feature of the level of detail of our analysis. Both alternatives are possible. The Argenton site is special in that it does not consist of coastal, but fluvial, deposits. It is also special in that a portion of groundwater (at least the shallowest samples) appear to come from wastewater that bypasses the treatment plant during flood events, which would explain the highly reducing conditions at the site (but not so much that these conditions are maximum at the seawater rich samples of boreholes N1-25 and N2-25). But the opposite is also possible, perhaps what we have found is unusual in that we have looked in an unusual detail. It is clear that further research is needed.

Chemical complexity has hindered the study of radium as a tracer of continental water discharge. Radium concentrations correlate with salinity, as expected. But other factors (pH, sediment composition and grain size) also affect radium distribution within the aquifer.

As a consequence of the complex structure of the aquifer, hydrochemical sampling was not enough to fully characterize the chemical processes in the aquifer. The patterns observed in chemical species distribution with depth and with respect to  $EC_w$ , showed a high degree of aquifer-rock interaction.

Heterogeneity is often a source of unexpected behaviors. Since heterogeneity is an essential feature of nature, surprise is an ever-present feature of conceptual modeling (Bredehoeft, 2005). What is surprising is that all “four pillars” of hydrogeology yielded some surprise, which suggests not only that we were originally quite ill-oriented in our expectations, but also that conventional SWI views need to be revised. Certainly, SWI deserves further research.

We want to make a final comment on the usefulness of the different characterization techniques used in Argentina. What set us on the track was the analysis of tidal response and, specifically, the fact that observed responses required mechanical coupling, which did not make sense in an unconfined aquifer. The fact that our “single” aquifer was indeed working as a multi-aquifer system, at least at the site scale, was confirmed by induction logs and best visualized by CHERT. Except for CHERT, which had never been used in SWI studies, these techniques are well known, but less frequently used. Traditional techniques (core descriptions, hydraulic tests, head measurements, and hydrochemical sampling) were of limited use for conceptualization. This is not meant to imply that traditional techniques should not be used (basic geology and properties are derived from core descriptions and core sample analyses; hydraulic parameters are needed to quantify fluxes; and hydrochemical analyses are required for understanding chemical processes). What we want to convey here is that (1) these traditional techniques are best when complemented by others; (2) tidal response analysis is informative and cheap; (3) induction or, in rocks, formation resistivity logs are also cheap and informative about freshwater and seawater circulation, which has been advocated by many authors since long ago (see, e.g., Buckley et al., 2001; Church and Granato, 1996) (Custodio, 1995)); and (4) time lapse CHERT is particularly enlightening, although it requires furnishing boreholes with permanent electrodes.

The questions arisen in this work may help in the design of new experimental sites that involve the quantification of SWI and SGD. Our case can thus serve as a benchmark for further characterization of alluvial coastal aquifers.

## **Chapter 3.**

Questioning the traditional paradigm for  
seawater intrusion: evidence from salinity profiles



### 3.1 INTRODUCTION

Coastal zones concentrate human activities and subject coastal aquifers to heavy pumping, which promotes the entrance of seawater (SW). As a result, seawater intrusion (SWI) is becoming a global problem (Michael et al., 2017). The issue is also relevant to submarine groundwater discharge (SGD), which is relevant to support marine ecology (e.g., (Cho et al., 2018; Knee and Paytan, 2011; Rodellas et al., 2015)) and tends to drop with increasing pumping or land-use changes (Rufi-Salís et al., 2019). Proper management requires to understand how SW enters the coast and characterizing the implications of this entrance in real coastal aquifers. To this end, a good paradigm (i.e., a simplified and clear example that captures the essence and can be used to draw generalizations) is useful.

The traditional SWI paradigm is largely based on the observations made by (Ghyben, 1888; Herzberg, 1901) that states that groundwater in coastal wells reaches seawater salinity at a depth approximately equal to 40 times the freshwater head above sea level (Du Commun, 1828). The model was formalized by Henry (1964), who showed that seawater penetrates the aquifer below exiting freshwater, developing a wedge (Figure 3-1). A mixing zone develops between fresh- and salt-water and brings seawater back to the sea, thus causing the SWI wedge to behave as a circulation cell (Figure 3-1a). The picture can be complicated by the presence of big intertidal regime (Figure 3-1c) (Lebbe, 1983) or aquitards (Figure 3-1b) (Guo et al., 2010a). Numerous improvements and refinements have been made to this model (Bakker et al., 2017; Pool and Carrera, 2011; Post and Werner, 2017; Werner et al., 2012). With the exception of Michael et al. (2016), who showed that heterogeneity may complicate this picture, the paradigm of Figure 3-1 has remained essentially unchallenged and has formed the basis for coastal aquifer management.

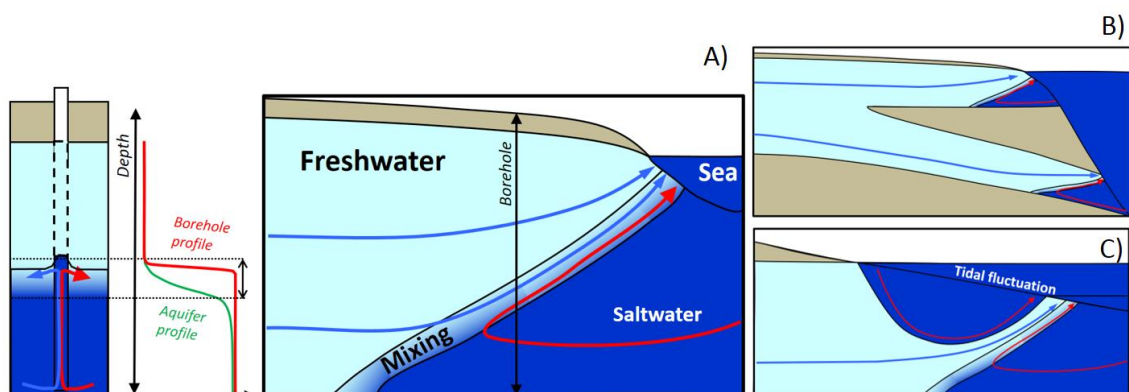


Figure 3-1 Traditional SWI paradigm that can be found in textbooks (e.g., (Bear et al., 1999; Custodio and Llamas, 2001); (Domenico and Schwartz, 1998), for a homogeneous steady state aquifer with a fixed sea boundary and correspondent salinity profiles (A) or a multi-layer aquifer (B) and for a significant tidal range (C). (This figure has been inspired by Jiao and Post (2019)).

The distribution of salinity is the natural indicator to monitor the status of coastal aquifers with respect to SWI, regardless of the SWI paradigm. It can be characterized using different methods. Surface non-invasive geoelectrical techniques are widely used because they give a picture of the SWI extent at a moderate cost (Falgàs et al., 2011a; Falgàs et al., 2009). Electrical resistivity tomography (ERT) is probably the most widely extended method to visualize salinity (actually bulk formation electrical conductivity,  $EC_b$ ) distribution within the aquifer (Abdul Nassir et al., 2000). Airborne electromagnetics can also be used for large scale coverage (Goebel et al., 2019; Kirkegaard et al., 2011; Paine, 2003). These techniques can be used to map the extent of seawater intrusion, but provide poor resolution capacity and tend to underestimate  $EC_b$  at depth (Nguyen et al., 2009). Resolution is improved by cross-hole methods (Palacios et al., 2019), but they require installing electrodes at the well casing, which is costly. Formation electrical conductivity can also be measured from induction logs (IL) in closed PVC wells (Buckley et al., 2001; Church and Granato, 1996; Lebbe, 1999; Stumm and Como, 2017a), and many others have advocated the use of IL to overcome the masking impact of groundwater flow along the borehole long-screen wells. In fact, for the same reason, clusters of short-screen wells should be preferred in general to monitor contamination (see reference to discussion on the topic in the 1980s by Church and Granato (1996)).

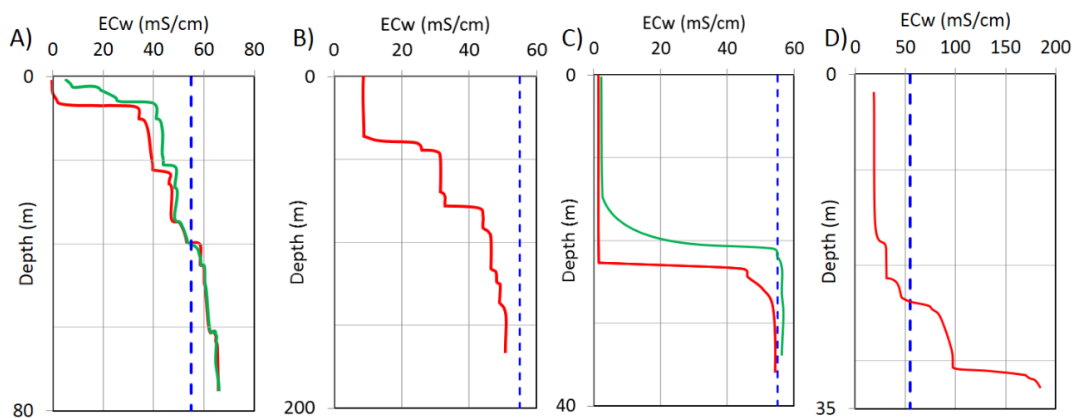


Figure 3-2. Examples of salinity profiles performed in Y. Liu, Jiao, Liang, and Kuang (2017) (A), Buckley et al. (2001) (B), Shalev et al. (2009) (C) and Yechieli et al. (2010) (D). The average  $EC_w$  of western Mediterranean Sea is marked with a blue line. Red and green lines represent salinity profiles obtained at different times.

Despite the above, the most widely spread technique for characterizing depth to seawater remains the water salinity log in long-screen or uncased holes (Bear et al., 1999; Liu et al., 2016; Yechieli et al., 2010). The main advantage of this approach is the ease of measurement (recording simply requires lowering an EC probe inside the well) and the fact that it can be applied in most of the wells, which are mainly drilled for pumping and thus long-screened. Another nice feature of salinity profiles is that they appear to yield the position of the saline interface together with its width and localization. In fact, salinity

profiles are monotonous (i.e., water electrical conductivity,  $EC_w$ , increases with depth) and display sharp jumps in salinity (a few typical examples are displayed in Figure 3-2). Field hydrogeologists have usually interpreted these jumps as representative of the seawater interface.

Numerous researchers have criticized salinity profiles for a broad range of reasons. Beyond the traditional criticism to sampling from long-screen wells due to borehole flow caused by the cutting units with different heads discussed above (Buckley et al., 2001; Custodio, 1995; Church and Granato, 1996), SWI causes specific difficulties. The most apparent one is that, in the paradigm of Figure 3-1A, the salinity profile represents an equilibrium within the well (in red), which does not need to coincide with the aquifer (in green) (Carrera et al., 2009; Shalev et al., 2009; Tellam et al., 1986). In fact, since seawater flows upwards in the seawater wedge of Figure 3-1a, so does seawater in the lower portion of long-screen wells. The result is that the jumps in salinity profiles are (1) above the actual mixing zone in the aquifer (Shalev et al., 2009), (2) anomalously sharp (Abarca et al., 2007; Tellam et al., 1986) and fluctuations of the salinity jump in response to tides display much larger amplitude than expected (Levanon et al., 2016). Another surprising feature with respect to the paradigm of Figure 3-1a is that salinity profiles often display stepwise shapes (see Figure 3-2). Salinity jumps have been traditionally linked to flow driven by head differences and they are frequent in fractured media, where those jumps can be associated with discrete fractures inflow (e.g., Buckley et al. (2001)). But stepwise profiles are also frequently found in unconsolidated sediments (e.g., Liu et al. (2016)).

The most surprising feature of salinity profiles is that they rarely reach seawater salinity (see Figure 3-2). If the traditional paradigm was true, deep salinity should be equal to seawater, regardless of recirculation problems within the well. The fact that surface ERT tends to yield lower than expected  $EC_b$  at depth makes things worse, in that it suggests that water salinity is lower than that of seawater at depth. It is clear that the paradigm needs revision.

We have observed these kinds of problems at our non-tidal SWI research site in Argentona (Folch et al. (2020); Cerdà-Domènech et al. (2017)). The objective of this chapter is to present our salinity profiles and the explanation we have found for their shape, which leads us to question the traditional SWI paradigm.

## **3.2 CHARACTERIZATION METHODS**

The Argentona Experimental site is a field laboratory dedicated to studying SWI and SGD. It is placed in the eastern Mediterranean coast, in an alluvial coastal aquifer above a

weathered granitic basement. The sedimentary bodies found in this aquifer respond to the deposit of fast flood events. The aquifer contains several silt layers, mainly at the top of fining upward sequences. In Chapter 1 a detailed description of the aquifer can be found.

The site is instrumented with 18 boreholes with PVC casing drilled at different depths. The casing for most of the boreholes is slotted only in a 2 m interval (at 2, 3 or 5 m from the piezometer bottom, depending on the borehole, see Figure 3-3) to enable representative fluid sampling as discussed in the introduction. In two boreholes located close to the sea (PP15 and PP20) were furnished with larger slotted intervals to test the acquisition of realistic salinity vertical distribution within the aquifer using different methods. An additional blind borehole (MH) was drilled to install a subsurface monitoring device.

Seven of these boreholes were also equipped with stainless steel mesh to shelter electrodes placed at a distance ranging between 0.4, 0.5 and 0.7 m, depending on the total length of the well (Folch et al., 2020) and to be able to perform cross hole electrical resistivity tomography (CHERT) (Palacios et al., 2019). The disposition of the electrodes along the borehole also enables us to perform vertical resistivity profiles around the well.

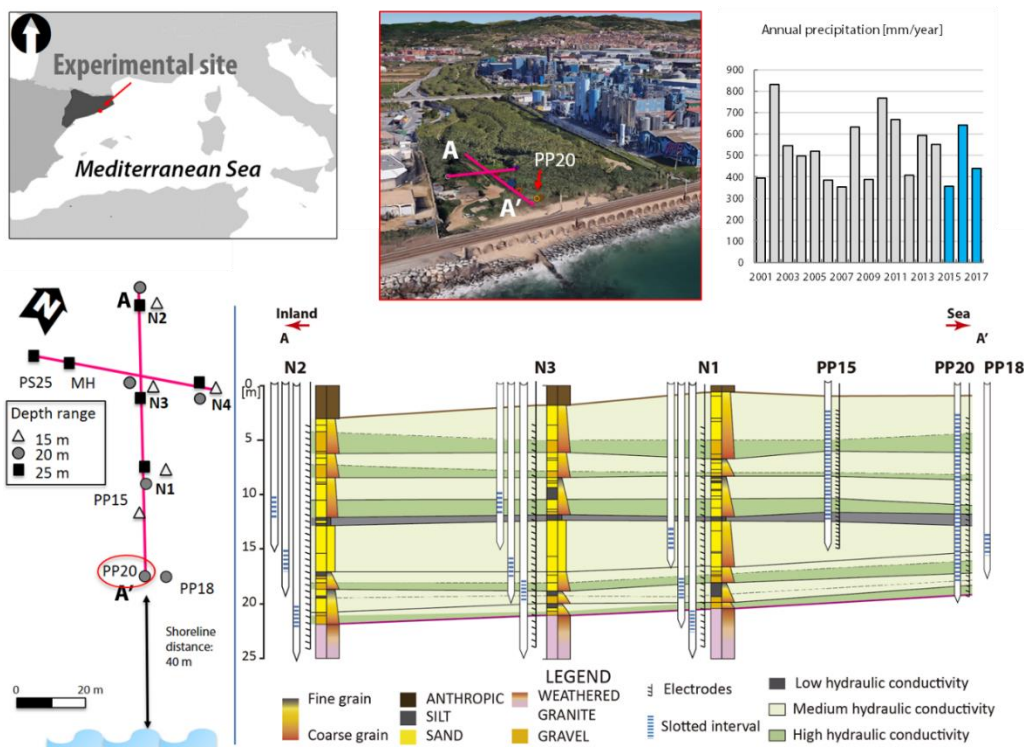


Figure 3-3 Localization of the Argenton Experimental site, annual precipitation regime (Average for the period 2001-2017: 584.1 mm), disposition of the wells and cross-section A-A' with the geology and localization of piezometers slotted intervals.

We implemented different measurement techniques to characterize the aquifer at different scales. Pumping tests indicated aquifer transmissivities between 3 and 400 m<sup>2</sup>/d. Cross-hole pumping tests and piezometric characterization were also carried out. Aquifer

characterization included geophysical campaigns (Spectral Gamma Ray and Induction logging) and hydrochemical sampling in different periods (see **Table 3-1 Geophysical acquisitions**.Table 3-1). Water samples were collected after purging the volume of water contained in the PVC tubing to ensure the collection of formation water, and placing the pump in the middle of the slotted interval in the different piezometers of each nest. Water was sampled at two different depths in the long-screen well placed close to the coast. Fluid logging was carried out using a multiparametric probe to measure  $EC_w$  variation with depth and Induction logging was performed in boreholes without electrodes. A complete description of all the geophysical, geochemical, hydrodynamical and hydrochemical characterization can be found in Chapter 1. Temporal analysis of the data relying on geophysical campaigns (resistivity and temperature variations with time) can be found in Palacios et al. (2019) and Folch et al. (2020).

### **3.3 RESULTS: SALINITY PROFILES**

Here, we analyze 8 salinity profiles (Figure 3-4) performed between 2015-2017 in the nearshore long-screened boreholes (PP20, see Figure 3-3).

Salinity profiles of 8 seasonal periods performed between 2015-2017 in the nearshore long-screen borehole (PP20, see Figure 3-3) are shown in Figure 3-4. Figure 3-4 A displays the profiles performed in spring 2015. The first one (May, 21st, 2015) was recorded after two days of rain (32.7 mm), and no rain occurred before the second one (June, 8th, 2015). The saline interface rose 1 m (black arrow in Figure 3-4A) in only 19 days.  $EC_w$  at depth increased from 41.9 mS/cm to 47.3 mS/cm. The salinity of the upper 6 m on the May, 21st, 2015 profile is above the salinity immediately below, which is surprising because a high salinity implies a higher density and dense water should sink into light (low salinity) water. Note however, that the salinity between the 6 m depth and the 15-17 m jump is too high for fresh water (5-10 mS/cm, which is representative of brackish water). A similar profile was measured on October, 27st, 2015 (Figure 3-4C). Both profiles were measured two days after a 32 mm rainfall and are also the ones that present the deepest sharp jump in salinity. We attribute the increase at the top to storm surges and/or the presence of past saline aerosol and saline crust from past storm surges and the descent of the salinity jump to the increase in freshwater discharge caused by the rainy-day recharge.

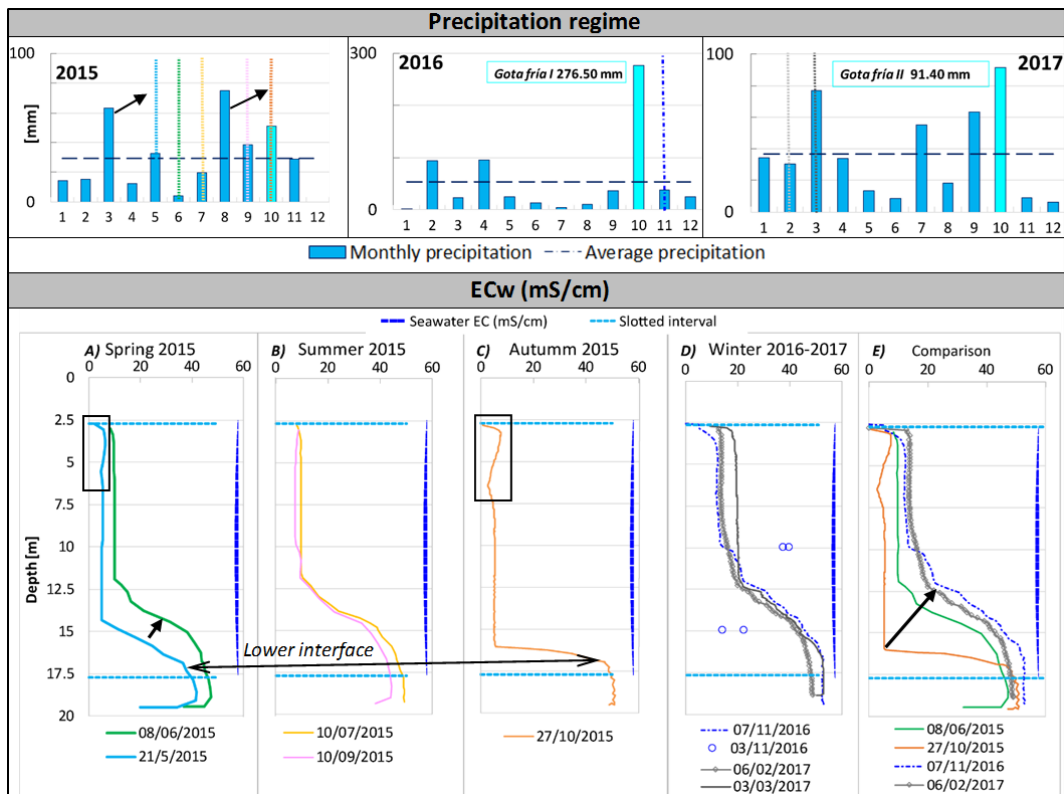


Figure 3-4 Monthly precipitation in mm of the monitored years. The date of salinity profiles acquisition is marked in vertical dotted lines. Salinity profiles performed in PP20 representative of the different seasons (A), B), C) and D)). Salinity profiles after rain events compared with seawater  $EC_w$  (E).

The first profile of the next winter (November, 7th, 2016, Figure 3-4D) was recorded one month after a heavy rainfall event ("Gota fria I": 276.5 mm on October, 12<sup>th</sup>, 2016). After the huge storm that took place, 11 days of subsequent rainfall may have spread the upper saline wedge through the superior part of the profile, as can be seen in the higher values of the salinity profiles (see Figure 3-4D). The anomalous salinity distribution in the upper part was supported by the discrete sampling (Figure 3-4D) performed on November, 2016, that showed higher  $EC_w$  in the upper part of the aquifer. Still,  $EC_w$  values of this profile present a homogeneous increase both in the upper portion of the borehole (reaching 14 mS/cm) and in the position of the salinity jump, which is the highest of all profiles.

This is contradictory to what is observed in the profiles performed in spring and autumn of 2015 (see Figure 3-4A and C), where the increase in salinity is constrained to the top 5 m, and the transition zone between freshwater and salt water is located deeper.

The aquifer tends to salinize during the monitoring interval (2015-2017), which is reflected in the highest salinity measured in the last profile made in winter 2017 (see Figure 3-4E). Overall salinization was also observed by means of CHERT (Palacios et al., 2019) and may reflect that, except for the October, 12<sup>th</sup> 2016 event ("Gota fria I"), rainfall was below

average during these three years. These observations suggest that, although the SWI is quite slow, there is a progressive seawater intrusion into the aquifer. Still, the actual mechanisms beneath this highly variable response of the depth of the interface remain unclear and cannot be addressed relying only on salinity profiles.

### 3.4 DISCUSSION: SWI PATTERNS AND IMPLICATIONS FOR BOREHOLE SALINITY PROFILES

We describe the results of induction logs (IL) and CHERT performed at different time periods (see Table 3-1) to understand the salinity profiles discussed in the previous section. Bulk electrical conductivity ( $EC_b$ ) versus depth is shown for each borehole nest in Figure 3-5. IL yields an average  $EC_b$  within a 1 m sphere around the measurement point, so that they are somewhat smoothed. However, they represent a direct measurement, whereas CHERT profiles result from inversion (Palacios et al., 2019) and should be considered estimated. Still, we take the similarity of IL and CHERT profiles as a validation of CHERT inversion results. IL was not possible at the deepest boreholes (25 m holes of the NX nests, PS25, and PP20) due to interference with the electrode cables. However, the similarity between IL and CHERT profiles allows us to extend direct IL measurements to greater depths, within the CHERT coverage, which also becomes uncertain below 25 m depth, especially at the edges of the considered domain.

Table 3-1 Geophysical acquisitions.

Measurement	Borehole	Date
Induction Logging	N2-15, N2-20	12/05/2015
	N4-15, N4-20	12/05/2015
	MH	13/01/2017
	N3-15, N3-20	12/05/2015
	N1-15, N1-20	11/05/2015
	PP18	31/05/2018
CHERT profile	N2-25	15/07/2015
	N4-25	15/07/2015
	PS-25	15/07/2015
	N3-25	15/07/2015
	N1-25	15/07/2015
	PP20	15/07/2015

The main observation from Figure 3-5 is that  $EC_b$  does not increase monotonically with depth.  $EC_b$  is generally low in the upper portion (above 15 m depth) of inland wells, which suggests that fresh water flows through this zone, as one would expect from the traditional SWI paradigm of Figure 2-1. Still, the zoom of Figure 3-5 displays some additional complexity. First, some wells (N2, N3, MH and PP20) display a somewhat higher  $EC_b$  near the surface, which we attribute to the low EC of the unsaturated zone, but also to saline/brackish water recharge from either storm surge or salty aerosol or both. And,

second, salinity tends to increase a bit with depth within this upper freshwater zone, which we attribute to either past SWI events or to the top salinity fingering its way down.

Beyond the discussion of the shallow portion, the most surprising feature of Figure 3-5 is the reduction of  $EC_b$  at depth (all wells display this reduction below 20 m depth). IL only displays the marked reduction in well MH because all other IL profiles stop at shallower depths. And CHERT interpretation, though attempted, was not possible without the reduction (Palacios, 2020, personal communication). This reduction of  $EC_b$  suggests that freshwater is discharging at depth, which is possible, but unexpected given the relative homogeneity of the aquifer (Figure 3-3). Even more surprising is the PP20 profiles, with four salinity inversions (freshwater below seawater).

We took water samples at several times during the 2015-17 period. Their EC generally confirms the above observations. Shallow (NX-15) samples display small variability in freshwater values (see blue dots in Figure 3-5).  $EC_w$  of deeper samples fluctuates significantly. We attribute this variability to small changes in the actual salinity profile. Within a given nest,  $EC_w$  tends to increase with depth and measurements are consistent with  $EC_b$  profiles, at least in the samples taken from boreholes with short slotted intervals (true piezometers) (green dots in Figure 3-5). In fact, variability is largest in PP20 (see blue dots in Figure 3-5), which is fully slotted and is located closest to the sea. Within the samples in short slotted intervals, variability is largest at the intervals where the salinity gradient of the EC and CHERT profiles is largest (i.e., where small fluctuations in SWI would cause a largest change in the sampled water). The only sampled salinity reversal (fresher water above more saline water) occurred at N1-25. But, except for N2-25, it is the only one where salinity inversion could have been actually sampled.

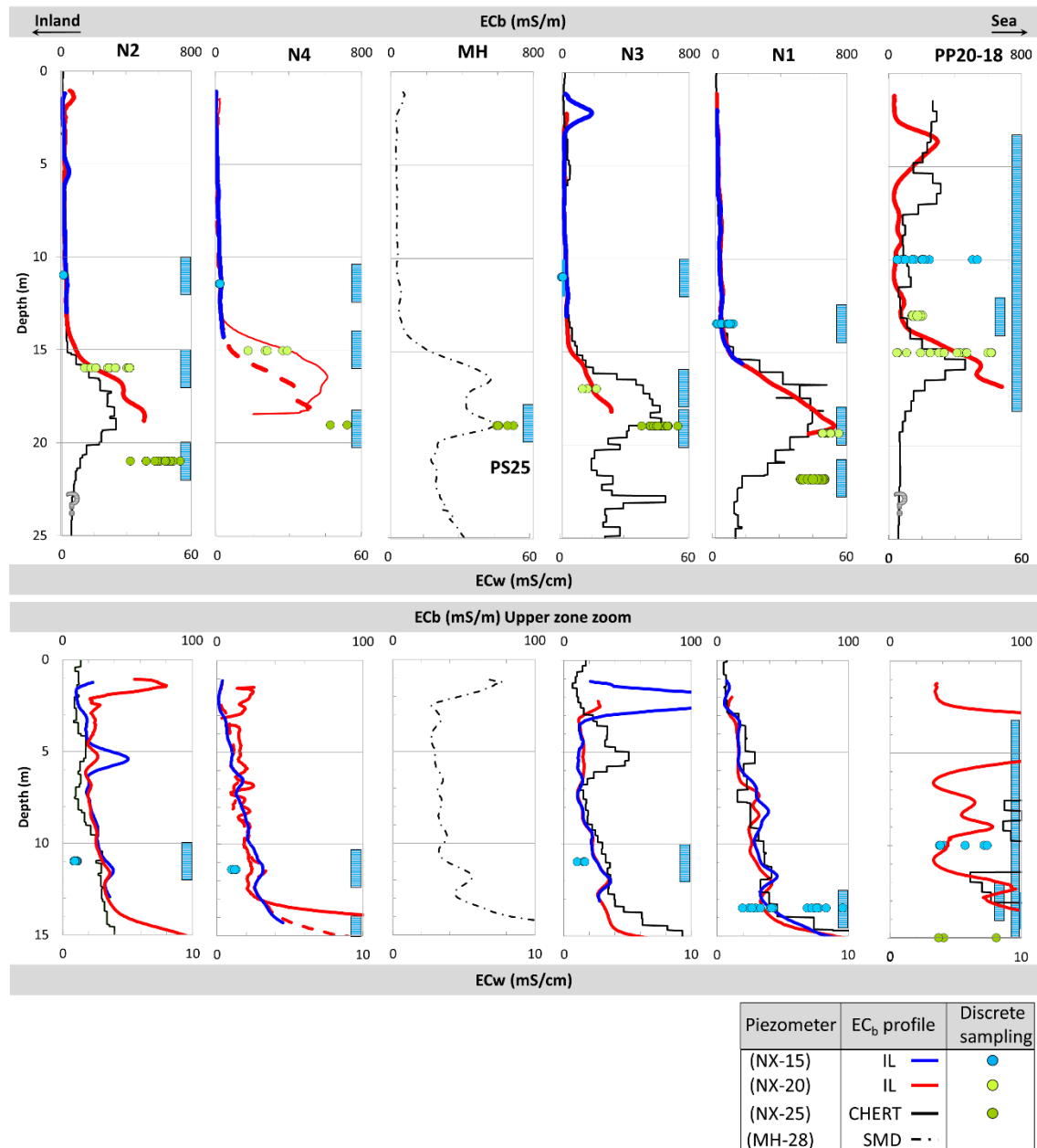


Figure 3-5 Combination of geophysical measurements: Induction logging (electromagnetic method) (mS/m) and CHERT profiles (geo-electric method) and point measurements EC<sub>w</sub> (mS/cm) performed in the different piezometers belonging to each nest. The localization of slotted intervals of each piezometer is marked with blue squares. In PP20 fluid sampling was performed at two different depths. CHERT profile has resolution constraints below 20 m at the edges and is not taken into account for the analysis.

The large fluctuations and the four salinity reversal in the  $EC_b$  profiles of PP20, as well as the reduction of  $EC_b$  at depths in all the boreholes, suggest that SWI is more complex than the model shown in Figure 2-1 and provide the basis for explaining the salinity profiles of this well. Figure 3-6 displays together the CHERT profile, the spectral gamma ray (SGR) log and some of the measured  $EC_w$  profiles. The SGR logs, together with the core descriptions, allow us to identify the relatively minor silt layer of this aquifer. It is clear that the  $EC_b$  maxima occur just above the silt layers located at 7, 12 and 17 m depth. This observation implies the water circulation patterns displayed in Figure 3-6C. Fresh water discharges below each of these three layers and salt water intrudes above. High salinity also covers fresh water discharging at the aquifer top, which we attribute in this well to seawater recharging the aquifer during storm surges. This is indeed consistent with the visual observation of waves flooding the near shore during intense storm events occurring during the studied period, and the correlation of high salinity at the top with high wave height events (Palacios et al., 2019).

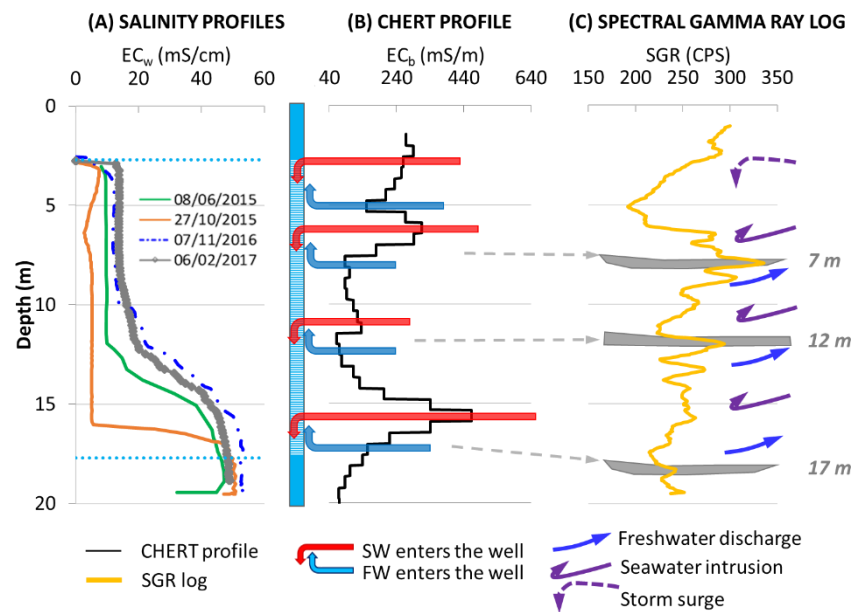


Figure 3-6 Comparison of (A) salinity and (B) CHERT profiles with (C) SGR logs in PP20.

The water circulation patterns described above are confirmed by the  $EC_b$  salinity cross-section beyond PP20 (Figure 3-7). This figure displays freshwater discharging below seawater at, at least, three depths, perhaps four (the inversion associated to the 12 m deep silt layer is not very clear). We interpret the deep saline bodies as two, perhaps three, seawater circulation cells and we attribute the top salinity to seawater entrance caused by storm surges. We observe irregular concentration distributions similar, although at smaller scale, to numerical results of Michael et al. (2016). It is also consistent with sand box experiments of Castro-Alcala (2019) who observed that freshwater discharges under mildly low permeability (K) zones during wet periods.

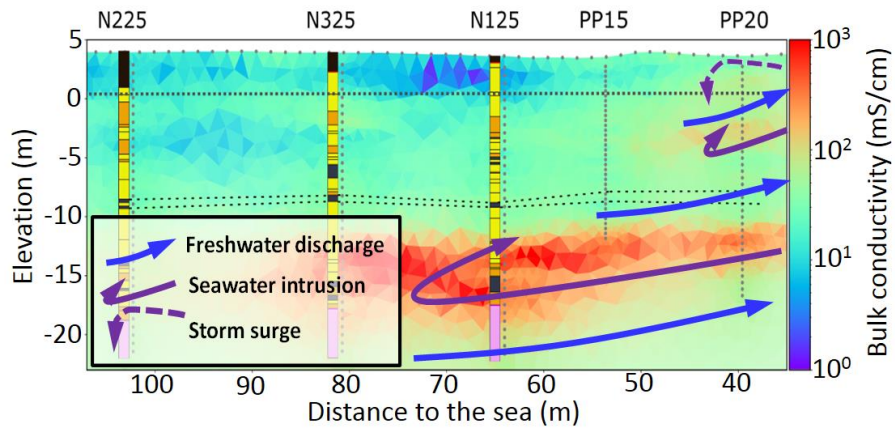


Figure 3-7 Combination of CHERT and surficial ERT (from (Palacios et al., 2019)).

Vertically fluctuations in bulk salinity explain the shape of water salinity profiles in PP20, as also shown in Figure 3-6. High salinity water is denser than freshwater, and is unstable when lying above it. While dense salt water tends to finger down its way across freshwater that flow upwards in the piezometer (Hassanzadeh et al., 2005; Hidalgo et al., 2009; Riaz et al., 2006), within the aquifer, silt layers hinder and slow down this process. In fact, discharging fresh water drags and washes away the downwards trickling salt water. But nothing prevents saline water to sink into freshwater in the piezometer. Figure 3-6b explains the resulting process. Salt water from the most saline regions will tend to sink, thus pulling saline water towards the well. The same occurs at the freshest intervals, due to fresh water floating upwards. The mixture will tend to discharge in the brackish zone above the salty intervals. Actually, mixing may not always occur (i.e., one can envision freshwater floating up in one fraction of the casing section and salt water sinking down in another fraction), which may explain the anomalous inversion measured in some of the  $EC_w$  profiles of Figure 3-4. But we conjecture that mixing may be fostered both by turbulence and by the EC probe while obtaining the profiles.

The implication is that salinity profiles in long-screened piezometers do not reflect aquifer salinity, but the mixture of fresh- and salt- water caused by the multiplicity of discharging fresh water levels.

### 3.5 SUMMARY

Mapping the electrical conductivity of the aquifer, by means of induction logs and cross hole electrical resistivity tomography, implied that water circulation is a lot more complex than expected. Freshwater discharges below silt layers that occur frequently in alluvial deposits aquifers. The top freshwater discharge is also covered near the shore by saline water, which we attribute to seawater recharged during storm surges.

The resulting SWI model is definitely not consistent with the traditional SWI paradigm, where freshwater discharges on top of a seawater wedge. This finding is consistent with numerical results of Michael et al. (2016), who attributed deep freshwater discharges to heterogeneity, or sand box experiments by Castro-Alcala (2019), who attributed them to seasonal freshwater discharge coupled to minor heterogeneities.

An implication of irregular distribution of salinity is that it leads to density variations that generate vertical fluxes inside the boreholes. Dense saline water tends to sink into the well, whereas light fresh water tends to float. The resulting mixing within the well leads to salinity profiles that represent neither the salinity distribution within the aquifer, nor the real position of the seawater intrusion wedge. Instead, salinity profiles in wells represent mixing. This explains the frequent stepwise shape of salinity profiles and the fact that the deepest salinity is typically below seawater.

The fact that these “anomalous” salinity profiles are frequent implies that deep freshwater discharges are equally frequent and that SWI is not so simple as we usually draw it. The traditional paradigm of fresh water discharging above seawater was established for hypothetical homogeneous SWI problems. This paradigm needs to be considered with caution for real aquifers. Even standard heterogeneities, typically neglected a priori, have a proven impact on flow recirculation at largest scale. Since heterogeneity should be considered the rule and anomalous salinity profiles are indeed frequent, direct applicability of the traditional paradigm may have to be considered the exception.

## **Chapter 4.**

Laboratory experiments to characterize radium  
desorption



## 4.1 INTRODUCTION

In the past 15 years, SGD has risen as a hot topic in marine chemistry as a result of the impact of groundwater discharge on coastal environments. This impact can be both positive and negative. SGD represents an important source of nutrients and metals (Lecher and Mackey, 2018), but can also transport excessive loads of nutrients leading to eutrophication (Amato et al., 2020). Thus, the presence of these discharging flows have gained importance and need to be taken into account in coastal aquifers properly. It must be noticed that fresh groundwater input into the oceans and seas worldwide has always been taken into account in the SWI literature as the natural force that avoided salt water migration into aquifers. However, its quantification has received little attention from the hydrogeological community, making the coexistence of SGD and SWI unexplored.

One of the key challenges is to characterize and quantify SGD properly. Within the many methods that exist to characterize it (see (Burnett et al., 2006b) and (Taniguchi et al., 2019) for an updated review), radioactive tracers are good candidates. Indeed, using radioactive tracers such as Radium isotopes, allows tracing processes that occur at different time scales, because of the different half-life of their isotopes ( $^{224}\text{Ra}$ ,  $T_{1/2} = 3.6$  days;  $^{223}\text{Ra}$ ,  $T_{1/2} = 11.4$  days;  $^{228}\text{Ra}$ ,  $T_{1/2} = 5.7$  years; and  $^{226}\text{Ra}$ ,  $T_{1/2} = 1600$  years). Another factor inherent of radioactive elements is the production from parent atoms and radioactive decay. When parent atoms are located closer to a grain surface, alpha recoil can be an important source of radionuclides to the liquid phase. This mechanism, named as a result of the movement that atoms experience after an alpha decay, has been documented as a significant input of radionuclides (Sturchio et al., 2001). Nevertheless, Radium activity in aquifer groundwater (also called subterranean estuary (Moore, 1999)) can vary over many orders of magnitude due to geochemical heterogeneity. This includes the abundance and distribution of parent isotopes in sediments, groundwater salinity, redox conditions, and other factors such as pH, temperature, and organic matter content. The elevated number of variables that can affect its distribution in groundwater, makes characterize radium inland end-member hard.

In addition to this, the concentrations in the dissolved phase can be affected by retardation (R), which causes certain species to move at a different velocity than groundwater. Chemical reactions that cause the precipitation of minerals (Charette and Sholkovitz, 2002), adsorption and cationic exchange with other species (Appelo, 1994) are the mechanisms responsible for this delay. So to quantify, the Ra inland end-member and identify the influencing parameters and conditions of Ra activity, laboratory experiments are needed. The main experimental studies carried out in the field of radioactive tracers focus on obtaining the adsorption parameters of the

materials, in order to subsequently model the transport of radionuclides and contaminants. Specifically, batch and column experiments have been designed to determine the distribution coefficient ( $K_d$ , in L/kg) which is the ratio between the amount of adsorbed and dissolved radium (Serne and Relyea, 1981). The classical procedure relies in adding a known concentration (spike of a pure amount of radionuclide) to a solution and measure its concentration before and after it enters in contact with a variable amount of sediment (see Table 4-1). A broad collection of different values given for different types of materials and salinities can be found in Beck and Cochran (2013).

Table 4-1 - Different experimental conditions to obtain  $K_d$  (units in mL/g if not explicit).

Reference	Ra Spike	Isotope	L/S Ratio	Contact time	Salinity	$K_d$
(Moore and others, 1996)	-	$^{228}\text{Ra}$	33-6000	7-8 h	0	10
(Krest et al., 1999)	-	$^{224}\text{Ra}$ , $^{228}\text{Ra}$ , $^{226}\text{Ra}$ , $^{223}\text{Ra}$		1 h	36	6280
(Meier et al., 1987)	10-5 – 10-11 M	$^{226}\text{Ra}$	9-1.1	-	-	210-32
(Gonneea et al., 2008)	100 dpm	$^{226}\text{Ra}$	0.02-0.75	12 h - 6 months	5, 15, 25	200, 450, 200
(Tachi et al., 2001)	-			20-40 days	1 M KCl 0.1 M NaCl 0	100-10000
(Beck and Cochran, 2013)	100 $\mu\text{L}$ of 50 dpm	$^{224}\text{Ra}$		1-12 h	40 mL seawater	0.33-38.7
(Baraniak et al., 1999)	40 to $2 \cdot 10^3$ Bq			8 weeks	-	3100-3650 mL/g 76-612 62-178
(Beneš and Strejc, 1986)	20 mg	$^{224}\text{Ra}$ spiked		17 h	-	2900 mL/g
(Chen and Kocar, 2018)	3-320 Bq	$^{226}\text{Ra}$		-	10 mM NaCl	2.77-3020000
(Hancock et al., 2006)	-	$^{223}\text{Ra}$		2 h	seawater	0.022-0.041 Bq/m <sup>3</sup>

The problem with the widespread experimental method to calculate  $K_d$ , is that these processes cannot be taken into account or be integrated in a dynamic way if changes in salinity are present. Despite this, the  $K_d$  approach is the most extended due to its ease of implementation. Numerous experiments have been performed to characterize  $K_d$  under different conditions (e.g. different salinities) and different materials (e.g. adsorbents) (see Table 4-1). In this brief recompilation we can already notice the broad range of values obtained. We conjecture that part of the problem may be inadequate tests (basically we need simultaneously adsorbed and in solution concentrations, which is hard).

In Argentina, the materials that compose our experimental site are formed by alluvial deposits resulting from the weathering of the surrounding granitic outcrops (see chapter 2). Granites are formed by minerals that contain  $^{238}\text{U}$  and  $^{232}\text{Th}$  which are continuously producing radium isotopes. They remain adsorbed to grain surfaces under freshwater conditions until a variation in salinity causes their desorption. As a result, they are present in high concentrations in fresh groundwater contained in coastal aquifers, especially, several orders of magnitude greater than in seawater. This difference allows to determine SGD through mass balances calculations if Ra concentrations in open seas (sea end-member) and in the aquifer groundwater (inland end-member) are known or estimated.

So, in this chapter, we propose new tests and a methodology that can be standardized to discretize the importance of absolute salinity vs. flow conditions in Ra desorption. We performed constant salted fluid injections but we also vary the salinity (SWI and SGD simulation) to infer adsorbed Ra from its mobilization. We finally proposed a 0D model as a first step to interpret the column experiments.

## 4.2 EXPERIMENTAL MATERIALS AND METHODS

In order to better understand the behavior of Ra in the Argentina coastal aquifer depending on different conditions, we have performed various laboratory experiments. We selected one of the samples characterized in Chapter 2, representative of the average geochemical parameters measured in the aquifer: low CEC and BET surface area (see Table 4-2).

Sample n1-13 was extracted from the intermediate part of the aquifer (18 m depth), where salinity ranges between 32 and 37 g/L and  $^{224}\text{Ra}$  activities present an average value of  $741.6 \text{ dpm} \cdot 100^{-1}\text{L}$ . The sediments correspond to medium to coarse sands with different proportions of quartz, albite, illite, and microcline.

Table 4-2 - Geochemical parameters of sample n1-13.

Geochemical parameters	
CEC ( $\text{meq} \cdot 100\text{g}^{-1}$ )	2.279
BET ( $\text{m}^2 \cdot \text{g}^{-1}$ )	2.33
$^{224}\text{Ra}$ bulk ( $\text{Bq} \cdot \text{kg}^{-1}$ )	33.3
surface bound $^{224}\text{Ra}$ ( $\text{Bq} \cdot \text{kg}^{-1}$ )	1.61
$^{226}\text{Ra}$ ( $\text{Bq} \cdot \text{kg}^{-1}$ )	14.8
$^{228}\text{Ra}$ ( $\text{Bq} \cdot \text{kg}^{-1}$ )	31.1

Two aliquots of the selected sediment were analyzed to characterize the radioactive signal of the sample. Bulk radium content was measured by gamma-spectrometry (Moore and Arnold, 1996) (see Table 4-2). In 100 g aliquot, surface exchangeable Ra was measured using a special device designed by Cai et al. (2012) coupled to a RaDeCC (Radium delayed coincidence counter) (see Table 4-1). This method measures directly

the activity emitted by the co-precipitated radium in the surface of the grains with an overall accuracy of 5%.

#### 4.2.1 Batch experiment

We selected another aliquot of 100 g from the same sediment type to perform a batch experiment at NaCl saturation (350 g/L) to perform a total exchangeable radium desorption. The sediment was mixed with 2.5 kg of brine and mixed during 30 min. After a period of decantation, water was filtered and rinsed through MnO<sub>2</sub> fibers. After the first wash, sediment was recombined with another volume of Ra-free brine up to 4 more times.

#### 4.2.2 Column experiments

The sediment fraction between 2 mm and 0.63 μm was used to fill 4 methacrylate columns of 25 cm height. The columns were packed with 1.5 kg of sediment and 500 mL of milli-Q water with 25 g/L of NaCl. At the base and at the top of the sediment column, 250 g of glass spheres were placed to avoid outlet clogging and distribute homogeneously the percolated water (Figure 4-1). After column construction, the sediment was left for 22 days, to ensure <sup>224</sup>Ra is in equilibrium with its parent nuclide, <sup>228</sup>Th.

Columns were connected with latex tubing to a peristaltic pump that enabled percolation of a controlled volume of liquid at a constant rate at the top and recovery at the bottom. Water percolations were fixed to a volume of 500 mL, the same as the pore volume (PV) of the column. Each recovered sample was the volume of water contained in the column, so in the practice, sampling consisted in a displacement of column pore volume, and not the classical flow-through column experiment. The porosity of the columns was around 0.47 and transit times ranged from 2 to 4 h, as sediment got compacted because of the consecutive percolations and columns heterogeneities.

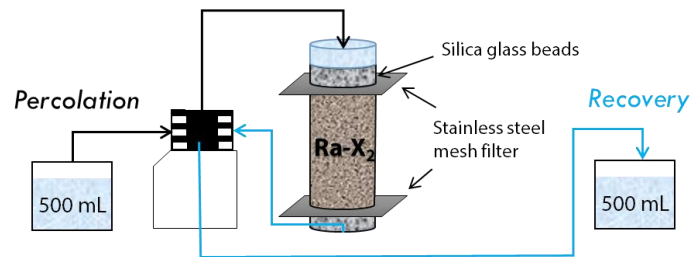


Figure 4-1 Experimental setup.

Sampled waters were later passed through 20 g of MnO<sub>2</sub> fibers to adsorb the radium desorbed from the sediment and analyze them using a RaDeCC.

This experimental setup enables to percolate radium-free water at different salinities and measure the desorbed radium under the following conditions:

1. *Recovering time impact on radium desorption.* We first tested the influence of water sample recovery in radium desorption to ensure the reproducibility of the different columns. After reaching secular equilibrium, the pore volumes of the 4 columns were displaced with another Ra-free 500 mL of milli-Q water at a salinity of 25 g/L. Sample recovery was performed at different times: from consecutive percolation-recovery until a contact time of 3 days in the column (Table 4-3).
2. *Radium desorption at different fixed salinities.* Columns were percolated with different volumes to set-up the salinity from the initial 25 g/L until a fixed value of 0, 5, 10 and 25 salinities (Table 4-3) and measure the desorbed radium.
3. *Radium desorption at consecutive fixed inlet salinities.* We then tested the influence of consecutive percolation of pore volumes at a fixed salinity. We took advantage of the different columns to examine the effect of different salinities on radium desorption (Table 4-3).

Table 4-3 - Experimental conditions.

Column	1. Elapsed time (25 g/L salinity)	2. Different fixed salinities (g/L)	3. Continuous percolations (ix) at fixed inlet salinity (g/L)
C1	3 days	25	2x 30, 4x 60
C2	3 h	0	11x 70, 15x 140
C3	1 h	10	10x 30, 10x 80
C4	0 h	5	4x 40

4. *Radium desorption at variable salinities:* Simulation of a SWI and a SGD event. Finally, we simulated a progressive entrance of seawater and the effect of a submarine groundwater discharge by percolating consecutive water volumes by increasing and decreasing salinities, respectively (see Table 4-4 for more details).

Table 4-4 - Simulation events (SWI and SGD), and the correspondent salinity of each displacing pore volume (PV).

		Salinity (g/L)										
Event	SWI	5	10	15	25	30	35	45	60	80	100	Column C4
	SGD	120	100	80	60	45	30	25	15	10	5	Column C2

### 4.3 INTERPRETATION METHOD

To interpret the tests described in Section 4.2, we need a model that simulates the evolution of Ra concentration within the column, taking into account adsorption and desorption. Column tests are usually interpreted using one-dimensional transport models, including reaction terms (Boluda-Botella et al., 2008); (Nitzsche and Merkel, 1999). In our case, however, the tests were performed by displacing the whole pore volume for sampling, with variable stagnant periods between samplings. This implies that concentration only varies significantly along the column during displacement periods. Therefore, rather than simulating Ra transport, we are concerned with Ra (and salinity) mass balance. An important element in the balance is the simulation of sorption. We discuss sequentially below how we simulate Ra sorption and mass balance.

#### 4.3.1 Radium sorption

Radium mobilization is driven by exchange with cations, notably Na<sup>+</sup> in our experiments and in SWI problems. Therefore, strictly speaking, Ra sorption and desorption should be modeled using cation exchange models. However, preliminary simulations using PHREEQC (Parkhurst and Appelo, 1995) and RETRASO (Saaltink et al., 2004), led to too high Ra concentrations in solution (i.e., insufficient sorption). This probably reflects that widely used cation exchange models may be inadequate. Cation exchange models typically rely on Cation Exchange Capacity (CEC) and selectivity coefficients from data bases, but not on the specific minerals of the sediments. It is well known that sorption of Ra is extremely sensitive to the presence of Fe and Mn oxides (Gonneea et al., 2008). Therefore, surface complexation models may be more appropriate, but these require cation specific selectivity coefficients that are not widely available (but see Chen and Kocar (2018)). Still, a useful conclusion from our preliminary simulations with PHREEQC and RETRASO was that sorbed Ra relates linearly with radium in solution and that the proportionality constant depends on salinity, which reflects that Na concentrations remain unaffected by exchange with Ra. This justifies adopting the traditional adsorption model, widely used in the radium transport literature (Webster et al., 1995) (Michael et al., 2011)):

$$c_s = K_d c \quad (4.1)$$

Where  $c_s$  (mol/kg) is the sorbed Ra concentration and  $c$  (mol/L) is the concentration in solution, so that the distribution coefficient,  $K_d$ , is expressed in L/kg. The partition coefficient,  $K_p$ , which expresses the ratio of Ra mass sorbed to Ra mass in solution, is also frequently used in the Ra literature (Krishnaswami et al., 1982). From its definition, it should be evident that  $K_p = \rho_b K_d / \phi$ , where  $\rho_b$  (kg/L) is the bulk (dry) sediment density and  $\phi$  is

the porosity. Here, we will use retardation,  $R$  (-), which relates the total mass of Ra in a volume of sediment to the mass in solution. Therefore,

$$R = 1 + K_p = 1 + \rho_b K_d / \phi \quad (4.2)$$

The important issue is that any of these parameters has been found to depend heavily on salinity. The most widely used model is that of Webster et al. (1995), which we write as:

$$R = 1 + \frac{B}{S} \quad (4.3)$$

where the coefficient  $S$  is salinity and  $B$  needs to be estimated.

### 4.3.2 Radium mass balance

Ra in the column changes because of production and decay, and during sampling. We treat the problem by assuming that the porous medium consists of a portion where water flows (mobile zone) and a portion where water does not flow (immobile zone). Both zones exchange water by diffusion, with a distribution of rates, which is why this model is termed multi-rate mass transfer (MRMT) model (Haggerty and Gorelick (1995); Silva et al. (2009)). This model is widely used in hydrology to represent both kinetic sorption and access to poorly connected zones. Total porosity ( $\phi_T$ , volume of pores per unit volume of porous medium) is divided in mobile porosity ( $\phi_m$ , volume of pores in the mobile zone per unit volume of porous medium) and a number,  $N_{im}$ , of immobile porosities ( $\phi_{im,j}$ ,  $j = 1, N_{im}$ , volume of pores in the  $j$ -th immobile zone per unit volume of porous medium). Each immobile zone exchanges mass with the mobile zone at a rate  $\alpha_j(c_m - c_{im,j})$ , where the exchange rate coefficient,  $\alpha_j$  (1/day) can be viewed as the inverse of the mean residence time in the  $j$ -th immobile zone for a conservative solute (the residence time for an adsorbing solute would be  $R_{im,j}/\alpha_j$ ).

We perform the mass balance between samplings by assuming that concentrations evolve during the percolation time interval and that sampling is performed at the end. Therefore, mass balance is split into two operations. In between samplings, the mass balance in the mobile zone is:

$$(R_m^{k+1} c_m^{k+1} - R_m^k c_m^k) = \sum_{j=1}^N \frac{\phi_{im,j}}{\phi_m} \alpha_j (c_{im,j}^{k+\theta} - c_m^{k+\theta}) \Delta t + \left( \frac{F_{vm}}{\lambda \phi_m} - R_m^k c_m^k \right) (1 - e^{-\lambda \Delta t}) \quad (4.4)$$

Where subindexes  $m$  and  $im$  stand for mobile and immobile, respectively, and the superindex  $k$  stand for time ( $\Delta t = t^{k+1} - t^k$ , we use the superindex  $k + 1 -$  to express concentrations and retardations at the end of the interval, but just before sampling),  $\theta$  is

a time weighting parameter to ensure stability ( $\theta = 0$  for explicit solution,  $\theta = 1$  for implicit,  $\theta = 0.5$  for time centered),  $\lambda$  is the decay constant ( $\lambda = 0.19$  1/day for  $^{224}\text{Ra}$ ), and  $F_{V_m}$  represents the exchangeable mass of  $^{224}\text{Ra}$  generated by the decay of progeny isotopes, per unit time and unit volume of porous medium. The mass balance in the immobile zone is:

$$(R_{im,j}^{k+1}c_{im,j}^{k+1} - R_{im,j}^k c_{im,j}^k) = \alpha_j (c_m^k - c_{im,j}^k) \Delta t + \left( \frac{F_{V_{im,j}}}{\lambda \phi_{im,j}} - R_{im,j}^k c_{im,j}^k \right) (1 - e^{-\lambda \Delta t}) \quad (4.5)$$

We use these equations to represent the mass balance of salinity. In such case, retardations are equal to 1 and both production and decay are zero. They can also be used in the case all water is assumed mobile by simply setting  $\alpha_j = 0$ .

A mass balance is also required for sampling to express mass in the mobile zone change because some mass exits during sampling, which reads:

$$V_m (R_m^{k+1} c_m^{k+1} - R_m^{k+1-} c_m^{k+1-}) = V_s (c_{im}^k - c_s^{k+1}) \quad (4.6)$$

where  $V_m$  is the volume of mobile water and  $V_s$  is the volume of the sample. If  $V_s$  is smaller than  $V_m$ , the sampled concentration,  $c_s^{k+1}$ , is simply the  $c_m^{k+1-}$ . But, if  $V_s/V_m > 1$ , then the whole mobile porosity is substituted by the inflowing water, and the sample is a mixture of the resident concentration in the mobile zone,  $c_m^{k+1-}$ , and the newly equilibrated concentration,  $c_m^{k+1}$ :

$$\begin{aligned} c_s^{k+1} &= r c_m^{k+1-} + (1 - r) c_m^{k+1} \quad \text{if } r < 1 \\ c_s^{k+1} &= c_m^{k+1-} \quad \text{if } r \geq 1 \end{aligned} \quad (4.7)$$

Where  $r = V_m/V_s$ . Substituting this equation in (3.7) and solving for  $c_m^{k+1}$ , we get

$$c_m^{k+1} = \frac{r(R_m^{k+1-} - 1)c_m^{k+1-} + c_{in}^k}{r(R_m^{k+1} - 1) + 1} \quad (4.8)$$

These equations have been programmed in a spreadsheet, available at <https://h2ogeo.upc.edu/en/investigation-hydrogeology/software>

## 4.4 RESULTS

To evaluate the maximum desorption of radium ( $^{224}\text{Ra}$ ), we performed 5 consecutive batch experiments with a liquid-solid ratio (L/S) of 25 and at NaCl saturation (350 g/L). After the first combination of sediment and brine,  $^{224}\text{Ra}$  activity dropped from 400 dpm/100L until less than 200 dpm/100L. The experiment was repeated three more times until a steady state was reached at the fourth washing around 100 dpm/100L (Figure 4-2).

So the maximum Ra desorption measured in this batch experiment with saturated brine water is 400 dpm/100L for 100g of sediments (see Figure 4-2). The constant value of the following wash revealed the effect of alpha recoil regenerating  $^{224}\text{Ra}$  from  $^{228}\text{Th}$  contained in the crystal lattice.

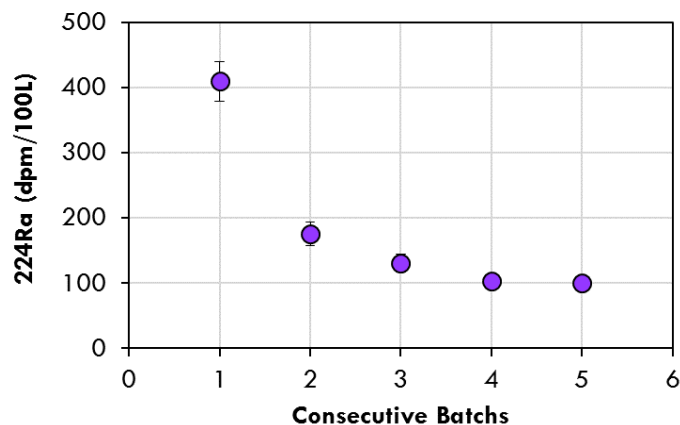


Figure 4-2- Batch experiments performed at halite saturation. Activity of  $^{224}\text{Ra}$  measured after consecutive batch experiments.

#### 4.4.1 Time impact on radium desorption

Column experiments have been performed with L/S ratio comparable with aquifer conditions. As explained in Section 4.2, we built 4 columns filled with the same type of material that we used both in static fluid conditions (such as in classical batch experiments, but with a representative L/S ratio of 0.33) and in dynamic conditions injecting continuously different types of fluids depending of the columns and the objectives.

To assess the variability in radium desorption with time, we displaced the 25 g/L of NaCl water in secular equilibrium inside the column, with another Ra-free volume at the same salinity in all the columns. We let the displacement water for different contact times in each column, and displaced again the contained water: in column C4, we recovered the water just after percolating through the column, and for the rest, we waited 1h (C3), 3 h (C2) and 3 days (C1). Water samples presented almost the same amount of  $^{224}\text{Ra}$  with slight variations within the error (Figure 4-3). This is coherent with the behavior observed by Gonnee et al. (2008), although the liquid-solid ratio (L/S) used here is different (0.33) and no shaking was performed.

Regardless the contact time, the average measured activity for a salinity of 25 g/L in all the columns was  $418 \pm 34.4$  dpm $\cdot$ 100L $^{-1}$ . This first test allowed to establish an equivalence between the columns. Comparing these results with the batch experiment, the total Ra desorpted here (27.6 dpm/100L/100g of sediments) is much less as the salinity is only 25 g/L.

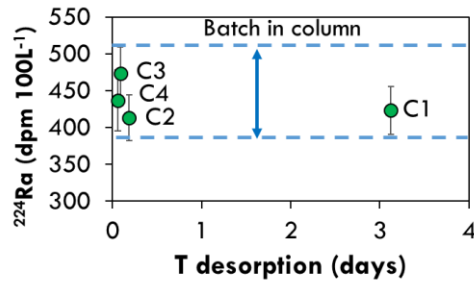


Figure 4-3 - Activity of <sup>224</sup>Ra measured in the four columns after being in contact for different periods of time (C1: 72h, C2: 3h, C3: 1h and C4: 0h since the first injection).

#### 4.4.2 Desorption at different salinities

Taking advantage of the similar behavior of the columns, volumes at different salinities displaced the previous water at 25 g/L until we reach a value of 0, 5, 10 and 25 g/L in C2, C4, C3 and C1 respectively, to compare radium desorption at various salinities. The injected solutions were left inside the columns for 22 days to reach a new secular equilibrium.

The results obtained show a decrease in <sup>224</sup>Ra activity as salinity decreases (Figure 4-4). Radium activity measured in C1 (with again 25 g/L of NaCl) remained the same as in the first set of experiments, confirming the previous desorption values at 25 g/L; for lower salinities, <sup>224</sup>Ra concentration is much lower. Nevertheless, a linear relation between <sup>224</sup>Ra concentration and salinity is highlighted (Figure 4-4) and we can observe that for increments of 5 g/L: from 0 to 5 and 5 to 10, <sup>224</sup>Ra increased more than 50 dpm·100 L<sup>-1</sup>. These reference activities, obtained after secular equilibrium has been reached, for each salinity, will be later compared with "transient" activities measured in the same columns but during continuum water displacements (see Section 4.4.3).

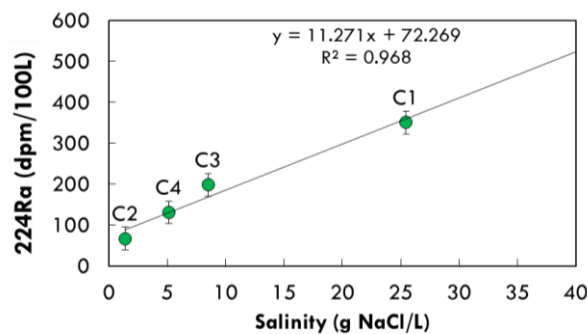


Figure 4-4.- <sup>224</sup>Ra measured activity in the four columns at different salinities in secular equilibrium.

#### 4.4.3 Desorption at consecutive fixed inlet salinities

Once we have characterized the production of Ra at fixed salinities after secular equilibrium was reached (Section 4.4.2), we reproduced sediment washing experiments at constant fluid salinity under representative field L/S ratio. These experiments have two

main objectives: first is to predict the effect of tidal pulses of salt water at a constant salinity entering to the aquifer, and second evaluate the possible change of Ra activity during continuous fluid percolation under the same salinity before reproducing SWI and SGD scenarios (Section 4.4.4).

To do so, different displacement experiments were performed in each column to test the evolution of Ra at constant salinities. Here, we present a subset of the experiments performed for columns C2 and C3. The complete sequence of consecutive water displacements can be found in Appendix A. First, we tested the effect of 10 consecutive water displacements at a salinity of 30 g/L in C3 (Figure 4-5). Results show a similar range with the once-displacement performed at 25 g/L (400-500 dpm·100L<sup>-1</sup>). We later percolate 10 consecutive volumes at 80 g/L salinity, which ended up desorbing more radium, as expected. Results at 80 g/L of salinity showed a sharp decrease at the end of the experiment (Figure 4-5).

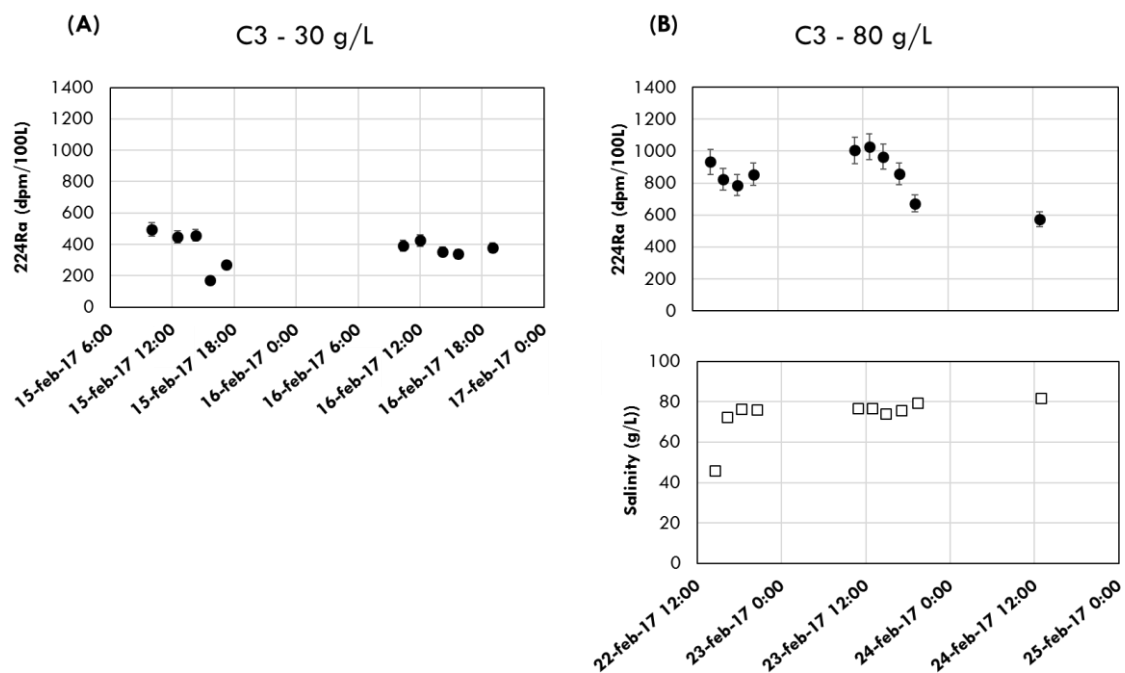


Figure 4-5.- Consecutive percolations performed on C3. A: at 30 g/L and B at 80 g/L. In bottom B part, the outlet water salinity is presented all along the different percolations.

In column C2 (see Figure 4-6), after a consecutive displacement of 11 volumes at 70 g/L, we passed up to 15 pore volumes at 140 g/L. The observed <sup>224</sup>Ra activity at the beginning was low for 140 g/L salinity, but comparable to other measurements for salinities of 70 g/L (see Appendix A). It took 5 percolations to measure an increase in <sup>224</sup>Ra activity, reaching a maximum value of 1300 dpm/100 L<sup>-1</sup>. And actually, this maximum value is reached after a stagnant period of 7 h.

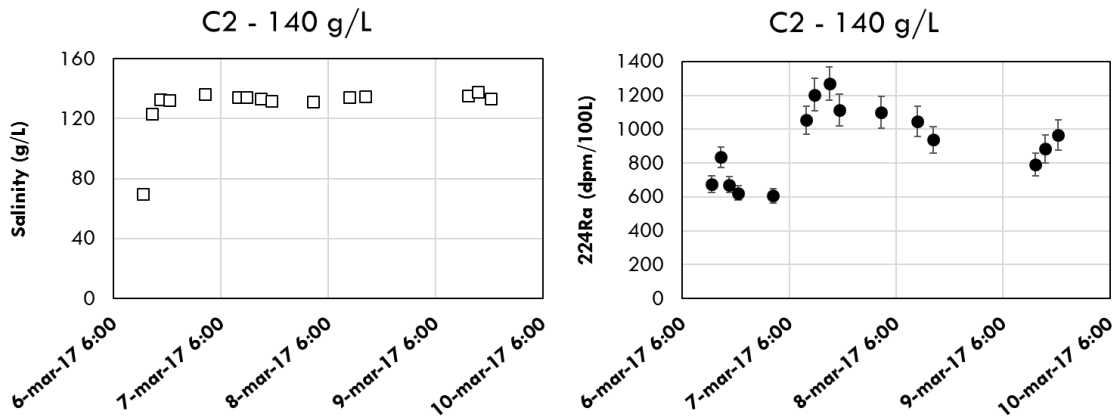


Figure 4-6.- Consecutive percolations performed on C2.

As for other experiments described above, we can see that the outlet fluid salinity reached the inlet one after the 3<sup>rd</sup> percolation. Nevertheless, the outlet fluid salinity is always slightly lower than the inlet one.

For C2 as for C3, we can observe two main trends; first, there is always a delay between the water salinity at the outlet compared to the inlet one, which affects the maximum <sup>224</sup>Ra activity measured; second, the <sup>224</sup>Ra activity is not constant along the experiments. The global trend of <sup>224</sup>Ra activity is to decrease with the different percolated volumes. Nevertheless, this decrease is not linear and we can also observe that we never reach constant <sup>224</sup>Ra activity as during the pure batch leaching experiment (see Figure 4-2) and rather some increases in <sup>224</sup>Ra activity after injection stops.

#### 4.4.4 Desorption at variable salinities

Once the columns were tested against constant salinity washings, we simulated a SWI event in C4 by passing 10 volumes at an increasing salinity from 5 to 100 g/L (see Table 4-4 and Figure 4-7) to test the effect of aquifer salinity gradients.

As expected, Ra activity increased all along the SWI simulation as the fluid salinity increased. However, the outlet salinity is always lower than the inlet one, resembling the mixing with the previous percolated volumes (Figure 4-7A). This difference is higher for high salinity fluid which can also be related to the injection time.

For a salinity around 25 g/L, we again have a similar Ra desorption around 500 dpm/100L as during the previous experiments.

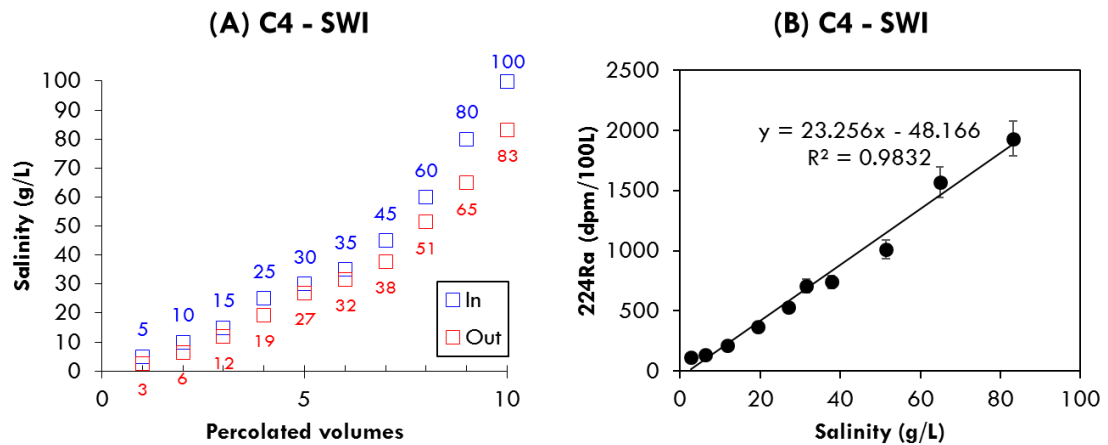


Figure 4-7.- Simulation of a SWI event in column C4. Evolution of inlet and outlet salinity (A) and radium desorption (B).

We took advantage of the previous injected salinity water in C2 at 140 g/L of NaCl to simulate an SGD event by passing 10 pores volumes at a decreasing salinity (Figure 4-8). Salinity decreased in 10 steps from 140 (inlet water initially) to 5 g/L (see Table 4-4). As previously observed,  $^{224}\text{Ra}$  activity desorption was higher for higher salinity injections, as expected. Unlike in the SWI event, the outlet salinity is always higher than the inlet one, due to mixing process between the injected water and the previous one. The decrease in Ra is smoother from the 6<sup>th</sup> volume percolated because changes in salinity are more gradual (the slope is softer).

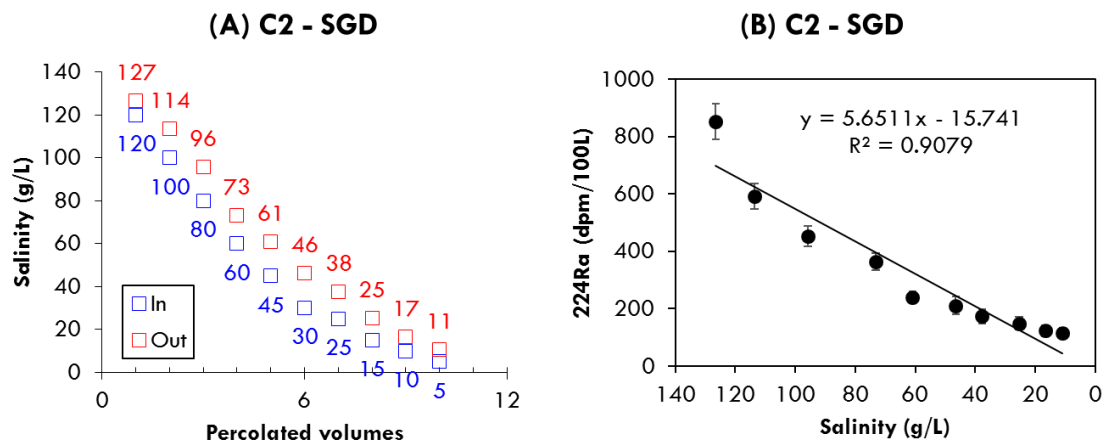


Figure 4-8.- Simulation of an SGD event in column C2. Evolution of inlet and outlet salinity (A) and temporal evolution of  $^{224}\text{Ra}$  activity (B).

## 4.5 DISCUSSION

We have performed a total of 8 column tests passing the same amount of water at various fixed NaCl concentrations, and at increasing or decreasing salinities using sediment recovered from an experimental site affected by both salinization and freshening events (SWI and SGD). We wanted to characterize radium desorption in

coastal aquifers but also understand the mechanisms behind the well-known salinity dependence of radium desorption.

#### **4.5.1 Displacement tests at fixed salinity**

Sequential displacements were made at high salinities to characterize the rate at which exchangeable radium desorbs from sediment grains. However, no top limit was reached, and desorption kept on adding radium to the liquid phase as during the batch experiment, possibly due to the effect of alpha recoil.

During the batch experiment, we measured a maximum Ra desorption of 400 dpm/100L/100g (Figure 4-2) which should be equivalent to 6135 dpm/100L in the L/S column ratio (with 1.5 kg of sediments). During the column experiments, we never reached such a high Ra activity as we have always injected lower salinity fluids.

The shape of the Ra activity evolution was different in the batch experiment, where activity dropped markedly, and in the column displacement tests, where activity fluctuated without a well-defined pattern. These differences can be attributed to two factors. First, as mentioned before, salinity was much lower in the column experiments than the one used in the batch experiment. Therefore, the Ra desorbable at each percolation step is also lower. Second, the L/S is very different. In the batch experiment, the L/S ratio is 25. This means that there are few sorption sites for Ra in the sediment compared to the water volume. In the column experiment, the L/S ratio is 0.33. So at least, 75 percolations are needed to reach the same quantity of sediment washing, with a high salinity fluid. This second constrain of L/S ratio explains why after even more than 10 percolations, Ra is still desorbed in the column experiments. This observation demonstrates that sorption is significant in these sediments even at salinities much greater than seawater.

Nevertheless, one can highlight that the shape of the Ra activity is different in C3 and C2. In C3 column, during the experiment at 30 g/L of salinity, Ra activity is almost constant (light decrease with time) whereas during the experiment at 80 g/L, the Ra activity decreased slightly along the percolation (Figure 4-5). During all the experiments, some percolation breaks happened. Nevertheless, after the percolation breaks no remarkable increase of Ra activity is measured during 30g/L and 80g/L experiment unlike in the C2 column (Figure 4-6). This suggests that almost all the injected fluid is in contact with all the sediments inside the column C3. This hypothesis of almost homogeneous percolation inside C3 column, is validated by the Ra activity measured at 30g/L which is almost the same as for 25g/L, obtained during displacement test experiments with secular equilibrium in the columns (Figure 4-3).

In contrast, the Ra activity measured in C2 column at the beginning of the percolation experiment at 140 g/L of salinity was very low compared to what we could expect. This low Ra activity can be attributed to a localization of the main flux inside the C2 column. Indeed, localization causes the amount of desorbable Ra in contact with the percolated fluid to be lower as only part of the sediment is in contact with the injected fluid. It was this observation what motivated using a MRMT model as described later in Section 4.6. After the first stagnant period, the Ra activity in C2 column increases a lot. We infer that the increase of Ra activity after the stagnant period may be due to diffusion process between the mobile zone and the immobile zone (zone not percolated during the injection steps, and therefore allowed to be enriched in radium). The diffusion mechanism induces a mixing process between the mobile and immobile zone and all the accessible Ra for 140g/L of salinity is desorbed.

So, unlike to what we have concluded from the time impact on radium desorption experiments (Section 4.4.1), the different columns are not equally packed. C3 column looks like homogeneously packed whereas C2 may have preferential path and consequently only part of the sediment will be in contact with the percolated fluid during displacement. As explained in Section 0, we proposed a MRMT numerical approach to take into account these mobile and immobile zones (see Section 4.6).

#### 4.5.2 Displacement tests to simulate SWI and SGD

In column C2, the simulation of the freshening event was performed during 23 h 18 min of effective water displacements (in 4 days) whereas the salinization event in C4 lasted 43 h 37 min (in 6 days).

The salinization of the aquifer (SWI event) was simulated using salinities between 5 and 100, lower than those during freshening (SGD event), between 120 and 5 g/L. Yet, higher activities were measured during the salinization event in C4.

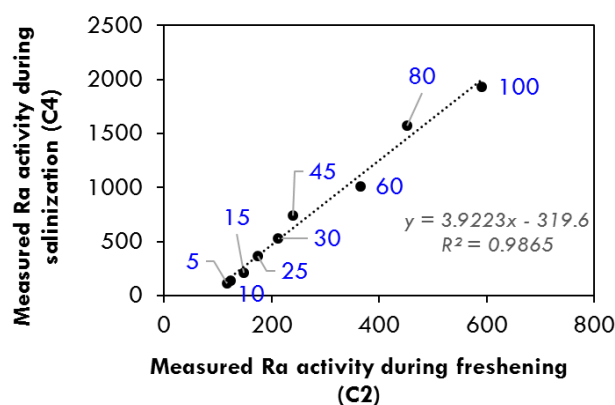


Figure 4-9.- Measured  $^{224}\text{Ra}$  activity during salinization and freshening events. Inlet salinity of the percolating volumes is marked in blue.

The highest Ra value during salinization in C4 (1934 dpm·100L<sup>-1</sup>) at an outlet salinity of 83 g/L doubles the first one measured during freshening in C2 (853 dpm·100L<sup>-1</sup>) at a salinity of 126.3 g/L. On a first glance, this observation is consistent with the view that that Ra accumulates at sorption sites when water is fresh, and desorbs during desalinization. The opposite occurs during freshening, which would explain why Ra activity is far higher during salinization than during freshening. However, another explanation is possible.

As highlighted before, the lower Ra activity measured in C2 column compared to the other columns (C3 and here C4) might be due to preferential flow path inside the column and a large part of immobile zones. Nevertheless, the Ra activity measured in C2 column during the SGD experiment is consistent with the one measured during the continuous fluid percolation at 140g/L before percolation breaks. Even if, here again some stops happened, the Ra activity after the break is not higher than the one before.

Comparing the two SWI and SGD salinity profiles of injected and outlet salinities (Figure 4-7A and Figure 4-8A), we can see that there is more mixing between the injected water and the one injected at time t-1, during the SGD simulation. This indicates that a large amount of the injected water remains in the column at each injection step and consequently, we can confirm that preferential flow paths are developed in column C2 compared to column C4. This localization of the flow can also explain the lower values of <sup>224</sup>Ra activity desorbed as the available sediment phase in contact with the percolated water is much lower with “funneled” preferential flow path. Moreover, the amount of Ra activity is linearly correlated with the salinity whatever the flow distribution inside the column (heterogeneous and localized for C2 column and more homogeneous for C4 column). Actually from Figure 4-9, we can infer that almost 4 more sediment is in contact with the percolated fluid in the C4 column than in C2 column.

Actually, for C4, we can observe in Figure 4-7, a linear relation between the Ra activity in the outlet fluid and the fluid salinity. This linear relation coupled with the absolute values obtained during this SWI simulation indicate that the C4 is mostly homogeneous and the flow percolates in almost all the column. Indeed, if we pick some Ra activity values during the SWI experiment we can see that they are comparable to the ones obtained in batch experiment conditions such as in Figure 4-2 and Figure 4-3 (for example, for a salinity of 35g/L, we measured a Ra activity of 708 ± 53 dpm/100L whereas the equivalent activity using the batch experimental results should be 670 ± 45 dpm/100L).

So, for both freshening and salinization, <sup>224</sup>Ra activities remained behaving as expected (i.e. <sup>224</sup>Ra increased when salinity increased and vice versa). No contradictory increases or decreases with respect to salinity evolution has been observed (as seen in Figure 4-7

and Figure 4-8), meaning that during stable periods of time, where no salinity changes occur (i.e. constant salinity inputs), transport condition and sediment accessibility are key parameters that control  $^{224}\text{Ra}$  activity. When salinity changes, as during SWI and SGD, the evolution of Ra desorption/adsorption looks completely controlled by the amount of NaCl present in the solution and not the transport condition.

## 4.6 MODELING

The analysis of the experimental data highlighted some differences in radium behavior within the columns, and with respect to salinity variations. At first, we attribute them to differences in packing and squeezing caused by the sequential percolations. In order to shed some light on this hypothesis, we simulated the whole sequence of percolations performed in the columns using the 0D model presented in Section 0. As an input for the model, we used some of the sediment parameters presented in Section 4.2 and some others listed in Table 4-5.

Table 4-5 – Input parameters for the model.

Symbol	Parameter (units)	Value
$\phi_T$	Total porosity (-)	0.47
$\rho_s$	Solids density (100 g/m <sup>3</sup> )	26700
$\rho_b$	Bulk density (100 g/m <sup>3</sup> )	14151
$F_{Vex}$	Radium source (dpm/100L/d)	136700
$F_{Vm}$	Ra source in mobile zone (dpm/m <sup>3</sup> /d)	29085

Bulk density  $\rho_b$  was calculated as  $\rho_s(1 - \phi)$  and  $F_{Vex} = \rho_b f_{m_{ex}}$  in dpm/m<sup>3</sup>. Being  $f_{m_{ex}} = 1.61 \text{ Bq/kg} = 31 \cdot 6 = 9.6 \text{ dpm/100 g}$  the exchangeable radium measured from the sediment ( $^{224}\text{Ra}$ ). We considered the source of in each zone as  $F_{Vm} = F_{Vex} \phi_m f$ , that will depend on the fraction of porosity we are considering ( $\phi_m$ ,  $\phi_{im1}$  or  $\phi_{im2}$ ).

Once computed,  $F_{Vex}$  was fixed for all the columns as it is assumed to be dependent on the medium (Th concentration). The coefficient  $B$ , which depends on the cation exchange capacity of the sediment, was calculated by the model. Two immobile zones were assumed. Their mass exchange rate coefficients were adjusted to fit salinity but constrained so that,  $\alpha_{im2}$  was considered as  $\alpha_{im1}/10$ .

We run the model taking into account the whole record of percolations to adjust the measured and computed values of salinity and considering the same listed parameters for all the columns. The values obtained by the model were adjusted minimizing the total objective function, which is the sum of squared errors.

The results obtained (Figure 4-10) show a good agreement for the salinity evolution, and a fair approximation of the overall trend, but not the fluctuations, of radium activity for the water displacements performed at constant salinity.

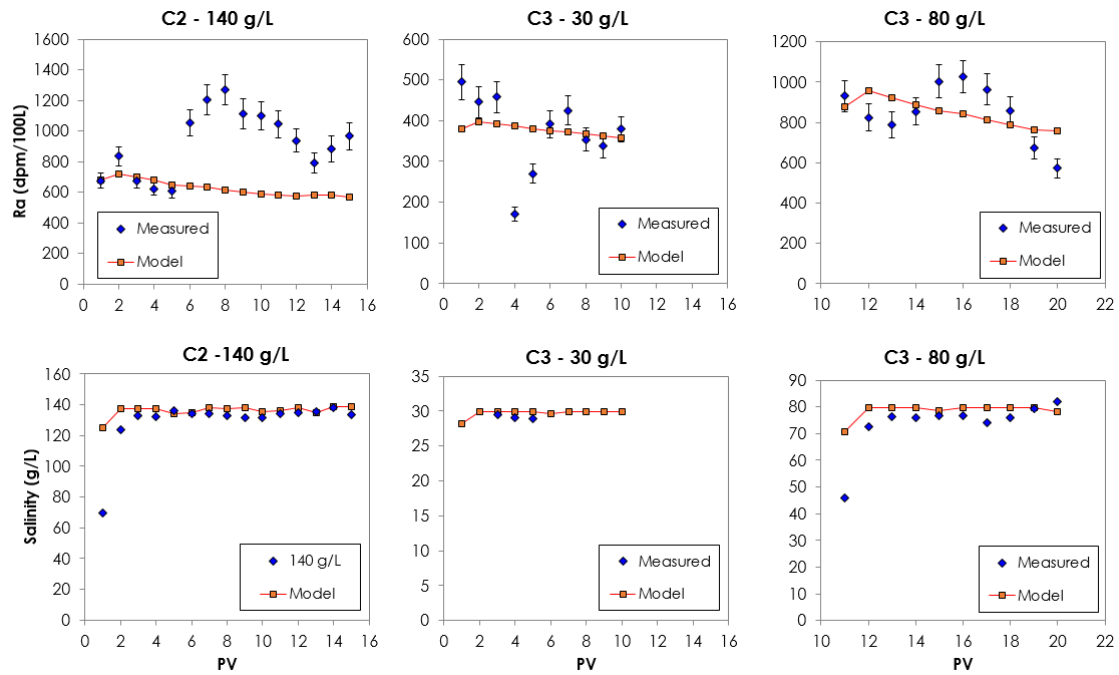


Figure 4-10.- Results of the simulations for fixed inlet salinity simulations.

However, the best results were obtained for the case of the simulations of SWI and SGD events (Figure 4-11). The rest of the parameters obtained by the model are listed in

Table 4-6 and confirm the presence of the immobile zones of column C2, which also constraints the mismatch for the first salinity value calculated by the model.

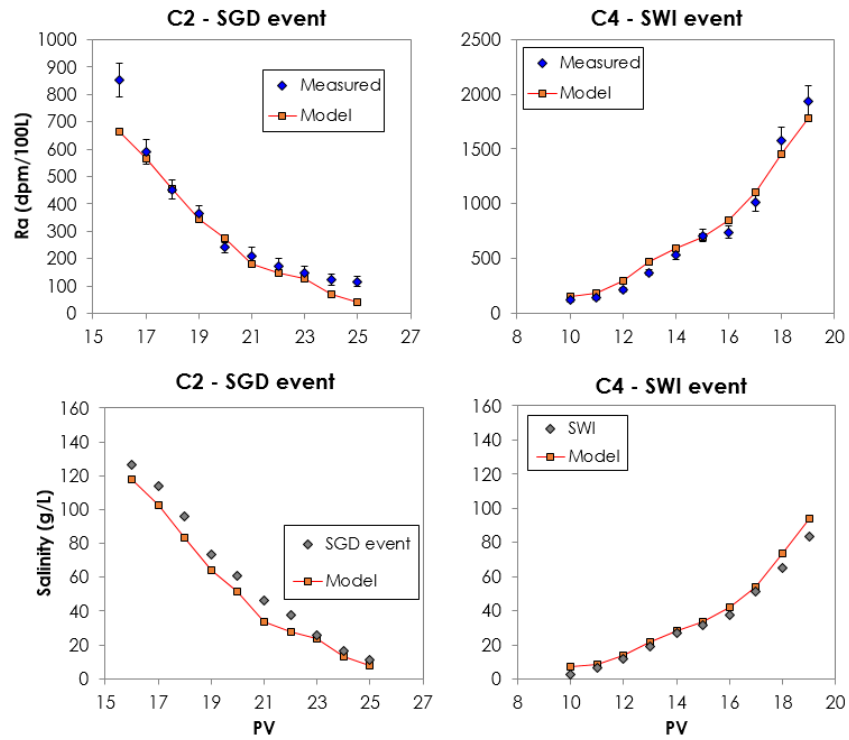


Figure 4-11- Results of the simulations performed for the SWI and SGD events.

Table 4-6 –Calibrated parameters.

Parameters	C2	C3	C4
$\phi_m$	0.09	0.10	0.17
$\phi_{im1}$	0.47	0.37	0.39
$\phi_{im2}$	0.01	0.10	0.01
$\alpha_{im1}$	0.51	0.09	0.03
$\alpha_{im2}$	0.05	0.01	0.00
$F_{vex}$	30000	30000	30000
$F_{Vm}$	2700	2905.93	5222.96
$F_{vim1}$	14100.00	11194.07	11577.04
$F_{vim2}$	300.00	3000.00	300.00
$B$	27265.34	11814.70	7319.79
$S_{initial}$	25.00	25.00	25.36
$Ra_{initial}$	422.00	480.22	400.00

The estimations for parameter B, which is related to CEC, should be the same because we are dealing with the same sediment, however, we obtained different B values for each column. We attribute this to different columns packing that affected water – sediment interaction. The preliminary simulations show higher B parameter for column C2, that also display the higher computed  $\alpha_{im1}$  values. This is consistent with the results observed in the experiment, where salinity evolution was delayed with respect to the inlet salinity (see Figure 4-6 and Figure 4-10). The previous percolations performed in C2, at 0 salinity, maintained Ra adsorbed to grain surfaces, due to the higher retardation.

Later, several volumes were passed through at a salinity of 70 g/L, which made radium remain adsorbed maybe because of the presence of a considerable fraction of immobile water. The high retardation values obtained (around 200 for the highest salinities) imply that almost all the radium remains sorbed to the surface and are the cause for the low values measured and obtained by the model for the continuous percolations performed at 140 g/L.

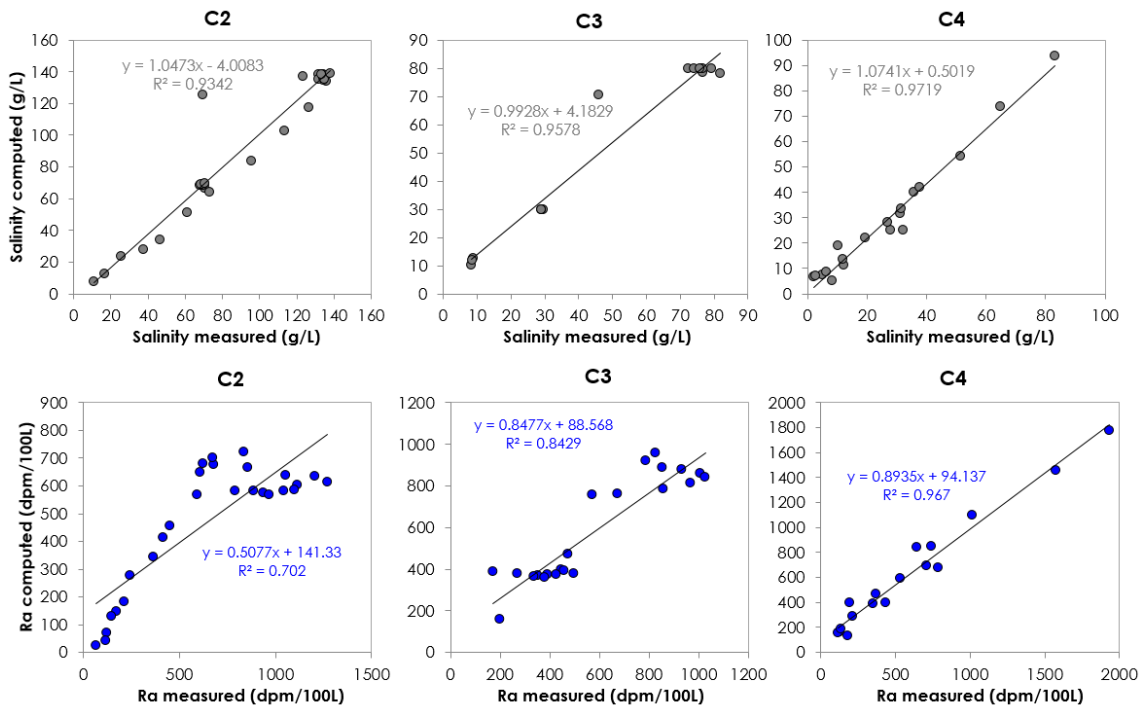


Figure 4-12- Measured and computed <sup>224</sup>Ra activity and salinity for the whole set of percolations.

We observed a similar behavior in C3, the activity is too high because it was previously exposed to a 10 g/L salinity. There is a lot of radium generated that remain adsorbed to grain surfaces. We conjecture that this is the reason why we later observe that huge increase when salinity increases.

The model does not represent well the radium activity fluctuations observed in tests performed at constant salinity. This may reflect that we may not have reached equilibrium during sequential percolations. It may also reflect that the high pressure gradients required to displace the water may have changed the porosity structure of the sediments.

## 4.7 SUMMARY

This work has led to a number of findings regarding Ra in sediments, testing methodologies and interpretation.

Regarding the salinity dependence of Ra activity in groundwater, significant desorption occurs when salinity increases, but sorption remains significant even at large salinities. Since most of the Radium is unaffected by washing, it should be close to secular equilibrium. Discrepancies from secular equilibrium should be attributed to heterogeneity or mixing during sampling, but not to sorption.

Regarding tests performance, consistent results were obtained both with the traditional batch experiments and with the proposed freshening and salinization experiments. Constant salinity tests yielded fluctuations that are hard to explain. We have observed that heterogeneous flux through preferential flow paths occurs in the samples. Variations in these flow paths may explain the observed fluctuations. Such variations may also occur during the freshening and salinization experiments, but the changes in sorption are so dominant that overcome the impact of changes in porosity structure.

The model reproduces both salinity evolution in all experiments and Ra activity evolution during freshening and salinization experiments, but not the constant salinity displacement experiments. Results are generally consistent with expectations, but the radium adsorption coefficient  $B$  is much larger than expected. The high dependence of distribution coefficients on mineralogy may explain the broad range of retardation coefficients used in the literature.

Our analysis of radium evolution during water displacements in these sediments aquifer yields some hints to better constrain radium inland end-member, notably the importance of mineralogy to understand sorption and heterogeneity to understand departures from secular equilibrium. Still, further work is needed. This includes:

- It would be desirable to simulate flow continuously and, possibly the evolution of porosity structure.
- Our experiments were performed at constant pH, to test its effect, and be able to compare the results with field observations, it would be necessary to modify pH injecting acid and simulate biogeochemical reactions that take place in the aquifer.
- Further insight on alpha recoil is needed to properly link Th measurements with  $^{228}\text{Ra}$  production. In this context, it would be desirable to perform the tests with uniform grain sizes, which would also facilitate uniform packing.

- We conjecture that alpha recoil may vary with salinity because the presence of cation on the grain surface may screen recoil. To test this conjecture, specific batch tests and column tests would have to be performed.
- The above would allow including alpha recoil in our model, thus reducing interpretation uncertainties.

## **Chapter 5.**

### Conclusions and Future Steps



The original goal of this thesis was to understand the interaction of SWI and SGD by a detailed study of a field site and specific laboratory experiments to characterize the desorption of Ra during aquifer salinization.

As part of the field work, we developed a heavily instrumented site at Argentona, where we generated and analyzed data on the four pillars of hydrogeology (Geology, Geophysics, Hydraulics, and Hydrochemistry and Isotopes). The design of the instrumentation was based on the traditional paradigm of SWI, which assumes freshwater discharging over salt water and both bodies separated by a mixing zone.

We found that the traditional paradigm is not valid at Argentona. The alluvial quaternary aquifer, that was expected to be roughly homogeneous, presented minor silt layers which ended controlling freshwater discharge, which takes place not just above a seawater wedge, but also below. In fact, three levels of discharge below saline water could be identified with the help of geophysics (both induction logs and cross-hole ERT).

This finding was supported by tidal response tests, which show that aquifer head fluctuations in response to sea level fluctuations were driven by mechanical loading, rather than driven by hydraulic connection to the sea. Mechanical response should be expected in confined, but not in unconfined aquifers. As with salinity fluctuations, we attribute mechanical response to the semiconfining effect of the silt layers.

The fact that Argentona does not follow the traditional SWI paradigm could be considered exceptional. However, the multiple freshwater discharge levels help us explain the anomalous salinity profiles usually observed in fully slotted coastal wells. That these profiles are unreliable was well known. However, the fact that they often display stepwise shapes and that salinity at depth rarely equals that of seawater remained unexplained. The presence of multiple freshwater discharge levels can explain these anomalies as a result of mixing within the well: freshwater floats towards the surface while mixing with sinking seawater. Beyond the anecdotic nature of this explanation, we find relevant that the frequency of these anomalies suggests that the Argentona observations may not be exceptional, and that the traditional SWI paradigm needs to be revised for unconfined porous aquifers, that could seem to be homogeneous.

Hydrochemistry was also surprising in that chemical activity was unusually high. We believe that this activity reflects not only the rich interaction between fresh and salt water discussed above, but also probably the episodic presence of wastewater that bypasses the treatment plant during flood events. As a result, site hydrochemistry is complex, which has hindered the study of radium as a tracer of continental water discharge. Radium concentrations correlate with salinity, as expected. But other factors (pH, sediment composition and grain size) also affect radium distribution within the aquifer.

This complexity has been confirmed by laboratory experiments on the salinity dependence of Ra sorption. We performed both traditional batch experiments in which Ra activity is measured after mixing sediments with saline water (typically varying salinity) and newly developed column tests where resident pore water was displaced with Ra free water, so that the measured activity at the outlet comes from Ra desorption.

We performed sequences of displacement both with constant salinity or with increasing (salinization experiments) or decreasing (freshening experiments) salinity. Constant salinity tests yielded fluctuations that are hard to explain. We have observed that heterogeneous flux through preferential flow paths occur in the columns. Variations in these flow paths may explain the observed fluctuations. Such variations may also occur during the freshening and salinization experiments, but the changes in sorption are so dominant that overcome the impact of changes in porosity structure. Therefore, we conclude that salinization and freshening experiments are robust and should be considered a good characterization test.

Regarding the behavior of Ra in the aquifer, it was known that Ra desorbs when salinity increases, what we have found is that sorption remains significant even at large salinities. An implication is that Ra should be close to secular equilibrium (most of it is unaffected by washing). Therefore, discrepancies from secular equilibrium should be attributed to heterogeneity or mixing during sampling, but not to sorption. Our analysis of radium evolution during water displacements in these sediments aquifer yields some hints to better constrain radium inland end-member in quantifying SGD. In particular, it makes it clear that thorough geochemical characterization is essential to understand Ra sorption. Also, heterogeneity is necessary to understand departures from secular equilibrium.

In this and other regards, the detailed geochemical and isotopic sediment characterization described in Chapter 2 is a contribution from this thesis that will hopefully be exploited in the future.

## References

- Abarca, E., 2006. Seawater intrusion in complex geological environments. Universitat Politècnica de Catalunya.
- Abarca, E., Carrera, J., Sánchez-Vila, X., Dentz, M., 2007. Anisotropic dispersive Henry problem. *Advances in Water Resources*, 30(4): 913-926.
- Abdul Nassir, S., Loke, M., Lee, C., Nawawi, M., 2000. Salt-water intrusion mapping by geoelectrical imaging surveys. *Geophysical Prospecting*, 48(4): 647-661.
- Alcolea, A., Castro, E., Barbieri, M., Carrera, J., Bea, S., 2007. Inverse modeling of coastal aquifers using tidal response and hydraulic tests. *Ground Water*, 45(6): 711-22. DOI:10.1111/j.1745-6584.2007.00356.x
- Amato, D.W., Whittier, R.B., Dulai, H., Smith, C.M., 2020. Algal bioassays detect modeled loading of wastewater-derived nitrogen in coastal waters of O'AHU, HAWAII. *Marine Pollution Bulletin*, 150: 110668.
- Andersen, M.S., Nyvang, V., Jakobsen, R., Postma, D., 2005. Geochemical processes and solute transport at the seawater/freshwater interface of a sandy aquifer. *Geochimica et Cosmochimica Acta*, 69(16): 3979-3994. DOI:<https://doi.org/10.1016/j.gca.2005.03.017>
- Appelo, C., 1994. Cation and proton exchange, pH variations, and carbonate reactions in a freshening aquifer. *Water Resources Research*, 30(10): 2793-2805.
- Archie, G.E., others, 1942. The electrical resistivity log as an aid in determining some reservoir characteristics. *Transactions of the AIME*, 146(01): 54-62.
- Bakker, M., Miller, A.D., Morgan, L.K., Werner, A.D., 2017. Evaluation of analytic solutions for steady interface flow where the aquifer extends below the sea. *Journal of hydrology*, 551: 660-664.
- Bampalouka, E.L.E.N.I., 2016. Sea water Intrusion with a focus on the geological heterogeneity.
- Baraniak, L., Thieme, M., Bernhard, G., Nitsche, H., 1999. Sorption behavior of radium on sandy and clayey sediments of the upper Saxon Elbe river valley. *Journal of radioanalytical and nuclear chemistry*, 241(3): 511-517.
- Bear, J., Cheng, A.H.-D., Sorek, S., Ouazar, D., Herrera, I., 1999. *Seawater intrusion in coastal aquifers: concepts, methods and practices*, 14. Springer Science & Business Media.
- Beck, A.J., Cochran, M.A., 2013. Controls on solid-solution partitioning of radium in saturated marine sands. *Marine Chemistry*, 156: 38-48.
- Bech, J., 1977. El factor climático en la edafogénesis del Maresme (Barcelona). *Revista de geografía*, 11(1): 37-61.
- Beneš, P., Strejč, P., 1986. Interaction of radium with freshwater sediments and their mineral components: IV. Waste water and riverbed sediments. *Journal of radioanalytical and nuclear chemistry*, 99(2): 407-422.
- Boluda-Botella, N., Gomis-Yagües, V., Ruiz-Beviá, F., 2008. Influence of transport parameters and chemical properties of the sediment in experiments to measure reactive transport in seawater intrusion. *Journal of hydrology*, 357(1-2): 29-41.
- Buckley, D.K., Hinsby, K., Manzano, M., 2001. Application of geophysical borehole logging techniques to examine coastal aquifer palaeohydrogeology. *Geological Society, London, Special Publications*, 189(1): 251-270.
- Burnett, W.C. et al., 2006a. Quantifying submarine groundwater discharge in the coastal zone via multiple methods. *Sci Total Environ*, 367(2-3): 498-543. DOI:10.1016/j.scitotenv.2006.05.009
- Burnett, W.C. et al., 2006b. Quantifying submarine groundwater discharge in the coastal zone via multiple methods. *Science of the total Environment*, 367(2): 498-543.
- Cai, P., Shi, X., Moore, W.S., Dai, M., 2012. Measurement of <sup>224</sup>Ra: <sup>228</sup>Th disequilibrium in coastal sediments using a delayed coincidence counter. *Marine Chemistry*, 138: 1-6.
- Carr, P., Van Der Kamp, G., 1969. Determining aquifer characteristics by the tidal method. *Water Resources Research*, 5(5): 1023-1031.
- Carrera, J., Hidalgo, J.J., Sooten, L.J., Vázquez-Suñé, E., 2009. Computational and conceptual issues in the calibration of seawater intrusion models. *Hydrogeology Journal*, 18(1): 131-145. DOI:10.1007/s10040-009-0524-1
- Cerdà-Domènech, M., Rodellas, V., Folch, A., Garcia-Orellana, J., 2017. Constraining the temporal variations of Ra isotopes and Rn in the groundwater end-member: Implications for derived SGD estimates. *Science of The Total Environment*, 595: 849-857. DOI:<https://doi.org/10.1016/j.scitotenv.2017.03.005>
- Clark, I.D., Fritz, P., 2013. *Environmental isotopes in hydrogeology*. CRC press.
- Custodio, E., 1995. The impact of vertical water flow in boreholes on monitoring operations. *Hydrogéologie (Orléans)*(3): 3-12.

- Custodio, E., Bruggeman, G.A., 1987. Groundwater problems in coastal areas. Publication of the IHP Working Group on Changes in the Salt-fresh Water Balance in Deltas, Estuaries and Coastal Zones due to Structural Works and Groundwater Exploitation.
- Custodio, E., Llamas, M., 2001. *Hidrología Subterránea*, Ediciones Omega. Barcelona, España.
- Charette, M.A., Buesseler, K.O., Andrews, J.E., 2001. Utility of radium isotopes for evaluating the input and transport of groundwater-derived nitrogen to a Cape Cod estuary. *Limnology and Oceanography*, 46(2): 465-470.
- Charette, M.A., Sholkovitz, E.R., 2002. Oxidative precipitation of groundwater-derived ferrous iron in the subterranean estuary of a coastal bay. *Geophysical Research Letters*, 29(10): 85-1-85-4. DOI:10.1029/2001gl014512
- Chen, M.A., Kocar, B.D., 2018. Radium sorption to iron (hydr) oxides, pyrite, and montmorillonite: implications for mobility. *Environmental science & technology*, 52(7): 4023-4030.
- Chidichimo, F., De Biase, M., Rizzo, E., Masi, S., Straface, S., 2015. Hydrodynamic parameters estimation from self-potential data in a controlled full scale site. *Journal of Hydrology*, 522: 572-581. DOI:10.1016/j.jhydrol.2015.01.022
- Cho, H.-M. et al., 2018. Radium tracing nutrient inputs through submarine groundwater discharge in the global ocean. *Scientific reports*, 8(1): 2439.
- Church, P.E., Granato, G.E., 1996. Bias in ground-water data caused by well-bore flow in long-screen wells. *Groundwater*, 34(2): 262-273.
- Church, T.M., 1996. An underground route for the water cycle. *Nature*, 380(6575): 579-580.
- Dausman, A., Langevin, C.D., 2005. Movement of the saltwater interface in the surficial aquifer system in response to hydrologic stresses and water-management practices, Broward County, Florida. US Department of the Interior, US Geological Survey.
- Dearing, J., 1994. Environmental magnetic susceptibility. Using the Bartington MS2 system. Kenilworth, Chi Publ.
- Díaz, J., Maldonado, A., 1990. Transgressive sand bodies on the Maresme continental shelf, western Mediterranean Sea. *Marine Geology*, 91(1-2): 53-72.
- Domenico, P.A., Schwartz, F.W., 1998. *Physical and chemical hydrogeology*, 506. Wiley New York.
- Du Commun, J., 1828. ART. XXV.--On the Cause of Fresh Water Springs. *Fountains, &c. American Journal of Science and Arts (1820-1879)*, 14(1): 174.
- Falgàs, E. et al., 2011a. Integrating hydrogeological and geophysical methods for the characterization of a deltaic aquifer system. *Surveys in Geophysics*, 32(6): 857-873.
- Falgàs, E. et al., 2011b. Integrating Hydrogeological and Geophysical Methods for the Characterization of a Deltaic Aquifer System. *Surveys in Geophysics*, 32(6): 857-873. DOI:10.1007/s10712-011-9126-2
- Falgàs, E., Ledo, J., Marcuello, A., Queralt, P., 2009. Monitoring freshwater-seawater interface dynamics with audiomagnetotelluric data. *Near Surface Geophysics*, 7(5-6): 391-400.
- Ferris, J.G., 1952. Cyclic fluctuations of water level as a basis for determining aquifer transmissibility, US Geological Survey.
- Fetter, C.W., 2018. *Applied hydrogeology*. Waveland Press.
- Folch, A. et al., 2020. Combining Fiber Optic (FO-DTS), CHERT and time-lapse formation electrical conductivity to characterize and monitor a coastal aquifer.
- Folk, R.L., Ward, W.C., 1957. Brazos River bar [Texas]; a study in the significance of grain size parameters. *Journal of Sedimentary Research*, 27(1): 3-26.
- Galofre, A., 1969. Estudio hidrogeológico de la cuenca de la Riera d'Argentona. *Tesi de llicenciatura*, Universitat de Barcelona. Laboratori de Geomorfologia i Geotectònica.
- Gámez, D. et al., 2009. Onshore-offshore correlation of the Llobregat deltaic system, Spain: Development of deltaic geometries under different relative sea-level and growth fault influences. *Sedimentary Geology*, 217(1-4): 65-84. DOI:10.1016/j.sedgeo.2009.03.007
- García-Solsona, E. et al., 2010. An assessment of karstic submarine groundwater and associated nutrient discharge to a Mediterranean coastal area (Balearic Islands, Spain) using radium isotopes. *Biogeochemistry*, 97(2-3): 211-229.
- Gat, J.R., Gonfiantini, R., 1981. Stable isotope hydrology. Deuterium and oxygen-18 in the water cycle.
- Ghyben, B.W., 1888. Nota in verband met de voorgenomen putboring nabij, Amsterdam. The Hague, 21.
- Goebel, M., Knight, R., Halkjær, M., 2019. Mapping saltwater intrusion with an airborne electromagnetic method in the offshore coastal environment, Monterey Bay, California. *Journal of Hydrology: Regional Studies*, 23: 100602.
- Goldman, M., Kafri, U., 2006. Hydrogeophysical applications in coastal aquifers, *Applied hydrogeophysics*. Springer, pp. 233-254.
- Gonneea, M.E., Morris, P.J., Dulaiova, H., Charette, M.A., 2008. New perspectives on radium behavior within a subterranean estuary. *Marine Chemistry*, 109(3-4): 250-267.

- Goyetche, T. et al., 2020. Hydraulic and mechanical characterization of tide-induced head fluctuations in coastal aquifers – Part 2: Application to a real case. In preparation.
- Guarracino, L., Carrera, J., Vázquez-Suñé, E., 2012. Analytical study of hydraulic and mechanical effects on tide-induced head fluctuation in a coastal aquifer system that extends under the sea. *Journal of Hydrology*, 450-451: 150-158. DOI:10.1016/j.jhydrol.2012.05.015
- Guo, H., Jiao, J.J., Li, H., 2010a. Groundwater response to tidal fluctuation in a two-zone aquifer. *Journal of Hydrology*, 381(3-4): 364-371. DOI:10.1016/j.jhydrol.2009.12.009
- Guo, Q., Li, H., Boufadel, M.C., Sharifi, Y., 2010b. Hydrodynamics in a gravel beach and its impact on the Exxon Valdez oil. *Journal of Geophysical Research*, 115(C12). DOI:10.1029/2010jc006169
- Haggerty, R., Gorelick, S.M., 1995. Multiple-rate mass transfer for modeling diffusion and surface reactions in media with pore-scale heterogeneity. *Water Resources Research*, 31(10): 2383-2400.
- Hancock, G.J., Webster, I.T., Stieglitz, T.C., 2006. Horizontal mixing of Great Barrier Reef waters: Offshore diffusivity determined from radium isotope distribution. *Journal of Geophysical Research*, 111(C12). DOI:10.1029/2006jc003608
- Hassanzadeh, H., Pooladi-Darvish, M., Keith, D., 2005. Modelling of convective mixing in CO<sub>2</sub> storage. *Journal of Canadian Petroleum Technology*, 44(10).
- Hazen, A., 1911. Discussion of "Dams on soil foundations": *Transactions American Society of Civil Engineers*, v. 73.
- Heinz, J., Kleinedam, S., Teutsch, G., Aigner, T., 2003. Heterogeneity patterns of Quaternary glaciofluvial gravel bodies (SW-Germany): application to hydrogeology. *Sedimentary geology*, 158(1-2): 1-23.
- Herzberg, A., 1901. Die wasserversorgung einiger Nordseebäder. *J. Gasbeleucht. Wasserversorg.*, 44: 842-844.
- Hesselbo, S.P., 1996. Spectral gamma-ray logs in relation to clay mineralogy and sequence stratigraphy, Cenozoic of the Atlantic margin, offshore New Jersey  
In *Proceedings of the Ocean Drilling Program: Scientific Results (Vol. 150, p. 411)*. The Program.
- Hidalgo, J.J., Carrera, J., Medina, A., 2009. Role of salt sources in density-dependent flow. *Water resources research*, 45(5).
- Huber, E., Huggenberger, P., 2016. Subsurface flow mixing in coarse, braided river deposits. *Hydrology & Earth System Sciences*, 20(5).
- IGME, 1976. I.G.M.E. (1976). Mapa Geológico de España 1:50.000. Hoja nº 393. Mataró, Segunda Serie, Primera Edición. Instituto geológico y minero de España.
- Jiao, J., Post, V., 2019. *Coastal Hydrogeology*. Cambridge University Press.
- Jiao, J.J., Tang, Z., 1999. An analytical solution of groundwater response to tidal fluctuation in a leaky confined aquifer. *Water Resources Research*, 35(3): 747-751.
- Kirkegaard, C., Sonnenborg, T.O., Auken, E., Jørgensen, F., 2011. Salinity distribution in heterogeneous coastal aquifers mapped by airborne electromagnetics. *Vadose Zone Journal*, 10(1): 125-135.
- Kiro, Y., Weinstein, Y., Starinsky, A., Yechieli, Y., 2015. Application of radon and radium isotopes to groundwater flow dynamics: An example from the Dead Sea. *Chemical Geology*, 411: 155-171. DOI:10.1016/j.chemgeo.2015.06.014
- Knee, K., Paytan, A., 2011. 4.08 submarine groundwater discharge: a source of nutrients, metals, and pollutants to the Coastal Ocean. *Treatise Estuar. Coast. Sci.*, 4: 205-234.
- Knudby, C., Carrera, J., 2006. On the use of apparent hydraulic diffusivity as an indicator of connectivity. *Journal of Hydrology*, 329(3-4): 377-389.
- Krest, J.M., Harvey, J.W., 2003. Using natural distributions of short-lived radium isotopes to quantify groundwater discharge and recharge. *Limnology and Oceanography*, 48(1): 290-298.
- Krest, J.M., Moore, W.S., others, 1999. 226Ra and 228Ra in the mixing zones of the Mississippi and Atchafalaya Rivers: indicators of groundwater input. *Marine Chemistry*, 64(3): 129-152.
- Krishnaswami, S., Graustein, W.C., Turekian, K.K., Dowd, J.F., 1982. Radium, thorium and radioactive lead isotopes in groundwaters: Application to the in situ determination of adsorption-desorption rate constants and retardation factors. *Water Resources Research*, 18(6): 1663-1675.
- Lamontagne, S., Taylor, A.R., Herpich, D., Hancock, G.J., 2015. Submarine groundwater discharge from the South Australian Limestone Coast region estimated using radium and salinity. *J Environ Radioact*, 140: 30-41. DOI:10.1016/j.jenvrad.2014.10.013
- Lebbe, L., 1983. Mathematical model of the evolution of the fresh water lens under the dunes and beach with semi-diurnal tides, 8th salt water intrusion meeting, Bari. *Geologia Applicata e Idrogeologia*, pp. 211-226.
- Lebbe, L., 1999. Parameter identification in fresh-saltwater flow based on borehole resistivities and freshwater head data. *Advances in water resources*, 22(8): 791-806.

- Lecher, A.L., Mackey, K.R., 2018. Synthesizing the effects of submarine groundwater discharge on marine biota. *Hydrology*, 5(4): 60.
- Levanon, E., Shalev, E., Yeichieli, Y., Gvirtzman, H., 2016. Fluctuations of fresh-saline water interface and of water table induced by sea tides in unconfined aquifers. *Advances in Water Resources*, 96: 34-42. DOI:10.1016/j.advwatres.2016.06.013
- Li, H., Jiao, J.J., 2001. Tide-induced groundwater fluctuation in a coastal leaky confined aquifer system extending under the sea. *Water Resources Research*, 37(5): 1165-1171.
- Li, H., Jiao, J.J., 2002. Analytical solutions of tidal groundwater flow in coastal two-aquifer system. *Advances in Water Resources*, 25(4): 417-426.
- Li, X., Hu, B.X., Burnett, W.C., Santos, I.R., Chanton, J.P., 2009. Submarine ground water discharge driven by tidal pumping in a heterogeneous aquifer. *Ground Water*, 47(4): 558-68. DOI:10.1111/j.1745-6584.2009.00563.x
- Liu, S., Gao, M., Tang, Z., Hou, G., Guo, F., 2016. Responses of submarine groundwater to silty-sand coast reclamation: A case study in south of Laizhou Bay, China. *Estuarine, Coastal and Shelf Science*, 181: 51-60. DOI:10.1016/j.ecss.2016.08.012
- Liu, Y., Jiao, J.J., Liang, W., Kuang, X., 2017. Hydrogeochemical characteristics in coastal groundwater mixing zone. *Applied Geochemistry*, 85: 49-60. DOI:10.1016/j.apgeochem.2017.09.002
- Maier, U. et al., 2005. Characterization of Quaternary gravel aquifers and their implementation in hydrogeological models. *IAHS PUBLICATION*, 297: 159.
- Maliva, R.G., Clayton, E.A., Missimer, T.M., 2009. Application of advanced borehole geophysical logging to managed aquifer recharge investigations. *Hydrogeology Journal*, 17(6): 1547-1556. DOI:10.1007/s10040-009-0437-z
- Meier, H., Zimmerhackl, E., Zeitler, G., Menge, P., Hecker, W., 1987. Influence of liquid/solid ratios in radionuclide migration studies. *Journal of radioanalytical and nuclear chemistry*, 109(1): 139-151.
- Michael, Post, V.E.A., Wilson, A.M., Werner, A.D., 2017. *Science, society, and the coastal groundwater squeeze*. Wiley Online Library, pp. 2610-2617.
- Michael, H.A., Charette, M.A., Harvey, C.F., 2011. Patterns and variability of groundwater flow and radium activity at the coast: a case study from Waquoit Bay, Massachusetts. *Marine Chemistry*, 127(1): 100-114.
- Michael, H.A. et al., 2016. Geologic influence on groundwater salinity drives large seawater circulation through the continental shelf. *Geophysical Research Letters*, 43(20): 10,782-10,791.
- Moore, W.S., 1976. Sampling <sup>228</sup>Ra in the deep ocean, *Deep Sea Research and Oceanographic Abstracts*. Elsevier, pp. 647-651.
- Moore, W.S., 1996. Using the radium quartet for evaluating groundwater input and water exchange in salt marshes. *Geochimica et Cosmochimica Acta*, 60(23): 4645-4652.
- Moore, W.S., 1999. The subterranean estuary: a reaction zone of ground water and sea water. *Marine Chemistry*, 65(1): 111-125.
- Moore, W.S., Arnold, R., 1996. Measurement of <sup>223</sup>Ra and <sup>224</sup>Ra in coastal waters using a delayed coincidence counter. *Journal of Geophysical Research: Oceans*, 101(C1): 1321-1329.
- Moore, W.S., others, 1996. Using the radium quartet for evaluating groundwater input and water exchange in salt marshes. *Geochimica et Cosmochimica Acta*, 60(23): 4645-4652.
- Neal, C. et al., 1992. Stable hydrogen and oxygen isotope studies of rainfall and streamwaters for two contrasting holm oak areas of Catalonia, northeastern Spain. *Journal of Hydrology*, 140(1): 163-178. DOI:[https://doi.org/10.1016/0022-1694\(92\)90239-R](https://doi.org/10.1016/0022-1694(92)90239-R)
- Nguyen, F. et al., 2009. Characterization of seawater intrusion using 2D electrical imaging. *Near Surface Geophysics*, 7(5-6): 377-390.
- Nitzsche, O., Merkel, B., 1999. Reactive transport modeling of uranium <sup>238</sup> and radium <sup>226</sup> in groundwater of the Königstein uranium mine, Germany. *Hydrogeology Journal*, 7(5): 423-430.
- Ozler, M.H., 2003. Hydrochemistry and salt-water intrusion in the Van aquifer, east Turkey. *Environmental Geology*, 43(7): 759-775.
- Paine, J.G., 2003. Determining salinization extent, identifying salinity sources, and estimating chloride mass using surface, borehole, and airborne electromagnetic induction methods. *Water Resources Research*, 39(3).
- Palacios, A. et al., 2019. Time-lapse cross-hole electrical resistivity tomography (CHERT) for monitoring seawater intrusion dynamics in a Mediterranean aquifer. *Hydrology and Earth System Sciences*.
- Parkhurst, D., Appelo, C., 1995. PREEQC—A Computer Program for Speciation, Reaction Path, Advective-Transport, and Inverse Geochemical Calculations US Department of the Interior Lakewood, Colorado.

- Plummer, L., 1975. Mixing of sea water with calcium carbonate ground water. *Geological Society of America Memoir*, 142: 219-236.
- Pool, M., Carrera, J., 2011. A correction factor to account for mixing in Ghyben-Herzberg and critical pumping rate approximations of seawater intrusion in coastal aquifers. *Water Resources Research*, 47(5).
- Post, V.E.A., Werner, A.D., 2017. Coastal aquifers: Scientific advances in the face of global environmental challenges. *Journal of Hydrology*, 551: 1-3. DOI:10.1016/j.jhydrol.2017.04.046
- Riaz, A., Hesse, M., Tchelepi, H., Orr, F., 2006. Onset of convection in a gravitationally unstable diffusive boundary layer in porous media. *Journal of Fluid Mechanics*, 548: 87-111.
- Rider, M., 1990. Gamma-ray log shape used as a facies indicator: critical analysis of an oversimplified methodology. *Geological Society, London, Special Publications*, 48(1): 27-37.
- Rodellas i Vila, V.i., Garcia Orellana, J., Masqué Barri, P., 2015. Evaluating submarine groundwater discharge to the mediterranean sea by using radium isotopes.
- Rodellas, V.i., Garcia-Orellana, J., Masqué, P., Font-Muñoz, J.S., 2015. The influence of sediment sources on radium-derived estimates of Submarine Groundwater Discharge. *Marine Chemistry*, 171: 107-117.
- Rodellas, V.i. et al., 2017. Using the radium quartet to quantify submarine groundwater discharge and porewater exchange. *Geochimica et Cosmochimica Acta*, 196: 58-73.
- Rovere, A., Stocchi, P., Vacchi, M., 2016. Eustatic and Relative Sea Level Changes. *Current Climate Change Reports*, 2(4): 221-231. DOI:10.1007/s40641-016-0045-7
- Rufi-Salís, M. et al., 2019. Influence of land use changes on submarine groundwater discharge. *Environmental Research Communications*, 1(3): 031005.
- Russak, A., Sivan, O., 2010. Hydrogeochemical tool to identify salinization or freshening of coastal aquifers determined from combined field work, experiments, and modeling. *Environmental science & technology*, 44(11): 4096-4102.
- Saaltink, M.W., Batlle, F., Ayora, C., Carrera, J., Olivella, S., 2004. RETRASO, a code for modeling reactive transport in saturated and unsaturated porous media. *Geologica acta*, 2(3): 0235-251.
- Sanford, W.E., Konikow, L.F., 1989. Simulation of calcite dissolution and porosity changes in saltwater mixing zones in coastal aquifers. *Water Resources Research*, 25(4): 655-667. DOI:10.1029/WR025i004p00655
- Santucci, L., Carol, E., Kruse, E., 2017a. Quaternary marine incursions as indicated by hydrogeochemical evidence in the semi-confined aquifer of the littoral of the Río de la Plata, Argentina. *Quaternary Research*, 88(1): 160-167.
- Santucci, L., Carol, E., Kruse, E., 2017b. Quaternary marine incursions as indicated by hydrogeochemical evidence in the semi-confined aquifer of the littoral of the Río de la Plata, Argentina. *Quaternary Research*, 88(01): 160-167. DOI:10.1017/qua.2017.35
- Schlumberger, 2009. *Log Interpretation Charts—2009 Edition*. Schlumberger, Sugar Land.
- Serne, R., Relyea, J., 1981. The status of radionuclide sorption-desorption studies performed by the WRIT program. *The Technology of High-Level Nuclear Waste Disposal*, 1: 203-254.
- Serra, O., 2008. *Well logging handbook*. Editions Technip.
- Shalev, E. et al., 2009. Biased monitoring of fresh water-salt water mixing zone in coastal aquifers. *Groundwater*, 47(1): 49-56.
- Shepherd, R.G., 1989. Correlations of permeability and grain size. *Groundwater*, 27(5): 633-638.
- Sherif, M.I. et al., 2018. Geological and hydrogeochemical controls on radium isotopes in groundwater of the Sinai Peninsula, Egypt. *Sci Total Environ*, 613-614: 877-885. DOI:10.1016/j.scitotenv.2017.09.129
- Silva, O. et al., 2009. A general real-time formulation for multi-rate mass transfer problems. *Hydrology and Earth System Sciences*, 13(8): 1399-1411.
- Slooten, L.J., Carrera, J., Castro, E., Fernandez-Garcia, D., 2010. A sensitivity analysis of tide-induced head fluctuations in coastal aquifers. *Journal of Hydrology*, 393(3-4): 370-380. DOI:10.1016/j.jhydrol.2010.08.032
- Smith, C.G., Swarzenski, P.W., Dimova, N.T., Zhang, J., 2012. Natural Radium and Radon Tracers to Quantify Water Exchange and Movement in Reservoirs. 345-365. DOI:10.1007/978-3-642-10637-8\_18
- Stanjek, H., Künkel, D., 2018. CEC determination with Cu-triethylenetetramine: recommendations for improving reproducibility and accuracy. *Clay Minerals*, 51(01): 1-17. DOI:10.1180/claymin.2016.051.1.01
- Stumm, F., Como, M., 2017a. Delineation of Salt Water Intrusion through Use of Electromagnetic-Induction Logging: A Case Study in Southern Manhattan Island, New York. *Water*, 9(9): 631.

- Stumm, F., Como, M.D., 2017b. Delineation of Salt Water Intrusion through Use of Electromagnetic-Induction Logging: A Case Study in Southern Manhattan Island, New York. *Water*, 9(9): 631.
- Sturchio, N., Banner, J.L., Binz, C., Heraty, L., Musgrove, M., 2001. Radium geochemistry of ground waters in Paleozoic carbonate aquifers, midcontinent, USA. *Applied Geochemistry*, 16(1): 109-122.
- Tachi, Y., Shibutani, T., Sato, H., Yui, M., 2001. Experimental and modeling studies on sorption and diffusion of radium in bentonite. *Journal of contaminant hydrology*, 47(2): 171-186.
- Tamez-Meléndez, C., Hernández-Antonio, A., Gaona-Zanella, P.C., Ornelas-Soto, N., Mahlknecht, J., 2016. Isotope signatures and hydrochemistry as tools in assessing groundwater occurrence and dynamics in a coastal arid aquifer. *Environmental Earth Sciences*, 75(9). DOI:10.1007/s12665-016-5617-2
- Taniguchi, M. et al., 2019. Submarine Groundwater Discharge: Updates on Its Measurement Techniques, Geophysical Drivers, Magnitudes, and Effects. *Frontiers in Environmental Science*, 7(141). DOI:10.3389/fenvs.2019.00141
- Tellam, J.H., Lloyd, J., Walters, M., 1986. The morphology of a saline groundwater body: its investigation, description and possible explanation. *Journal of Hydrology*, 83(1-2): 1-21.
- Tessler, Z. et al., 2015. Profiling risk and sustainability in coastal deltas of the world. *Science*, 349(6248): 638-643.
- Vallejos, A., Sola, F., Pulido-Bosch, A., 2015. Processes Influencing Groundwater Level and the Freshwater-Saltwater Interface in a Coastal Aquifer. *Water Resources Management*, 29(3): 679-697.
- Webster, I.T., Hancock, G.J., Murray, A.S., 1995. Modelling the effect of salinity on radium desorption from sediments. *Geochimica et Cosmochimica Acta*, 59(12): 2469-2476.
- Werner, A.D. et al., 2013. Seawater intrusion processes, investigation and management: Recent advances and future challenges. *Advances in Water Resources*, 51: 3-26. DOI:10.1016/j.advwatres.2012.03.004
- Werner, A.D. et al., 2012. Vulnerability indicators of sea water intrusion. *Groundwater*, 50(1): 48-58.
- Xue, Y., Wu, J., Ye, S., Zhang, Y., 2000. Hydrogeological and hydrogeochemical studies for salt water intrusion on the south coast of Laizhou Bay, China. *Ground water*, 38(1): 38-45.
- Yechieli, Y., Shalev, E., Wollman, S., Kiro, Y., Kafri, U., 2010. Response of the Mediterranean and Dead Sea coastal aquifers to sea level variations. *Water Resources Research*, 46(12). DOI:10.1029/2009wr008708
- Younger, P.L., 1996. Submarine groundwater discharge. *Nature*, 382(6587): 121-122.
- Zhang, X. et al., 2017. Hydrogeochemical characterization and groundwater quality assessment in intruded coastal brine aquifers (Laizhou Bay, China). *Environ Sci Pollut Res Int*, 24(26): 21073-21090. DOI:10.1007/s11356-017-9641-x

# APPENDIX A

Column	Sampling time	Elapsed time	Salinity in (g/L)	Salinity out (g/L)	224Ra (dpm/100L)	Error 224Ra (dpm/100L)
2	1-12-16 12:45	0.13	25	-	413.2	30.73
2	22-12-16 14:05	21.06	0	1.4	66.58	8.27
2	22-12-16 16:05	0.08	30	-	-	-
2	22-2-17 13:52	61.91	70	69.55	-	-
2	22-2-17 15:29	0.07	70	70.42	-	-
2	22-2-17 17:27	0.08	70	70.23	-	-
2	22-2-17 18:33	0.05	70	70.16	-	-
2	22-2-17 20:28	0.08	70	69.8	-	-
2	23-2-17 10:39	0.59	70	70.27	-	-
2	23-2-17 14:13	0.15	70	69.72	-	-
2	23-2-17 18:01	0.16	70	69.55	-	-
2	23-2-17 23:33	0.23	70	68.08	-	-
2	24-2-17 3:05	0.15	70	68.57	-	-
2	24-2-17 4:01	0.04	70	70.32	-	-
2	6-3-17 12:31	10.35	140	69.55	675.70	47.39
2	6-3-17 14:39	0.09	140	123.44	834.43	60.50
2	6-3-17 16:30	0.08	140	133.07	672.13	47.66
2	6-3-17 18:28	0.08	140	132.14	623.38	43.96
2	7-3-17 2:22	0.33	140	136.19	607.89	42.82
2	7-3-17 9:50	0.31	140	134.42	1052.83	83.54
2	7-3-17 11:43	0.08	140	134.32	1204.53	96.26
2	7-3-17 15:01	0.14	140	133.17	1270.25	97.79
2	7-3-17 17:15	0.09	140	131.83	1113.04	95.66
2	8-3-17 2:39	0.39	140	131.52	1100.19	93.81
2	8-3-17 10:50	0.34	140	134.42	1045.18	90.33
2	8-3-17 14:21	0.15	140	134.73	937.76	77.38
2	9-3-17 13:18	0.96	140	135.15	790.55	67.46
2	9-3-17 15:33	0.09	140	137.97	884.16	82.91
2	9-3-17 18:26	0.12	140	133.38	967.21	89.10
2	3-4-17 22:14	25.16	120	126.59	852.96	62.63
2	4-4-17 1:05	0.12	100	113.66	590.82	44.44
2	4-4-17 15:20	0.59	80	95.80	452.01	35.07
2	4-4-17 18:26	0.13	60	73.20	364.83	29.77
2	5-4-17 10:00	0.65	45	60.91	240.18	20.27
2	5-4-17 12:00	0.08	30	46.45	211.30	30.26
2	5-4-17 14:00	0.08	25	37.75	174.10	25.48
2	6-4-17 14:17	1.01	15	25.38	148.39	21.92
2	6-4-17 16:17	0.08	10	16.70	123.00	18.73
2	6-4-17 18:17	0.08	5	10.85	116.86	17.62
3	1-12-16 11:58	0.05	25	0.00	473.66	35.13
3	5-12-16 18:20	4.27	10	9.04	0.00	0.00
3	5-12-16 20:00	0.07	10	8.24	0.00	0.00
3	22-12-16 11:15	16.64	10	8.50	197.77	17.30
3	22-12-16 15:30	0.18	0	46.50	0.00	0.00
3	15-2-17 10:00	54.77	30	0.00	495.14	43.07
3	15-2-17 12:30	0.10	30	0.00	445.55	38.88
3	15-2-17 14:15	0.07	30	29.50	457.55	37.47
3	15-2-17 15:40	0.06	30	29.04	169.91	16.93
3	15-2-17 17:15	0.07	30	28.93	269.97	23.38
3	16-2-17 10:20	0.71	30	0.00	391.63	33.40
3	16-2-17 12:00	0.07	30	0.00	425.34	36.57
3	16-2-17 14:10	0.09	30	0.00	353.43	28.43
3	16-2-17 15:40	0.06	30	0.00	337.65	29.10
3	16-2-17 19:00	0.14	30	0.00	378.79	30.04
3	22-2-17 14:29	5.81	80	45.95	931.97	77.02
3	22-2-17 16:17	0.07	80	72.48	824.20	67.39
3	22-2-17 18:15	0.08	80	76.33	786.88	65.72

Column	Sampling time	Elapsed time	Salinity in (g/L)	Salinity out (g/L)	224Ra (dpm/100L)	Error 224Ra (dpm/100L)
3	22-2-17 20:32	0.10	80	76.12	854.53	68.73
3	23-2-17 10:51	0.60	80	76.67	1004.67	81.60
3	23-2-17 12:53	0.08	80	76.70	1026.21	80.96
3	23-2-17 14:52	0.08	80	74.19	964.91	78.95
3	23-2-17 17:06	0.09	80	75.92	858.23	67.63
3	23-2-17 19:20	0.09	80	79.36	672.56	54.31
3	24-2-17 12:54	0.73	80	81.88	572.43	47.58
4	2-12-16 10:57	0.06	25	32.25	436.91	41.25
4	2-12-16 13:10	0.09	25	28.00	346.89	34.54
4	5-12-16 13:35	3.02	5	12.35	0.00	0.00
4	5-12-16 15:15	0.07	5	8.34	0.00	0.00
4	22-12-16 11:25	16.84	5	5.13	130.73	12.70
4	19-1-17 12:10	28.03	40	31.15	782.97	58.70
4	19-1-17 14:50	0.11	40	35.61	645.57	47.34
4	19-1-17 18:20	0.15	10	10.14	190.37	18.99
4	19-1-17 20:35	0.09	5	2.02	181.70	22.61
4	22-2-17 16:03	33.81	5	2.64	116.55	13.45
4	22-2-17 20:25	0.18	10	6.36	136.93	14.33
4	23-2-17 13:02	0.69	15	11.83	210.76	17.24
4	23-2-17 17:11	0.17	25	19.40	368.85	27.93
4	24-2-17 9:15	0.67	30	26.96	529.44	39.85
4	24-2-17 13:54	0.19	35	31.50	708.57	53.68
4	24-2-17 17:44	0.16	45	37.80	740.42	54.06
4	27-2-17 12:19	2.77	60	51.37	1012.72	79.83
4	27-2-17 16:24	0.17	80	64.86	1571.85	126.33
4	27-2-17 20:34	0.17	100	83.18	1933.98	143.01
4	6-3-17 12:35	6.67	140	137.66	-	-
4	6-3-17 16:31	0.16	-	54.70	-	-
4	6-3-17 21:07	0.19	-	3.33	-	-
4	7-3-17 21:03	1.00	-	2.78	-	-
4	8-3-17 17:43	0.86	-	0.07	-	-